TOPICAL REVIEW

An insight into optical metrology in manufacturing

View the article online for updates and enhancements.

Topical Review

An insight into optical metrology in manufacturing

Yuki Shimizu[1]**, Liang-Chia Chen**[2] 🅳**, Dae Wook Kim**[3,4] 🅳**, Xiuguo Chen**[5] 🅳**, Xinghui Li**[6] **and Hiraku Matsukuma**[1] 🅳

[1] Department of Finemechanics, Tohoku University, Sendai 980-8579, Japan
[2] Department of Mechanical Engineering, National Taiwan University, Taipei, Taiwan
[3] James C. Wyant College of Optical Sciences, University of Arizona, Tucson, AZ 85721, United States of America
[4] Department of Astronomy & Steward Observatory, University of Arizona, Tucson, AZ 85721, United States of America
[5] School of Mechanical Science and Engineering, Huazhong University of Science and Technology, Wuhan, Hubei, People's Republic of China
[6] Tsinghua Shenzhen International Graduate School, Tsinghua University, Shenzhen 518055, People's Republic of China

E-mail: yuki.shimizu@nano.mech.tohoku.ac.jp

CrossMark

Abstract

Optical metrology is one of the key technologies in today's manufacturing industry. In this article, we provide an insight into optical measurement technologies for precision positioning and quality assessment in today's manufacturing industry. First, some optical measurement technologies for precision positioning are explained, mainly focusing on those with a multi-axis positioning system composed of linear slides, often employed in machine tools or measuring instruments. Some optical measurement technologies for the quality assessment of products are then reviewed, focusing on technologies for form measurement of products with a large metric structure, from a telescope mirror to a nanometric structure such as a semiconductor electrode. Furthermore, we also review the state-of-the-art optical technique that has attracted attention in recent years, optical coherence tomography for the non-destructive inspection of the internal structures of a fabricated component, as well as super-resolution techniques for improving the lateral resolution of optical imaging beyond the diffraction limit of light. This review article provides insights into current and future technologies for optical measurement in the manufacturing industry, which are expected to become even more important to meet the industry's continuing requirements for high-precision and high-efficiency machining.

Keywords: optical metrology, diffractometry, interferometry, deflectometry, scatterometry, super-resolution, optical coherence tomography

(Some figures may appear in colour only in the online journal)

1. Introduction

Optical metrology plays an important role [1, 2] in today's manufacturing industry, and many optical measurement technologies are employed in state-of-the-art manufacturing processes, due to their ability to provide contactless and high-speed measurements with high resolution [3]. Although optical metrology is a huge topic which involves different

measurement ranges, different surface characteristics, and different fields of application, the major optical measurement technologies in the manufacturing industry can be classified into two groups according to their main uses: those used for precision positioning, and those used for the quality assessment of products.

Optical measurement technologies for precision positioning are key technologies in state-of-the-art manufacturing processes; for example, the fabrication process for semiconductor products and/or optical components is supported by precision sensor technology with a sub-nanometric resolution [1]. Figure 1 summarizes the major optical measurement technologies for precision positioning. They can be divided into those used for the measurement of linear motion or displacement, and those used for the measurement of angular motion or displacement. They can be further classified according to their measurement principles, such as the speed of light, light wavelength, etc. Among these technologies, laser interferometers and optical linear encoders are two of the major sensor types employed for precision positioning [4, 5]. By enhancing the characteristics of light, such as rectilinear propagation and coherence, a sub-nanometric resolution over a measurement range of more than several hundred mm can be realized by these optical sensors. Meanwhile, in recent years, attention has been given to reducing uncertainty in the positioning of an object in three-dimensional (3D) space [1, 6]. For this purpose, planar/surface encoders capable of measuring multi-axis displacement using a planar scale grating are attracting attention [7, 8]. Another possible strategy for reducing positioning uncertainty is to reduce Abbe error by feedback compensation for the angular error motion of a positioning system using an optical-angle sensor, such as an autocollimator. For this reason, some improvements have been made to conventional autocollimators, including the employment of optical-frequency comb lasers [9–11].

Optical measurement technologies for the quality assessment of products are also key technologies in state-of-the-art manufacturing processes. Figure 2 summarizes the major optical measurement technologies used for quality assessment [12–14]. They can be divided into those used for the measurement of the surface form or texture of an object, and those used for the inspection of the internal structure of an object. In terms of the quality control (QC) of products, the importance of measuring the surface form or texture is well recognized in today's manufacturing industry [2, 15, 16]. The major technologies for the measurement of surface form or texture employed in the manufacturing industry are those based on far-field observation for the evaluation of the actual surface form or texture of an object. There are four major measuring technologies: triangulation, classical interferometry, scanning white light interferometry (often referred to as coherence scanning interferometry (CSI)), and deflectometry. These technologies each have their advantages and limitations in terms of their measurement ranges, resolutions, and system sizes, and are employed accordingly, based on the purpose (in-line or off-line) of the manufacturing process. In recent years, demand is increasing for rapid evaluation of large free-form surfaces, which can be achieved with superior performance by optical

systems [15, 17, 18]. Optical methods such as classical interferometry and deflectometry are the main solutions for this requirement, due to their contactless, non-destructive and high measurement-throughput characteristics. To date, much effort has therefore been made to improve measurement accuracy while expanding the measurement range [19–22].

Another increasing demand for optical measurement technologies in today's manufacturing industry is in the evaluation of micro- or nanometric structures. Conventionally, such small features have been evaluated using scanning electron microscopy (SEM) or atomic force microscopy (AFM) [23–25]. However, due to their disadvantage of low measurement throughputs, it is preferable to adopt a post-process approach for optical measurement technologies capable of contactless and non-destructive high-speed measurement in the manufacturing industry, where measurement throughput is important for QC [3]. To date, much effort has been made to improve the lateral and vertical resolutions of microscopy, as well as to realize *in-situ* automatic optical inspection (AOI). In addition, some state-of-the-art technologies referred to as super-resolution (SR) techniques have been proposed to overcome the diffraction limit of optical imaging [26]. Another method for overcoming the diffraction limit in optical metrology is to employ optical scatterometry [7, 27] that measures the statistical parameters of a surface under inspection. This method is not a straightforward one and typically requires the solution of a complicated inverse problem, and also, the applicable targets are limited to periodic nanostructures. Nevertheless, optical scatterometry is finding application in critical dimension (CD) and overlay measurement in the semiconductor industry, due to its characteristics of being high throughput, non-destructive, and easy to use in setup.

Furthermore, in recent years, with the advent of new processing technologies such as additive manufacturing [8], the manufacturing industry demand to realize the inspection of not only the surface form but also the internal structures of a fabricated product has increased.

In responding to the background described above, this article provides an insight into optical metrology for precision positioning and quality assessment in today's manufacturing industry. In section 2, some optical technologies for precision positioning are treated, while mainly focusing on those of a multi-axis positioning system composed of linear slides, often employed in machine tools or measuring instruments in the precision manufacturing industry. We review high-precision optical displacement sensors and angle sensor technologies used for high-precision positioning, which are indispensable for current high-precision machining, as well as application examples of multi-axis measurement. Recent technological development trends are also introduced, such as multi-axis optical-sensor technology with a grating reflector and absolute position-sensing technology that uses an optical-frequency comb-laser source. Furthermore, laser triangulation sensors are also treated in this section, due to their importance [28] in machine shops and factories, where instrumentation cost and ease of use in setup are critical issues. The subsequent sections treat optical measurement technologies used for quality assessment in today's manufacturing industry,
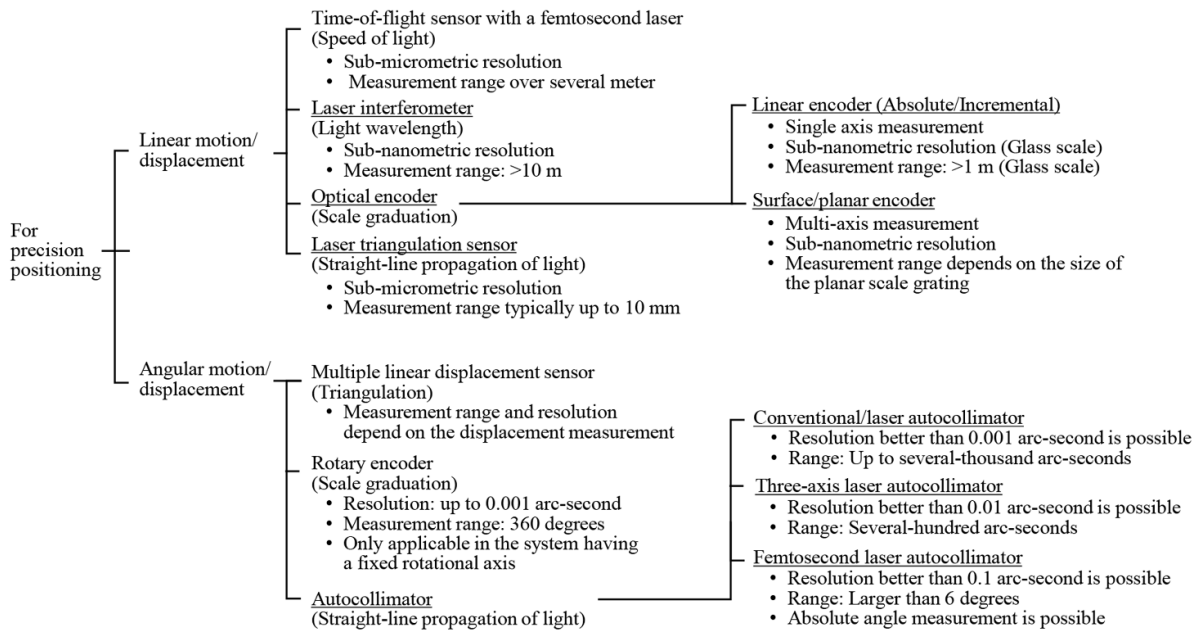
Figure 1. Major optical sensors used for precision positioning (the sensors underlined are treated in section 2).
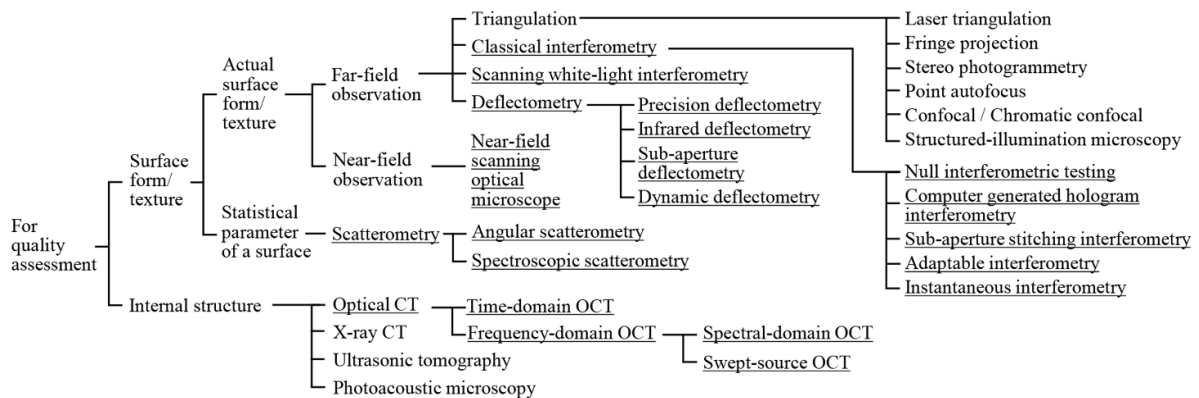

Figure 2. Major optical measurement technologies for quality assessment (the items underlined are treated in sections 3, 4 and 5).

mainly focusing on technologies used for the form measurement of products, from those with a large metric structure such as telescope mirrors, to those with a nanometric structure such as semiconductor electrodes. In section 3, we treat classical interferometry and deflectometry for the measurement of large free-form surfaces, which have been especially in demand in recent years, while introducing the latest technologies for measuring the surface form of astronomical telescope primary mirrors. In section 4, we introduce the basic principles and recent development trends of scanning white-light interferometry (SWLI) and scatterometry for the evaluation of micro-or nanostructures such as MEMS (microelectromechanical system) products, nanometric semiconductor electrodes, etc. Furthermore, in section 5, we address the increasing demands for even higher resolution and the non-destructive inspection of internal structures by providing overviews of optical coherence tomography and SR techniques, which are emerging measurement technologies in today's manufacturing industry.

2. Optical sensor technologies

In the manufacturing industry, lengths and angles are important physical quantities that determine the form of a fabricated component. Sensor technologies for measuring lengths and angles are thus important to guarantee the quality of fabricated products. Besides, optical sensor technologies are one of the key technologies for precision positioning in state-of-the-art manufacturing processes [1]. Among the optical sensor technologies developed so far, optical sensors such as laser interferometers, optical linear encoders and laser triangulation sensors are the main ones often employed in today's manufacturing industry due to their high resolution, high measurement throughput, and easy-to-use setup. Table 1 summarizes the major optical sensors for length and displacement measurements in the manufacturing industry. In particular, laser interferometers and optical linear encoders are two major sensors employed for precision positioning, due to their high resolution, extending as far as the sub-nanometre scale [1, 5].

Meanwhile, in recent years, attention has been given to reducing the uncertainty of object positioning in a 3D space. The application of an optical angle sensor, as well as the design of a positioning system complying with the Abbe principle, could be a solution to further reduce the uncertainty of precision positioning [6, 29]. Furthermore, some innovations in conventional laser interferometers and linear encoders have been implemented. With the use of a reflective two-dimensional (2D) grating in an optical encoder, multi-axis measurement has been realized using a single measurement laser beam [30, 31]. Also, some techniques employing an optical frequency comb laser, which are directly traceable to the time or frequency national standards, are also attracting attention in today's manufacturing industry due to strong demand for measurement traceability [11].

In this section, some optical sensor technologies for the measurement of lengths, displacements, and angles in the manufacturing industry are reviewed. The basic principles of the laser interferometer, optical linear encoder, and laser triangulation sensor are briefly described, and examples of their applications in the manufacturing industry are explained. In addition, optical sensor technologies for multi-axis precision positioning are reviewed, while focusing on a surface/planar encoder technology with a 2D scale grating. State-of-the-art optical angle sensor technologies, including the three-axis laser autocollimator and the mode-locked femtosecond laser autocollimator, which is referred to as the angle scale comb, are also reviewed. Furthermore, an example of the application of optical sensor technology for the measurement of other quantities in SI base units, a Kibble balance for the measurement of mass [32], is also presented.

2.1. Optical sensors for length and displacement measurements

2.1.1. Laser interferometers.
The optical sensors for length and displacement measurements commonly employed in manufacturing are summarized in table 1. Recently, some optical sensors with a sub-nanometric resolution have become available for single-axis measurement of length or a translational displacement and these are employed in the state-of-the-art manufacturing industries [1]. Among them, the laser interferometer [19, 33] and the linear encoder [34, 35] are the main optical sensors employed in the precision positioning of an object.

A laser interferometer [5, 36], which is one of the optical sensors that can directly be linked to a national standard of length [37–40], measures the displacement of an object using the light wavelength of a laser beam, λ, from a laser source as the scale graduation for measurement. Figure 3(a) shows the optical setup of an interferometer based on the homodyne method [41–43] with a single-mode continuous wave (CW) laser, where the intensity, I, of the light captured by a photodetector can be expressed by the following equation (1):

$$I = I_0 \left(1 + \cos \frac{4\pi \Delta x}{\lambda} \right) = I_0 \left(1 + \cos \frac{4\pi n_{\mathrm{air}} f \Delta x}{c_0} \right) \quad (1)$$
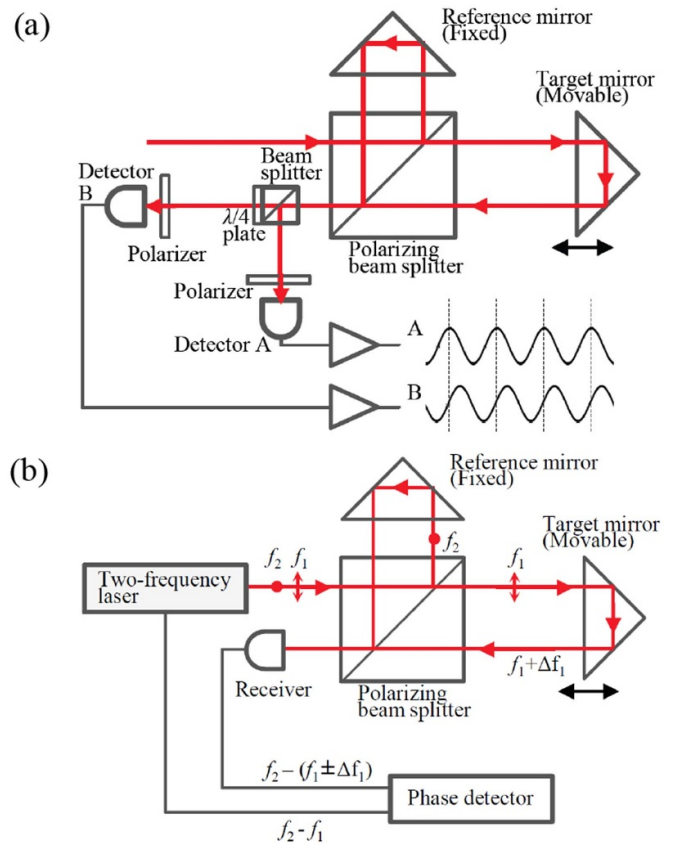

Figure 3. Laser interferometers: (a) homodyne quadratic phase detection, (b) heterodyne phase detection [1].

where n_{air} is the refractive index of air, c_0 is the speed of light in a vacuum, f is the optical frequency, and Δx is the displacement of a moving target. Since the light intensity, I, is modulated with a period of half of λ with respect to Δx, as shown in equation (1), Δx can be detected by counting the occurrences of constructive and destructive interference using the photodetector. It should be noted that the direction of motion of a moving target cannot be detected using a single output signal from a photodetector. Most of the commercial interferometers therefore use at least two interference signals with a phase difference of $\pi/2$ rad to judge the direction of motion. Since the intensity modulation of the superimposed reflected beams is utilized for measurement, the homodyne method is poorly isolated from external disturbances. On the other hand, the heterodyne method [19, 39, 41], in which the beat frequency of the superimposed reflected beam is utilized for measurement, is more stable than the homodyne method. Figure 3(b) shows a schematic of the heterodyne method, where two monochromatic laser beams with slightly different optical frequencies f_1 and f_2 are utilized. By controlling the polarization modulation, one of the laser beams, with a frequency of f_2, is made incident to the reference mirror (held stationary in this setup), while the other, with a frequency of f_1, is projected onto the moving target. Due to a Doppler shift, the laser beam reflected by the measurement mirror experiences a frequency shift Δf_1 that can be expressed by the following equation using the velocity v of the moving target [19, 39, 41]:

Table 1. Major optical sensors for lengthand displacement measurements.

Laser interferometer	• A light wavelength is employed as the graduation for measurement • Homodyne and heterodynetypes are available • Nanometric resolution over several meters • Absolute length measurement is possible with a laser beam having multiple wavelengths or a continuouslyvarying wavelength • Poor isolation from external disturbance due to a large optical path difference; environmental control is required for precision measurement
Linear encoder	• Micropattern structures on a scale are employed as graduations for measurement • Absolute and incrementaltypes are available • A sub-nanometric resolution over a range of 1 m • Nanometric resolution
Confocal probe	• Confocality of an optical system is employed to detect the distance between an objective lens and a target • Several tens of nanometers' resolution over several tens of micrometers with a mode-locked femtosecond laser source • Sub-nanometric resolution
Time-of-flight distance sensor	• Speed of light is utilized to detect the distance between an optical head and a target • Sub-micrometer resolution over several hundred m for a femtosecond laser system
Laser triangulation sensor	• Detects the axial position of a target as the displacement of a reflected beam on a photo-detector • Compact optical head, easy to use in machine shops and factories • A sub-micrometric resolution over several tens of mm
Optic fiber sensor	• Detects fiber deformation by observing the spectrum of transmitted light • Can be employed to measure temperature and force by observing fiber deformation • Nanometric resolution over several micrometers

$$\Delta f_1 = 2vn_{air}f_1 \ 2vn_{air}f_1c_0 - c_0. \tag{2}$$

Since the difference of the optical frequencies (f_1–f_2) of the two laser beams from the light source is known, being a design parameter, the velocity v of the measurement mirror can be obtained by detecting the optical frequency of the beat signal ($f_1 + \Delta f_1$–f_2). By integrating v with respect to time, the displacement of the moving target can be detected. A sub-nanometric resolution has been achieved by these laser interferometers due to their enhancement with a signal interpolation technique. Also, due to the long working distance of the laser interferometer, multi-axis measurement can easily be achieved by splitting the laser beam into sub-beams and preparing the corresponding multiple receivers. Nowadays, laser interferometers are widely employed in many applications where ultra-precise positioning with feedback from precision displacement sensors is mandatory [19, 44]. Furthermore, some notable techniques have been developed to carry out absolute distance measurement by employing multiple wavelengths simultaneously in parallel or in sequence, or by continuously varying the wavelength [45–47]. Meanwhile, due to the large optical path difference (OPD) between the reference arm and the measurement arm, a laser interferometer can easily be affected by the fluctuations of the refractive index of air, n_{air}, induced by external disturbances such as temperature, humidity, and ambient pressure [48, 49]. Strict

environmental control is therefore required for accurate displacement measurement.

2.1.2. Optical linear encoders. An optical linear encoder [34, 35, 50], which is another of the main optical sensors for precision positioning, measures the displacement of a scale with respect to an optical reading head. Optical linear encoders can be classified into the absolute type [35, 50, 51] and the incremental type [34, 52]. In the absolute type of optical encoder, a scale with a serial code structure such as an M-code [53, 54], which is unique over the measuring length of the scale, provides absolute positional information. The absolute type has increased its market share in recent years due to its cost, robustness, and high throughput when enhanced by a high-speed image sensor [1]. Meanwhile, most of the absolute scales have an incremental track, which can be employed in the same manner as the incremental type, to achieve high-resolution position measurement. Figure 4 shows a schematic of the interferential scanning type of linear encoder, which is an example of the incremental type. With the use of a scale that has an incremental track composed of equally-spaced line-pattern structures, an interferential scanning-type linear encoder can achieve a sub-nanometric resolution. A light ray from a light source is made incident to the scale at a right angle to generate diffracted beams, and the first-order diffracted
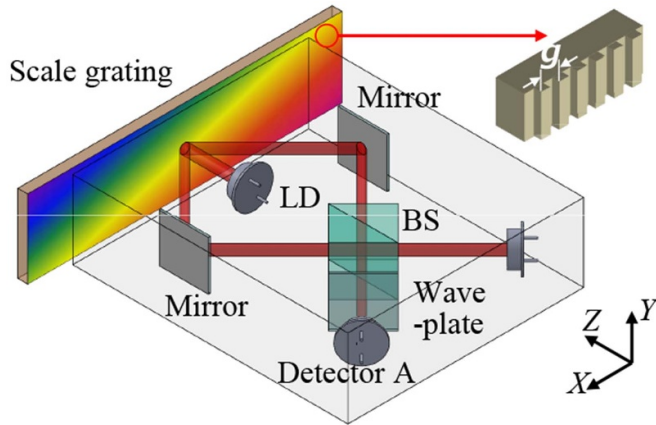
Figure 4. Interferential scanning-type linear encoder.

Figure 5. A multi-axis positioning system employing multiple interferometers. Reproduced from [6]. © IOP Publishing Ltd. All rights reserved.

beams are then superimposed to generate an interference signal. Denoting the period of the line-pattern structures on a scale grating as g, the light intensity I_{LE} detected by the photodetector in the optical head can be expressed by the following equation [34, 41]:

$$I_{LE} = I_0 \left(1 + \cos \frac{4\pi \Delta x}{g} \right) \quad (3)$$

where Δx is the x-directional scale displacement with respect to the optical head. As can be seen from the equation, constructive and destructive interference repeats with a displacement Δx of $g/2$. As can be seen in figure 4, the superimposed first-order diffracted beams are split into two sub-beams, and one of the sub-beams is made to pass through a polarizer to apply a phase retardance of $\pi/2$ rad. By using the two interference signals obtained, which have a phase difference of $\pi/2$ rad, the displacement Δx can be detected at a high resolution while distinguishing the direction of motion through signal interpolation.

By employing several one-axis precision optical-displacement sensors such as linear encoders and/or laser interferometers, multi-axis positional measurement can be carried out for precision positioning [6, 29, 55, 56]. Figure 5 shows an example of a multi-axis positioning system where multiple laser interferometers are employed [6]. In this system, a probe for the profile measurement of a sample is held stationary in 3D space, while the X-, Y- and Z-directional motions are given to the sample by a multi-axis positioning system whose motion is measured by three laser interferometers. The three laser interferometers are arranged in the setup in such a way that the beam axes intersect at the tip of the probe; namely, the system is designed to satisfy the Abbe principle [57]. Such a multi-axis positioning system can also be constructed by arranging several linear encoders in such a way that that measurement axes of the linear scales intersect at the position where the tip of a probe for profile measurement is placed to satisfy the Abbe principle [29]. However, it is not so easy to apply these sensor arrangements in a small system where the space available for the sensors is limited. Besides,
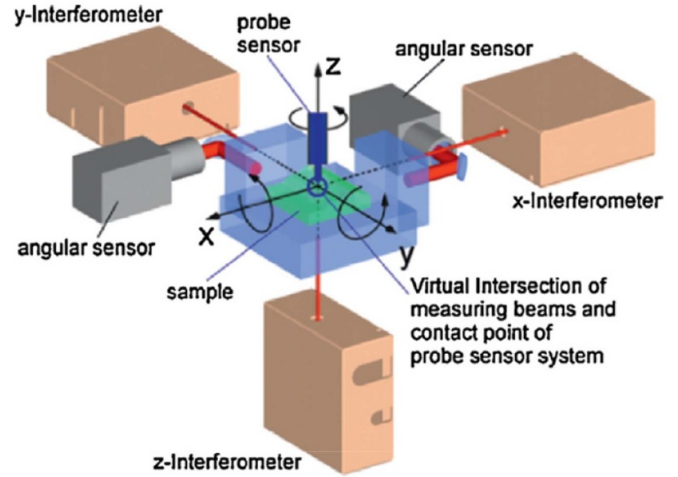
in most applications, it is not easy to design a multi-axis positioning system complying with the Abbe principle, mainly due to the restrictions that come from the mechanical design of such a system.

2.1.3. Multi-axis optical encoders. To overcome the aforementioned problems in a multi-axis positioning system, optical sensors known as planar/surface encoders have been developed that are capable of measuring multi-axis displacements using a single measurement laser beam [30, 58–63]. Figure 6 shows a schematic of the measurement principle of an optical surface encoder capable of measuring primary in-plane (XY) displacements and the secondary out-of-plane (Z) displacement of a scale XY grating using a single measurement laser beam. The scale XY grating and a reference XY grating are employed instead of the measurement mirror and the reference mirror, respectively, of a conventional Michelson interferometer. The reference XY grating is held stationary in space, while the scale XY grating can travel in the X-, Y- and Z-directions. The laser beam from a laser diode (LD) unit is split into two sub-beams (the measurement and reference beams) using a beam splitter. The measurement beam and the reference beam are made incident to the measurement mirror and the reference mirror, respectively, to obtain the X- and Y-directional diffracted beams. The positive and negative first-order diffracted beams from the XY gratings are superimposed at the beam splitter to generate interference signals (I_{X+1}, I_{X-1}, I_{Y+1}, I_{Y-1}) that can be captured by photodetectors. The primary motions of the scale XY grating in the $X-$ and Y-directions (Δx, Δy) can be detected in the same manner as that used by conventional interferential scanning-type linear encoders through signal interpolation of interference signals having a phase difference of $\pi/2$. Also, the secondary motion of the scale grating in the Z-direction (Δz) can be obtained by detecting the phases of the first-order diffracted beams in the same manner as that used by the conventional homodyne method. Experimental results have demonstrated
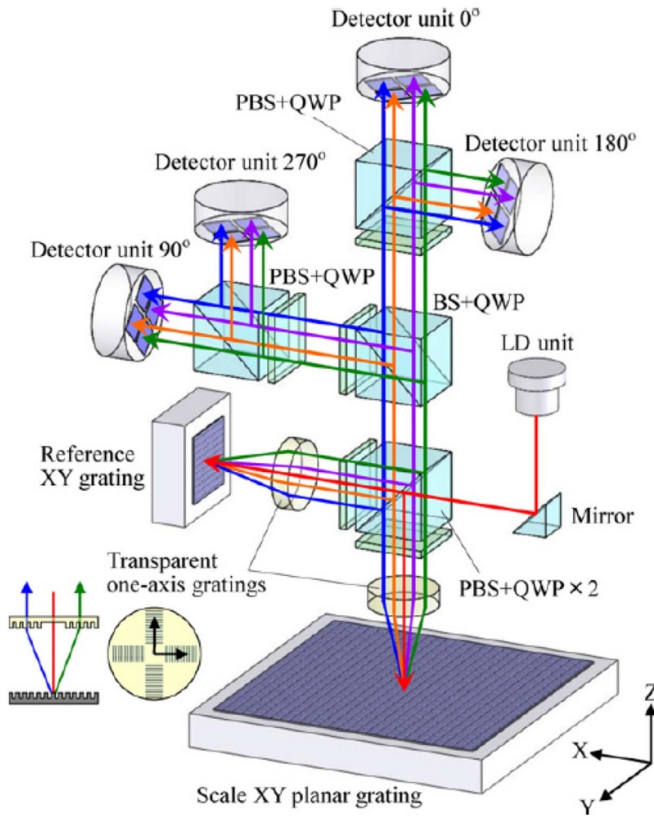
Figure 6. A surface encoder for the measurement of three-axis (*XYZ*) translational displacement. Reprinted from [58], copyright (2012), with permission from Elsevier.

Figure 7. Surface encoder with a mosaic scale grating. Reproduced from [64]. © IOP Publishing Ltd. All rights reserved.

that simultaneous three-axis displacement measurement with a sub-nanometric resolution can be carried out using *XY* gratings with a pitch of 1 μm [58].

The measurement range of a planar/surface encoder along the primary axes (*XY*) is determined by the in-plane size of the scale *XY* grating. With the increase of wafer diameters in the semiconductor industry, a measurement range of more than 500 mm × 500 mm in the primary axes is required for a positioning system. For this purpose, a scale *XY* grating larger than 500 mm × 500 mm is required; however, the fabrication of such a large-scale *XY* grating costs too much. Furthermore, the deformation of a large-scale grating due to gravity could result in a degradation of measurement accuracy. To address these issues, the concept of the mosaic grating is introduced for a planar/surface encoders [64]. Figure 7 shows a planar encoder with a mosaic scale grating composed of several small-scale *XY* gratings aligned in a matrix. As can be seen in the figure, a group of optical heads arranged in a matrix for three-axis displacement measurement is employed to read the in-plane displacement of the mosaic scale grating. Using a stitching technique on the readings from the group of optical heads, the arrangements of the optical heads and the small-scale gratings enable the planar/surface encoder to treat the small-scale *XY* gratings as a large-scale *XY* grating. A small-scale grating can easily be fabricated, based on the perspectives of technology and cost [65–70]. Furthermore, the mosaic scale grating
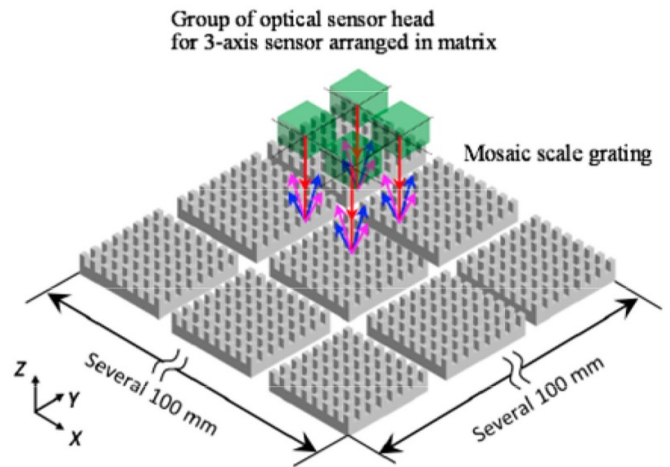
can avoid the issues that arise from scale deformation due to gravity.

The concept of a planar/surface encoder with multiple measurement beams can also be extended to the measurement of the rotary motion of an object. Figure 8 shows the optical layout of the *Z*-θ_Z sensor [71]. In this setup, 2D sinusoidal micropattern structures fabricated on a cylindrical moving element by a fast tool servo technique [60] are read by multiple laser measurement beams. Using a quadrant photodiode (QPD) with four active cells aligned in a matrix, *Z*-directional translational motion and rotational motion about the *Z*-axis can be detected simultaneously. It should be noted that the influence of the form errors of the sinusoidal micropattern structures can be reduced by the averaging effect of multiple measurement beams.

2.1.4. Laser triangulation sensors. Laser triangulation sensors are often employed in industrial fields where fast and contactless measurements with a resolution of less than a micrometre are required. Figure 9 shows two types of optical head for a laser triangulation sensor. The angle of incidence of the measuring laser beam should be selected based on the surface reflectivity of the object under measurement. In the case of measuring a mirror surface, an oblique incident angle is selected, as shown in figure 9(a). According to the geometric relationship of the setup, the target displacement, Δd, can be expressed by the following equation:

$$\Delta d = \frac{p}{s}\Delta h\prime \cos\beta \tag{4}$$

where β is the angle of incidence of the measurement laser beam for the target surface, p is the distance between the target surface and the lens, s is the distance between the lens and the detector plane, and $\Delta h'$ is the spot displacement on a position-sensing detector. With the use of image sensors such as charge-coupled devices (CCDs) or complementary metal-oxide-semiconductors (CMOS) as the position-sensing detectors, the measurement range of a commercial laser
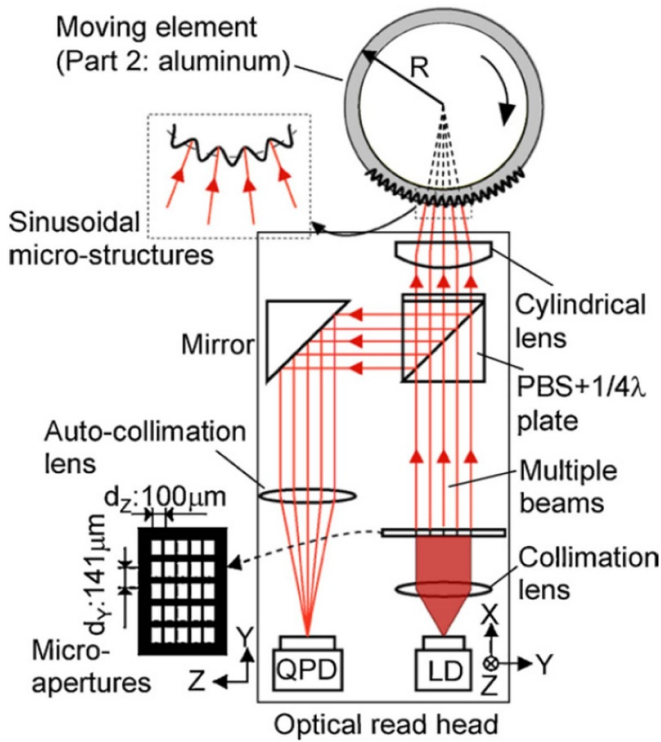
Figure 8. *Z-θ* encoder. Reproduced from [71], copyright (2010), with permission from Elsevier.

Figure 9. Laser triangulation sensors with (a) oblique incidence and (b) right-angle incidence.

Figure 10. Cutting error measurement of flexspline gears of harmonic speed reducers by laser triangulation sensors. Reprinted from [73], copyright (2004), with permission from Elsevier.

triangulation sensor can be up to 10 mm [72]. Meanwhile, in the case of measuring a rough surface, the measurement laser beam is set to be incident to the measuring surface at a right angle, as shown in figure 9(b). In this case, the displacement Δd can be expressed as follows, using the initial spot position h' and the spot displacement $\Delta h'$ on the detector plane:

$$\Delta d = w \cdot s \left(\frac{1}{h\prime} - \frac{1}{h\prime + \Delta h\prime} \right) \qquad (5)$$

where w is the distance between the laser beam and the lens axis, while s is the distance between the lens and the detector plane. It should be noted that h' is determined by w, the initial target position d and the focal length of the lens; these are designed parameters in the optical setup. Therefore, by detecting $\Delta h'$, the displacement of the target surface, Δd, can be measured. With the use of scanner systems, laser triangulation can also achieve fast 3D profile measurement. Meanwhile, factors such as the working distance, the angle of incidence of the measuring laser beam with respect to the target surface, the local slope of the target surface, and the influence of ambient light can all affect the accuracy of laser triangulation sensors. In particular, the speckle noise due to the roughness or texture of a target surface can strongly affect measurement accuracy, since the displacement of a target surface is detected by observing the displacement of a focused laser beam at the detector. This problem can be avoided by employing a light source with a small temporal and/or spatial coherence. The employment of a large observation aperture can also reduce
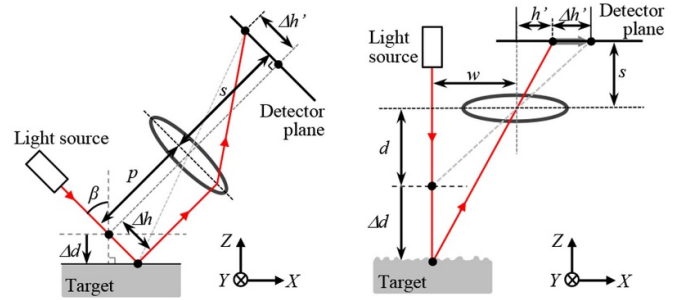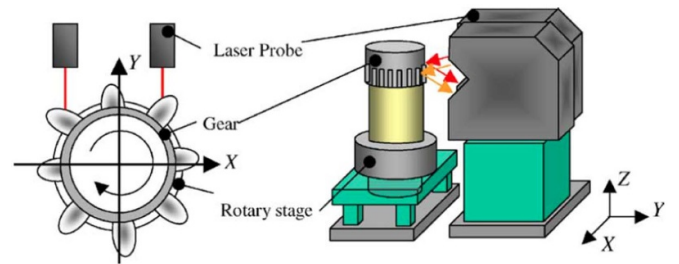
the influence of speckle noise. The resolution of most of the commercially available laser-triangulation sensors, which is mainly limited by the resolution of the detector, is on the order of 0.1 μm.

Figure 10 shows an example of a laser-triangulation sensor deployed in an industrial application [73]. The two laser beams from a pair of laser-triangulation sensors are projected onto different tooth surfaces of a flexspline gear of harmonic speed reducers with a certain spacing for evaluation of the tooth thickness. One of the advantages of the laser triangulation sensor is its long working distance; this feature enables the laser triangulation sensor to be employed in many industrial applications [74–77].

2.1.5. Absolute distance measurement by a mode-locked femtosecond laser. In the last two decades, several methods have been developed for absolute length measurement using the optical frequency comb of an ultra-short pulse laser [78–81]. With the development of fiber-based femtosecond laser sources [10, 82] capable of being fabricated even in laboratories where facilities and budgets are limited, the application of optical-frequency comb sources to dimensional metrology is being accelerated. Figure 11 shows an example of a method based on time-of-flight (TOF) measurement employing a mode-locked femtosecond laser source [81]. A mode-locked femtosecond laser beam from the laser source is first collimated and is then divided into two sub-beams. One sub-beam is employed as the reference beam, while the other is employed as the measurement beam. The reference beam is made incident to a reference reflector held
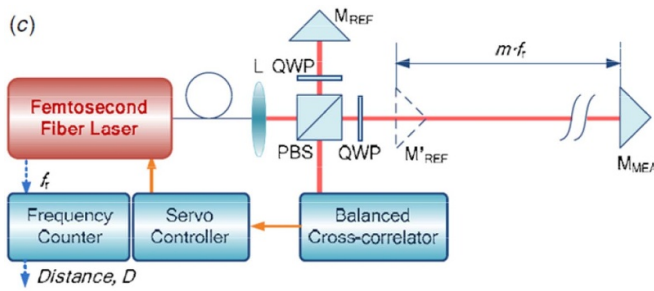
Figure 11. Absolute distance measurement based on the time-of-flight (TOF) method with a mode-locked femtosecond laser source. Reprinted from [81]. © IOP Publishing Ltd. All rights reserved.

Figure 12. Femtosecond laser chromatic confocal probe. Reproduced from [83]. © IOP Publishing Ltd. All rights reserved.

stationary in space, while the measurement beam is projected onto a target reflector capable of traveling along the measurement beam's axis. To obtain a reflected measurement beam with a sufficient light intensity, a retroreflector is employed as the target reflector. Pulse trains in the reflected measurement beam and those in the reflected reference beam are detected by a balanced cross-correlator using second-harmonic generation (SHG) by a nonlinear optical crystal to obtain the absolute distance to the target reflector [81]. In the proposed method, absolute distance measurement with a sub-micrometre precision has been achieved at a working distance of 700 m.

Figure 12 shows another example of the measurement of the absolute position of a target using a mode-locked femtosecond laser source in a chromatic confocal probe [83–86]. A mode-locked femtosecond laser beam from a fiber-based laser source has a non-uniform spectrum; this characteristic of the laser source strongly affects the axial response curve in a confocal probe for absolute position measurement. To address this issue, a dual-detector configuration is employed in the optical setup, as shown in figure 12. By obtaining two axial response curves with two fiber detectors in different confocal setups, the influence of the non-uniform spectrum of the mode-locked femtosecond laser beam, as well as the influence of the surface reflectivity of the measurement target, can be eliminated through a differential operation. With the enhancement of peak-detecting algorithms, absolute positional measurement with a resolution of 20 nm has been achieved [83]. Table 2 summarizes the advantages and disadvantages of the optical length and displacement sensors treated in this section.

2.2. Optical angle sensor

The main optical-angle sensors are summarized in table 3. A rotary encoder is one of the major optical-angle sensors employed in manufacturing processes [1, 50]. In a rotary encoder, circumferential patterns on a disk scale's surface are employed as the graduations for angle measurement and are read by an optical head. Optical rotary encoders are also classified into 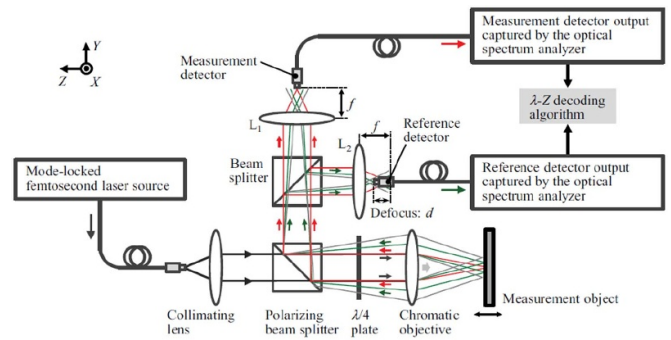the absolute type and the incremental type, in the same manner as a linear encoder. An interferential scanning-type rotary encoder, for which the principle of reading the grating patterns is almost the same as that of the linear encoder, can carry out angular measurement with a high resolution over 360°. In the national measuring institute of Japan, an encoder system with multiple optical heads has achieved a resolution of 0.0015 arc-second while assuring angle measurement accuracy of ±0.03 arc-second over a range of 360° [87]. An optical rotary encoder can be employed in applications where the rotational axis of a measuring object is fixed in space. Therefore, it is difficult to employ a rotary encoder in applications where the working distance between an optical head and a disk scale could be changed; for example, in the case of evaluating the angular error motion of a table in a precision linear slide. In such a case, angular measurement can be carried out using laser interferometers with multiple laser measuring beams if an appropriate laser source and a sufficient number of photoreceivers are available [88, 89].

2.2.1. Autocollimator. An alternative method for the cases where a rotary encoder cannot be applied is to employ an optical autocollimator [90–92]. In an autocollimator, by using a collimator objective (CO) with a long focal length, a high resolution of better than 0.01 arc-second can be achieved. By employing a CCD or a CMOS image sensor, a wide measurement range of over ±1° can also be achieved [91]. However, since the sensor's sensitivity is in proportion to the focal length of the CO [93], the size of the sensor tends to become larger as the sensor sensitivity increases. On the other hand, a laser autocollimator, which is based on laser autocollimation [94] and employs a monochromatic laser source, can be designed to have a compact size while achieving a high resolution. Figure 13 shows a schematic of the optical setup of a two-axis laser autocollimator having a photodiode with four active cells (a QPD) as the photodetector [95]. The use of the photodiode makes the sensor sensitivity independent of the focal length of the CO [94, 95]. As a result, a compact optical angle sensor having a high resolution of more than 0.001 arc-second can be achieved [96]. Furthermore, the use of a multi-cell PD can offer a wide measurement range without sacrificing the resolution [97].

Table 2. Advantages and disadvantages of the optical length and displacement sensors treated in this section.

Laser interferometer	• Sub-nanometric resolution • Long measurement range • Absolute measurement is possible with a multi-wavelength technique • Easy to design a measurement system complying with the Abbe principle • Easily affected by external disturbances
Linear encoder	• Sub-nanometric resolution • Measurement range: up to several meters (in the case of a glass scale) • Absolute measurement is possible • Robust against external disturbance • Scale deformation could affect the measurement • Difficult to comply with the Abbe principle in most applications
Multi-axis optical encoder	• Sub-nanometric resolution • Multi-axis translational and angular motions can be measured by a single laser beam using a planar scale grating • Measurement range is limited by the size of a planar scale grating (this can be overcome by the mosaic grating technique [64]) • Need to establish a method for the calibration of a planar scale grating
Laser triangulation sensor	• Sub-micrometric resolution • Easy-to-use setup in the manufacturing industry • Measurement range: up to several tens of mm • Measurements can be affected by the surface characteristics of a measurement target
Absolute distance measurement by a mode-locked femtosecond laser	[TOF] • Sub-micrometric accuracy over a wide measurement range (working distance: 700 m) • Absolute measurement is possible • High instrumentation cost (Chromatic confocal probe) • Resolution: up to 20 nm • A limited measurement range of up to several tens of μm (need to optimize the design of a chromatic objective lens) • A high instrumentation cost

Table 3. Major optical sensors for angle measurement.

|	
Rotary encoder	• Uses patterns on a disk scale surface as graduations for angular measurement • Absolute and incremental types are available • Measurement accuracy of up to ±0.03 arc-second over a measurement range of 360° • Can only be applied in cases having a fixed axis of rotation.
Autocollimator	• Detects the displacement of a measurement beam reflected from a target surface to measure angular displacement of the target • Can be applied for in cases with no fixed axis of rotation. • A high resolution of better than 0.001 arc-second is possible for the laser autocollimator • A wide measurement range over 6° can be possible with the use of a mode-locked femtosecond laser and a grating reflector
Fiber optic gyroscope	• Detects the angular velocity of the setup based on the Sagnac effect • Drift components in the angle reading are not suitable for use in manufacturing processes • Nanometric resolution
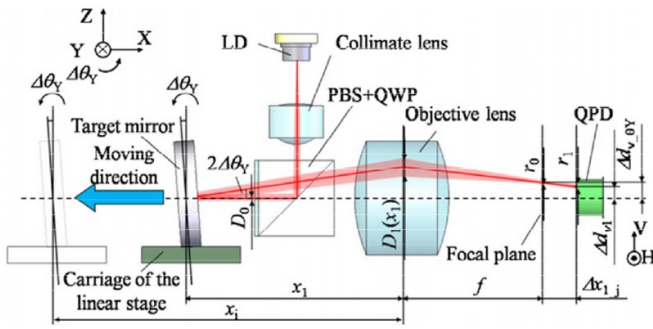
Figure 13. Laser autocollimator for two-axis angle measurement. Reproduced from [95]. © IOP Publishing Ltd. All rights reserved.
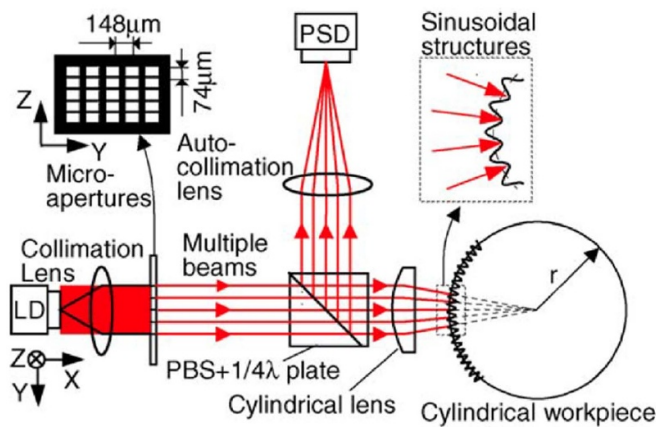

Figure 14. On-machine measurement of sinusoidal micropatterns fabricated on a cylindrical workpiece. Reprinted from [102], copyright (2006), with permission from Elsevier.

Laser autocollimators can also be employed to evaluate the surface form of an object [21, 98–101]. By scanning the measurement laser beam of a laser autocollimator over the surface under inspection, a series of local slope data can be obtained, from which the surface form can be reconstructed. The influences of the scanning motion errors can be canceled by the use of a pentaprism [21, 99] or a multi-probe method [98]. Furthermore, the application of laser autocollimators can also be expanded to the measurement of microstructures. Figure 14 shows an example of the on-machine measurement of microstructures by an optical angle sensor [102]. By employing a cylindrical lens, multiple beams are projected onto the cylindrical workpiece in such a way that the same phase positions in different periods of the sinusoidal microstructures can be evaluated. By using the setup shown in the figure, on-machine measurement of sinusoidal microstructures with an amplitude of 100 nm and a pitch of 100 μm has been achieved.

2.2.2. Three-axis laser autocollimator. Conventional autocollimators and laser autocollimators can carry out two-axis angle measurement using an image sensor, a QPD or multiple single-cell photodiodes as the photodetector. Meanwhile, due to the principle of angular measurement, the angular displacement of a target about the axis of the measurement

beam cannot be detected. For simultaneous measurement of three-axis ($\theta_X \theta_Y \theta_Z$) angular displacements, a pair of orthogonally aligned 2D autocollimators is required. For the case of measuring three-axis angular displacement using a laser interferometer system, six laser measuring beams and the corresponding photoreceivers, as well as complicated optical alignments, are required. To address this issue, a three-axis laser autocollimator has been developed [103]. Figure 15 shows a three-axis laser autocollimator where a grating reflector is employed instead of the flat mirror reflector employed in conventional autocollimators and laser autocollimators. Also, an additional autocollimation unit composed of a CO and a QPD is added to the setup to detect the zeroth-order diffracted beam as well as the first-order diffracted beam. The zeroth-order diffracted beam is employed to detect the angular displacement of the target about the *X*- and *Y*-axes ($\Delta\theta_X$ and $\Delta\theta_Y$) in the figure. The zeroth-order diffracted beam is insensitive to the angular displacement of the target about the Z-axis ($\Delta\theta_Z$). On the other hand, the first-order diffracted beam is sensitive to the three-axis angular displacement of the grating reflector. Therefore, by detecting the zeroth-order and the first-order diffracted beams simultaneously with the corresponding autocollimation units and carrying out a simple calculation, the angular displacement of the grating reflector about the Z-axis can be detected. It should be noted that, due to the different measurement principles, the sensitivity of measurement of $\Delta\theta_Z$ is different to that of $\Delta\theta_X$ and $\Delta\theta_Y$. However, this can be compensated for by adding an optical magnifier composed of a pair of lenses, as shown in figure 15. Using this setup, simultaneous measurement of the three-axis angular displacement of a grating reflector has been achieved, with a resolution better than 0.01 arc-second [103]. Furthermore, with the employment of a reference float supporting a scale grating, the concept of the three-axis laser autocollimator can be extended to a liquid-surface-based three-axis inclination sensor [104].

It should be noted that the three-axis laser autocollimator can easily be combined with the three-axis surface encoder [58] introduced in the previous section to construct a six-degree-of-freedom (six-DOF) surface encoder that can measure three-axis translational displacements (*XYZ*) and three-axis angular displacements ($\theta_X \theta_Y \theta_Z$) with a single measurement laser beam [30]. By arranging the displacement assembly and the angular assembly in such a way that these assemblies share a single measurement laser beam and scale grating, the optical head of the six-DOF surface encoder can be designed to have a compact size [30, 31]. Crosstalk between the displacement assembly and the angular assembly can be suppressed by careful design of the optical setup [105].

2.2.3. Femtosecond laser autocollimator. Applications of the mode-locked femtosecond laser source to optical angle sensors have also been seen in recent years [31], with the development of fiber-based femtosecond laser sources [10, 82]. Figure 16 shows a schematic of the 'angle scale comb' that can be employed as the scale graduation for optical angle measurement [106]. The optical modes of a
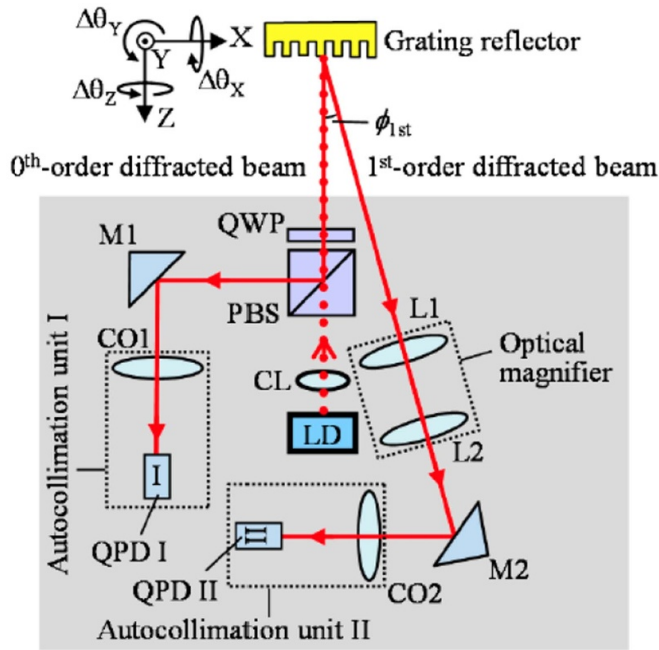
Figure 15. A three-axis laser autocollimator. Reprinted from [103], copyright (2011), with permission from Elsevier.

Figure 16. An angle scale comb generated by an optical frequency comb and a two-axis grating reflector. Reprinted from [106], copyright (2017), with permission from Elsevier.

Figure 17. A femtosecond laser autocollimator with an optical-frequency-domain angle-measurement method. Reproduced from [108]. CC BY 4.0.

mode-locked femtosecond laser equally spaced in the optical frequency domain are converted into a group of first-order diffracted beams (an angle scale comb), each of which has an angle of diffraction corresponding to its optical frequency with the dispersive characteristics of a grating reflector. Multi-axis angular measurement can be achieved by an angle scale comb using a 2D diffraction grating. By combining an angle scale comb with conventional laser autocollimation, high-resolution angle measurement over a wide range can be achieved with an optical head designed to be compact [107]. Furthermore, observation of the optical frequency comb emanating from the grating reflector in the optical frequency domain enables the reading head to resolve the modes overlapping at the fiber detector with high visibility [108, 109]. Figure 17 shows a mode-locked femtosecond laser autocollimator with an optical frequency-domain angle measurement method. A high resolution of better than 0.03 arc-second over a wide angular measurement range of more than six degrees has been achieved so far [106–109]. In addition to the angle scale comb, some methods for angular measurement with a mode-locked femtosecond laser utilizing SHG [110], chromatic aberration of a lens [111] etc., have been developed so far [112]. Table 4 summarizes the advantages and disadvantages of the optical angle sensors treated in this section.

2.3. Optical sensors contributing to the measurement of major physical quantities

In the current SI system of units, some physical quantities are associated with each other, as shown in figure 18 [113]. Optical sensors for the measurement of length and displacement therefore contribute to the measurement of other physical quantities, such as mass and temperature [114].
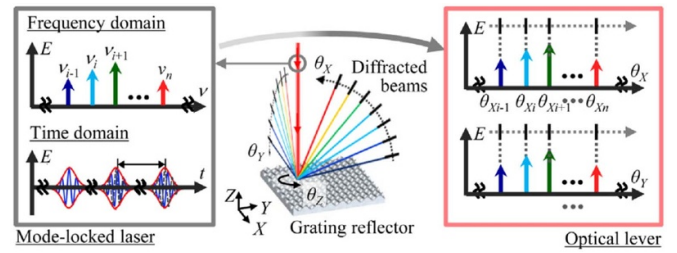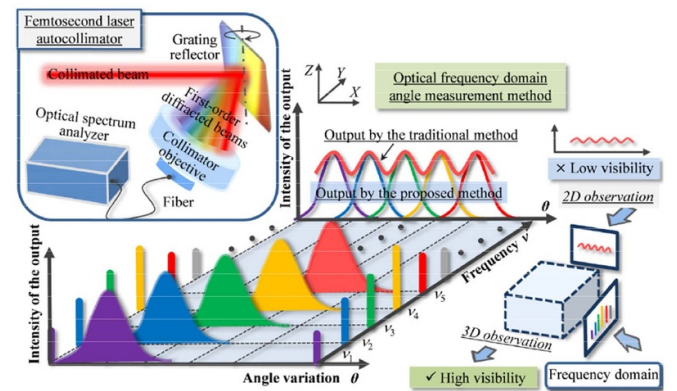
Figure 19 shows an example of optical displacement sensors used in a system for the measurement of mass, which is referred to as the Kibble balance [115, 116]. This system has been developed at a compact size so that gram-level precision mass measurements can be carried out in industrial laboratories without referring to a calibrated artifact. This system can be operated in two different modes, the velocity mode based on Faraday's law and the force mode associated with the Lorentz force. By utilizing these two modes, electrical and mechanical powers are linked with each other. The system is mainly composed of the main mass side (MMS) related to the velocity and force mode, and a counter mass side, and both sides are hung using a titanium fibre through a truncated wheel. By comparing the weight of an object of interest to a calibrated electromagnetic force determined by electrical quantities, an absolute measurement of weight can be carried out. The counter-mass side acts as a driving motor in the velocity mode. In this setup, a heterodyne-type interferometer with a dual-frequency 2.83 MHz Zeeman split-laser source is employed for measurement and control of the Z-directional motion of the air-bearing shaft attached to the coil of the MMS. Attention is paid to the position of the reference mirror in the interferometer to minimize the OPD of the sub-beams in the interferometer and reduce the influence of common-mode noise components. Interference signals are detected by two time-interval analyzers, which are capable of detecting frequency and time

Table 4. Advantages and disadvantages of the optical angle sensors treated in this section.

Autocollimator with an image sensor	• Resolution: up to 0.005 arc-second • Two-axis measurement is possible with an image sensor • A wide measurement range of up to several thousand arc-seconds • Sensitivity depends on the focal length of a collimator objective → Relatively large optical setup for high-sensitivity measurement
Laser autocollimator (based on laser auto-collimation)	• Resolution beyond 0.001 arc-second is possible • Sensitivity is independent of the focal length of a collimator objective→A compact optical setup • A limited measurement range of up to several hundred arc-seconds (this limitation can be overcome by a multi-cell photodiode [97])
Three-axis laser autocollimator	• Resolution: up to 0.01 arc-second • Three-axis angular displacement can be measured simultaneously • A grating reflector is required
Femtosecond laser autocollimator	• Resolution: 0.1 arc-second • A wide measurement range over 10 000 arc-seconds • Robust measurement in the optical frequency domain • Absolute measurement is possible • A grating reflector is required • Measurement throughput is restricted by the spectrometer employed in the optical head • A high instrumentation cost

intervals at high speed; one is employed for the feedback control of the system, while the other is employed so that the velocity can be detected when triggered by a signal from the field programmable gate array (FPGA). It should be noted that a 10 MHz reference clock linked to a GPS timer is provided to the system. Also, another optical system composed of a corner cube, a laser source and a position-sensitive detector (PSD) is employed to measure the motion of the air-bearing shaft in the horizontal direction. Optical form interferometry, which is described in the following section of this paper, is also contributing to the establishment of a mass standard for the SI base units [114, 117].

3. Optical form interferometry and deflectometry

The optimal functionality of various scientific and commercial optical systems is often enabled by unique optical surfaces such as aspheric lenses and free form optics. The measurement of optical surface forms requires a distinct dynamic range, precision, and accuracy. Different approaches and technologies are utilized to measure a specific aspect of the surface form and the associated optical quality. To achieve optical systems with a higher spatial resolution, a wider field of view, and better speed (i.e. smaller f-numbers), the optical surfaces of mirrors and lenses are becoming highly aspheric, off-axis, and free-form, requiring non-traditional metrology solutions.

Traditional optical form/figure specifications include peak-to-valley (PV) and root-mean-square (RMS) surface errors. For the highest-quality optical systems, however, the traditional specification methods do not ensure high-contrast imaging performance, which is affected by the spatial frequency
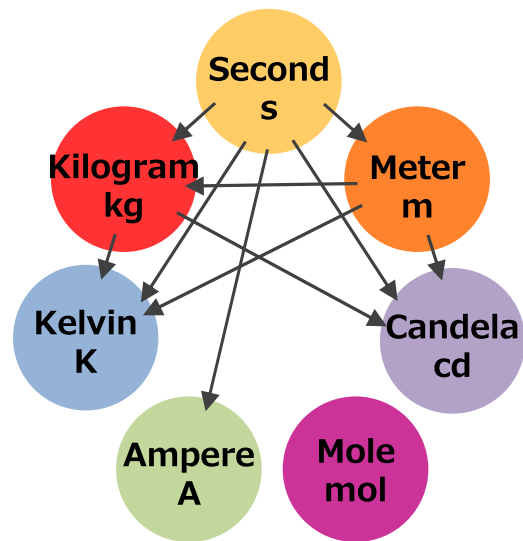

Figure 18. The new SI system of units.

contents of the optical surface form. For instance, the spatial frequencies of the lens surface will directly impact the spatial irradiance distribution of the point spread function (PSF) at the imaging plane. An example of the loss in PSF quality due to mid-spatial frequency errors is shown in figure 20 [118].

Various advanced metrology concepts and methods have been researched and developed to measure and test optical surfaces across the low-, mid- and high-spatial-frequency bands. In particular, interferometry and deflectometry have been the two main solutions for measurement and control of modern optical manufacturing and production.
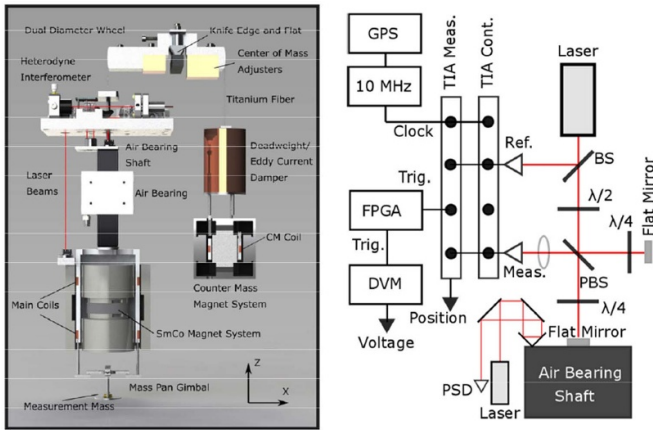
Figure 20. A PSF comparison of two identically specified optical systems shows a highly focused irradiance spot for the well-controlled mid-spatial-frequency case (left) and a scattered focus pattern for the case with mid-spatial frequency errors in the optics (right). The color shows the relative irradiance in each PSF on the detector plane. Image credit: R Parks.

3.1. Optical form interferometry

3.1.1. Null interferometric testing. As a 'gold standard' metrology solution for precision optics testing, an interferometric null test comparing the real wavefront from the unit under test (UUT) with the ideal reference wavefront is often configured and performed using a computer-generated hologram (CGH) or null optics such as the Offner null lens. The interferometric null test is modeled and designed using an ideal optical surface shape or an optical system model, such that any deviation from a perfect null (i.e. an exact match between the reference and test wavefronts) will precisely measure the wavefront error, compared to nominal design. This nulling approach has excellent sensitivity and accuracy for measuring a small deviation from the modeled case. As an example, figure 21 shows a view of the Large Synoptic Survey Telescope (LSST) test optics looking up into the test tower from the 8.4 m monolithic primary–tertiary mirror under test. The lower bridge contains the tertiary mirror (M3) null test, and the upper bridge contains the primary (M1) test [119].

In contrast to non-null deflectometry solutions, the interferometric test has a limited dynamic range, since it cannot acquire an interference fringe pattern as the UUT deviates from its modeled form. However, at the same time, its
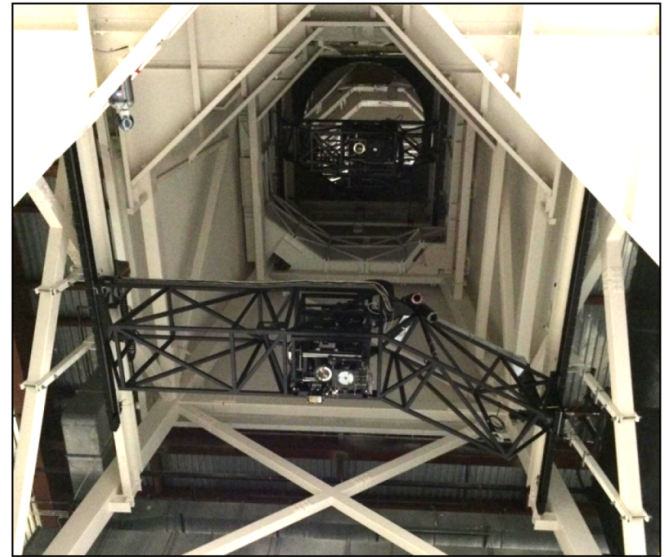

Figure 21. The interferometric LSST optical test configuration in the test tower at the University of Arizona. The lower black bridge contains the M3 nulling interferometry unit, and the upper bridge contains the M1 nulling interferometry unit. Image credit: H Martin.
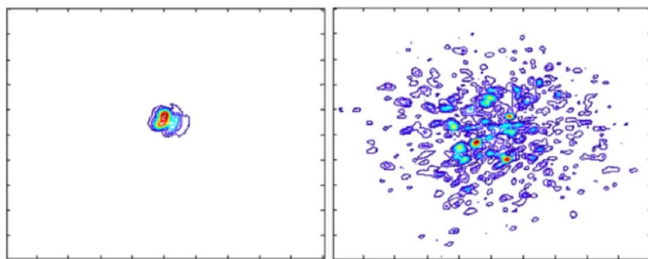
sensitivity and measurement resolution rapidly increase when measuring deviations from the ideal. Therefore, a null test is usually performed on optical components, subsystems, or the full system as a final acceptance test.

3.1.2. CGH interferometry. For aspherical or freeform mirror or lens applications, nulling interferometry typically utilizes a CGH as the nulling optic in an interferometry setup because of the superb accuracies of the holographic patterning process developed by the semiconductor-lithography industry. This high-accuracy aspheric metrology can guide and confirm precision optical-manufacturing processes. For instance, the last step in the computer-controlled optical-surfacing process of the Giant Magellan Telescope (GMT) primary mirror segments, (the telescope has about 13–14 mm of aspheric departure), was guided by the CGH-based interferometry system shown in figure 22. The specific nulling configuration used both fold spheres to accommodate a large portion of the astigmatism in the test wavefront and the CGH to generate the remaining higher-order nulling wavefront components [120]. A typical CGH-based interferometric test usually provides sub-nanometre-level metrology information to guide an optical manufacturing process. The 8.4 m GMT primary mirror was completed with a 20 nm RMS residual error as measured by the hybrid null test [121].

As another great advantage of CGH, diverse holographic alignment patterns can be designed and included outside of the metrology nulling CGH pattern to assist the test-configuration alignment and positioning [122]. Since the auxiliary alignment patterns are lithographically printed on the CGH glass substrate at the same time as the main metrology null pattern, all the holographic patterns are precisely aligned to one another at almost no additional cost.
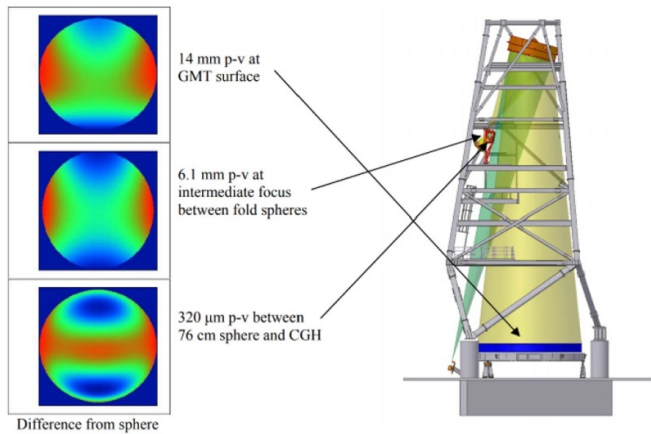
Figure 22. Three-step wavefront control (left) using a hybrid nulling configuration with two fold spheres and a CGH corrector. The interferometer's spherical wavefront is shaped by the CGH, the 76 cm sphere, and the 3.75 m sphere installed in the testing tower (right) to match the GMT primary mirror's ideal aspheric departure. Image credit: H Martin.

3.1.3. Sub-aperture stitching interferometry.

In the era of freeform optics design and manufacturing, sub-aperture stitching interferometry is an important emerging area. In this method, small local sections of the full clear aperture are measured individually in such a way that the entire UUT area is covered by an overlapping array of measurements. For aspherical measurement applications, to generate local nulling conditions, CGH or nulling optical components are often used to create matching wavefronts that are transmitted though lenses or reflected by mirrors under test.

This local nulling interferometric approach is essential when testing highly freeform surfaces or large-aperture convex optics. For instance, the sub-aperture stitching method enables the measurement of steep convex surfaces (e.g. a wide field of view aspheric lens, or a small f-numbered telescope secondary mirror). Traditional null interferometry cannot easily measure large convex apertures because the testing output beam size needs to be larger than the convex surface UUT.

To achieve a series of multiple sub-aperture measurements, the system geometry is systematically adjusted by translating and/or rotating the UUT and/or the interferometer system. A circular sub-aperture is commonly used, and a local nulling is achieved for each section of the UUT. However, since the method does not measure the full aperture at once, various sub-aperture regions can be optimized or adapted, such as the annular region [123] and the elliptical sub-aperture approach [124].

Sub-aperture measurements are stitched together using common features such as fiducials or the common overlapping areas among neighboring sub-apertures. Stitching the individual sub-aperture measurements together may create uncertainties and stitching residual errors. Various algorithms such as modal and zonal fitting can be applied to align and stitch the large local data set to reconstruct the entire surface or wavefront map. For instance, a specialized stitching algorithm has been investigated to manage steep surface measurement cases, which may produce unique residual errors when reconstructing the full metrology map [125].
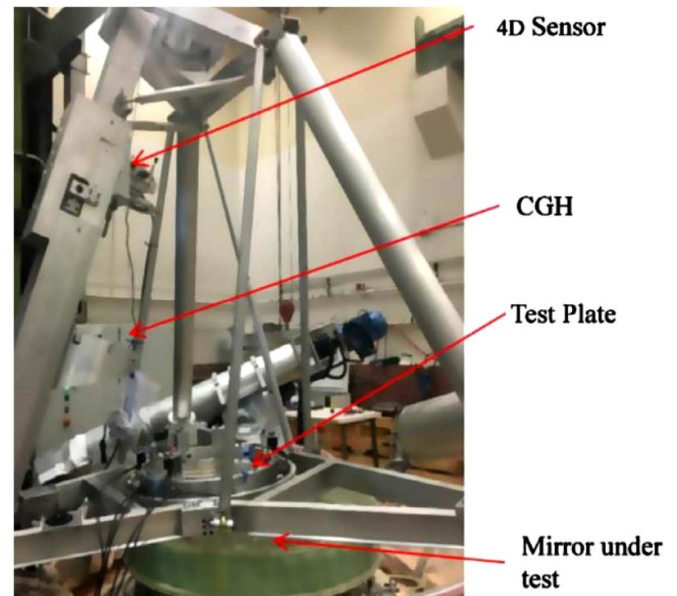

Figure 23. Custom sub-aperture stitching interferometry hardware setup to measure a highly aspheric convex mirror ~1 m in diameter. The 4D sensor is a commercial interferometry sensor by 4D Technology. Image credit: C Oh.

Accurate and precise positioning of the sub-aperture metrology unit within the global coordinate frame is essential to adjust and compensate for the motion and tolerance of the metrology system. A custom-designed and -built sub-aperture interferometric stitching system [126] to test a convex aspheric mirror ~1 m in diameter is shown in figure 23. In this configuration, the CGH was designed to compensate for the majority of the common aspheric wavefront departures, considering all the sub-apertures.

3.1.4. Adaptable interferometry.

Freeform or steep convex optics metrology creates a challenging problem when designing the null testing CGH pattern or the nulling optics for all the sub-aperture local measurement configurations. Several clever methods utilizing reconfigurable null hardware concepts have been developed. An adaptive optical-wavefront nulling to accommodate each sub-aperture measurement region can be accomplished using specialized active optical components such as Zernike plates or prisms [125, 127, 128].

A sub-aperture stitching interferometry setup enabling a precise interferometric form measurement of large convex aspheric optics utilizes a multi-axis hardware platform and an actively rotating CGH pair to minimize systematic metrology errors in each sub-aperture measurement [129]. The overall adaptive interferometer system and the annually stitched map are shown in figure 24.

3.1.5. Instantaneous interferometry.

Single-shot instantaneous interferometry technologies have been developed. These metrology solutions acquire all the measurement data at an instantaneous moment (i.e. single-shot). Such instantaneous capability captures rapidly varying wavefront variations caused by air turbulence or the testing hardware's vibration
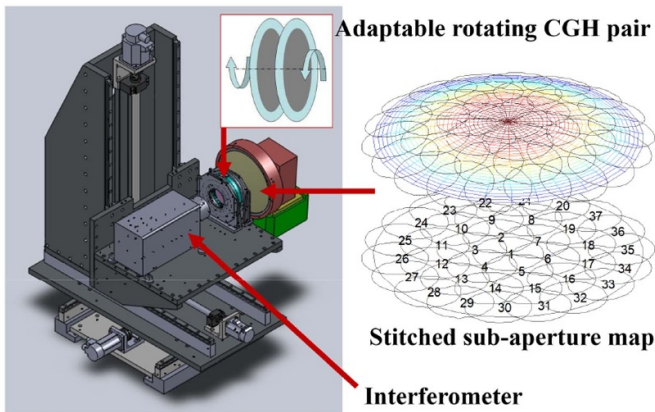
Figure 24. An adaptable sub-aperture interferometry setup, utilizing a multi-axis platform (left) and a rotating CGH pair (inset), enables high-precision convex measurements. The annually stitched entire surface map (right) can be acquired after calibrating for system errors. Image credit: S Chen.

Figure 25. Schematic layout of a visible deflectometry system utilizing a flat display. The camera and monitor are placed near the center of curvature of the UUT. Image credit: D Kim.

during measurements. By measuring and averaging multiple measurements, such short-time-scale random variations can be averaged out. This is especially critical in the context of large astronomical optics testing and manufacturing processes, where the optical testing path lengths easily exceed many meters. Also, these single-shot measurements are used to measure and monitor dynamic motions, as used in, for example, adaptive optics surface metrology during continuous shape changes.

For instantaneous data acquisition, all the information required to calculate wavefront phase unknowns is multiplexed in the single-shot imaging acquisition. For instance, an instantaneous interferometer was designed and built to characterize the dynamic response due to environmental exposure of the flight hardware opto-mechanics of the James Webb Space Telescope (JWST). The high-speed interferometer uses a polarization-based multiplexed phase-shifting method to achieve data collection rates of 1 kHz and 2.25 kHz for detectors with 720×720 pixel and a 400×400 pixel resolutions, respectively. Using instantaneous interferometry, the dynamic structural responses to stimuli applied at varying locations were measured, and the transfer function for the hardware structure was successfully defined [130].

3.2. Optical form deflectometry

3.2.1. Precision deflectometry. The principle of deflectometry, a reverse Hartmann test, is based on an optical source array and an imaging camera with a pixelated detector array to measure local surface slopes across the mirror aperture. An integration step (e.g. zonal or modal) is then required to reconstruct the surface height information from the slope data. Deflectometry is a non-null test method that achieves a high dynamic range.

A typical precision deflectometry system displays a modulated pattern on a pixelated flat screen, and the camera acquires an image of the UUT illuminated by the reflecting (i.e. deflecting) structured irradiance pattern on the display.
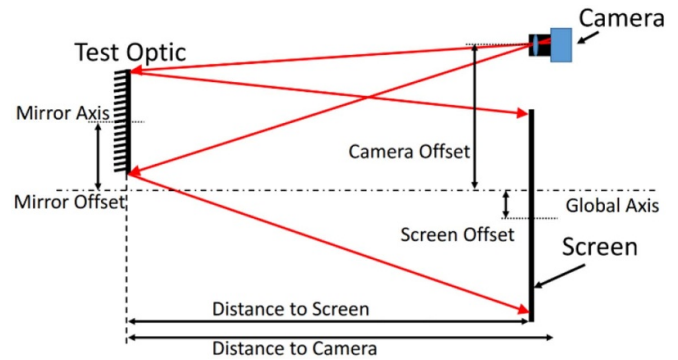
The schematic deflectometry layout is depicted in figure 25 [131]. This test directly measures the local slope distribution of the UUT by tracing the ray path from the display pixel to the camera aperture. This is a non-null approach and provides a large dynamic range (i.e. a measurable error range compared with the nominal shape), which is largely defined by the display size and configuration geometry.

A visible wavelength deflectometry system utilizes an off-the-shelf screen as the light source, which can display various time-varying irradiance patterns, such as sinusoidal phase-shifting patterns. A precisely configured and calibrated visible deflectometry system can make nanometer-level accuracy measurements. As an accuracy demonstration of precision deflectometry, a surface measurement comparison of the GMT primary mirror off-axis segments was made when both deflectometry and interferometry measurements were available. The resulting surfaces formed a data match to <25 nm RMS difference, which lies within the uncertainty level of the metrology systems.

The deflectometry test provides high spatial sampling, defined by its image-acquisition camera's resolution, to measure low-and-mid spatial frequency surface errors with a large dynamic range to cover the changing mirror surface shape during the iterative manufacturing process [131]. The high dynamic range becomes particularly critical during the optics edge figuring process since the surface slopes near the edge of the mirror are often too large for an interferometric null test.

3.2.2. Infrared deflectometry. Visible deflectometry utilizing display panels can measure surfaces that are reflective at the visible wavelengths. In other words, if the optical surface is still in its grinding phase in the manufacturing process chain, the method cannot be applied.

An infrared (IR) deflectometry system can produce height maps with a much higher spatial resolution than other fine-grinding-stage metrology methods while achieving ∼1 μm-level accuracy, which is sufficient to guide the fine-grinding stage when the optical surface roughness is <10 μm RMS [132, 133]. In the case of IR deflectometry, a thermal source such as a heated long metal wire emits in the long-wave infrared (e.g. at a 10 μm wavelength). By
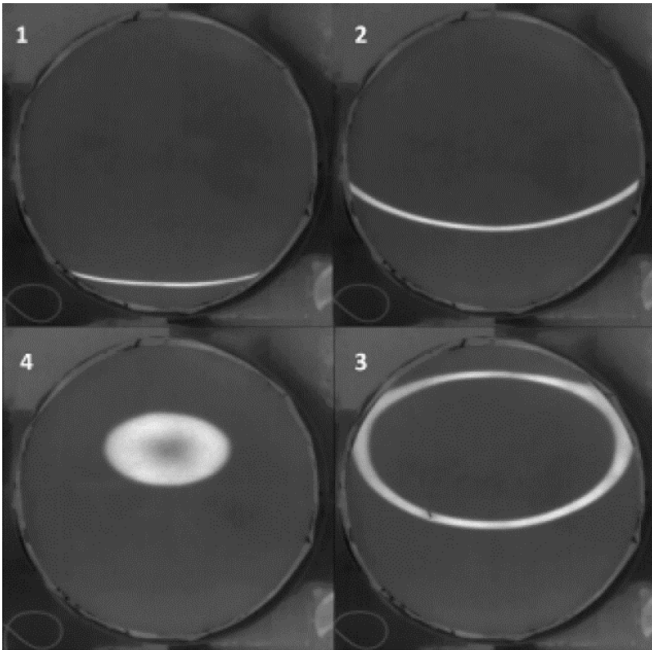
Figure 26. Four sequential IR deflectometry images captured using an IR camera during a hot-wire scanning process. Bright areas have local slopes that reflect the thermal IR light so that it passes through the camera aperture. Image credit: D Kim.

Figure 27. Sub-aperture deflectometry system measuring a high-spatial-resolution local area on the LSST tertiary mirror (M3) right next to the primary mirror (M1) boundary on the monolithic substrate. Image credit: H Martin.

knowing the accurate location of the wire, and measuring the grinding-phase UUT image with an IR camera while the wire is scanning in two orthogonal x and y directions (figure 26), the surface slope is measured through ray path triangulation [18].

The IR deflectometry technique was used during the grinding stage of the 4.2 m-diameter Daniel K. Inouye Solar Telescope (DKIST) primary mirror production, where 25 μm loose abrasives were used [134]. A sequential IR scanning image of the reflected hot wire on the DKIST mirror surface is shown in figure 27. The metrology successfully guided the fabrication from grinding with 25 μm to 12 μm of loose abrasive, which finally resulted in a 1 μm RMS surface before the polishing phase.

3.2.3. Sub-aperture deflectometry. A slope-measuring test using deflectometry and an additional auxiliary lens allows sub-aperture mid-to-high-spatial frequency errors to be measured. The concept of sub-aperture deflectometry is very similar to that of regular deflectometry, which is a reverse Hartmann test using a pixelated display screen and an imaging camera. However, the sub-aperture deflectometry system utilizes an auxiliary lens placed close to the UUT to change the ray paths and allow a wider range of local (i.e. sub-aperture) surface curvatures to be measured. In this configuration, a portable deflectometry system measures convex, flat, and concave parts at a very high spatial resolution with the use of an auxiliary lens. This technology is used for various high-quality optics manufacturing projects, including the 8.4 m LSST mirror as shown in figure 27 [119].
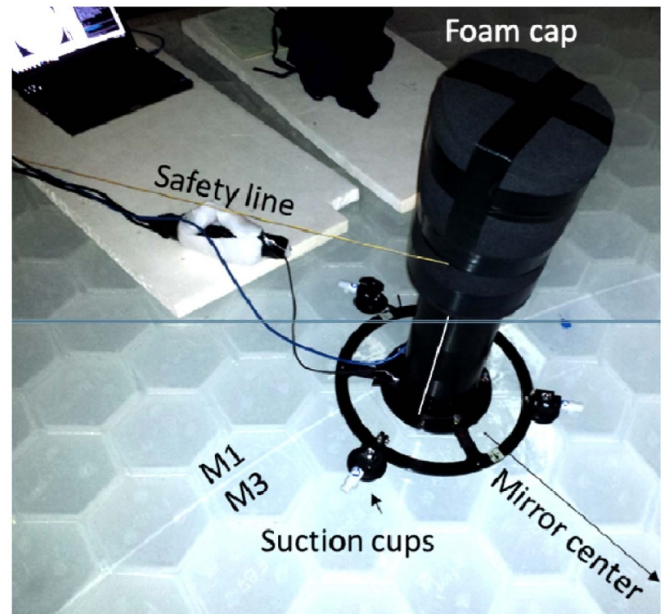
In the context of advanced precision optics manufacturing using a sub-aperture computer-controlled figuring tool, correcting mid-to-high spatial frequency errors is one of the most important aspects during the computer-controlled optical surfacing process. Sub-aperture deflectometry measures mid-to-high spatial frequencies to the nanometre RMS level of accuracy. For the DKIST primary, a deflectometry tool using an auxiliary lens was able to measure surface irregularities from 10 cycles m^{-1} to 1000 cycles m^{-1} over a 125 mm diameter region [134]. It successfully bridged the gap in the power spectral density (PSD) data between the interferometric measurement and the micro-roughness measurement. As shown in figure 28, full coverage of spatial-frequency measurements of the DKIST mirror was achieved using multiple metrology solutions, including sub-aperture deflectometry (a.k.a. SPOTS) [135].

3.2.4. Dynamic deflectometry. Instantaneous deflectometry technologies have been developed to expand the application range of metrology cases that deflectometry systems cover. Instantaneous systems often adopt the sinusoidal phase-shifting technique, but multiplex all the required information in a single pattern, which allows a full deflectometry measurement to be made with a single exposure of the camera. One approach, creating a single-shot deflectometry measurement, uses Fourier transform profilometry, which extracts all the data from a single monochromatic fringe pattern [136]. Another method utilizes color multiplexing to create two fringe patterns, achieving lower measurement errors [137].

Thus, this solution enables dynamic metrology for a continuously moving surface measurement. Applications of this
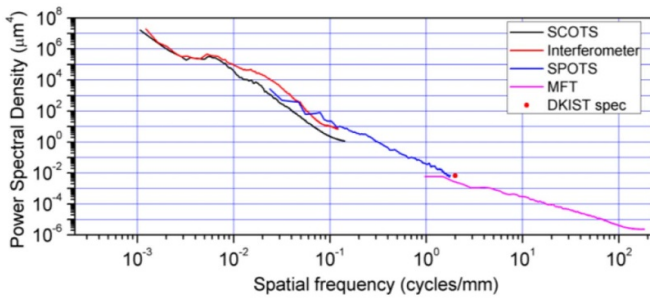
Figure 28. Combined PSD plots from four DKIST measurement systems, visible deflectometry (software configurable optical test system (SCOTS)), CGH-based interferometry, sub-aperture deflectometry (slope-measuring portable optical test system (SPOTS)), and the micro-finish topographer (MFT), along with the computed PSD specification for the DKIST mirror. Image credit: D Kim.
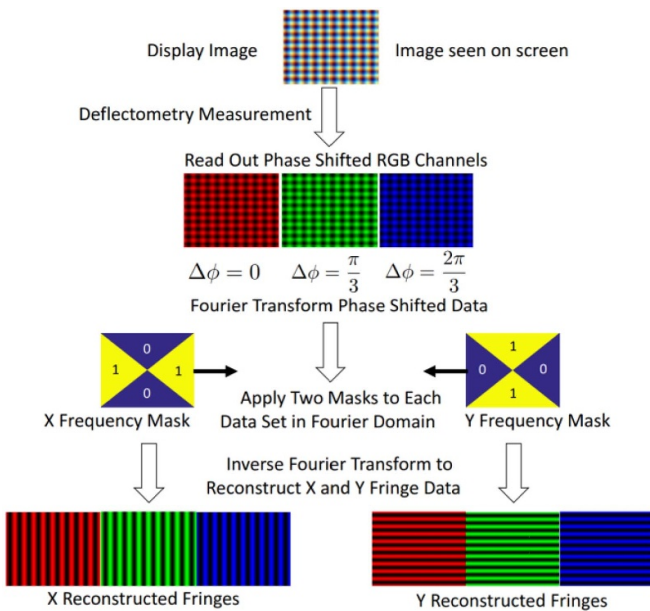

Figure 29. Instantaneous deflectometry pattern and its data-processing flowchart for multiplexing three color channels in the Fourier domain. This approach enables dynamic metrology using a single-shot data acquisition. Image credit: I Trumper.

system range from the measurement of a small deformable mirror to the bending modes of a large optical surface with active supporting actuators. For instance, color multiplexing with Fourier domain filtering also enables instantaneous phase-shifting deflectometry. The multiplexing scheme and data processing flowchart are shown in figure 29. This technology was applied to the characterization of a deformable mirror, and demonstrated a high accuracy at the $\sim$25 nm RMS level, matching an interferometric cross-check measurement result [20].

With the capability of instantaneous measurement, the dynamics of actively controlled precision surfaces are measurable and the surfaces are manufacturable. Also, the large dynamic range advantage of deflectometry is still valid for the instantaneous case, therefore optical testing of a time-varying large-deviation surface is also possible.

3.2.5. Outlook for deflectometry. The four distinct and complementary deflectometry solutions (sections 3.2.1–3.2.4) have their unique advantages and limitations. For instance, standard-precision deflectometry works very well for concave UUT applications, but only for specular surfaces. Infrared deflectometry provides a powerful solution for a ground (i.e. scattering) UUT case, but is less accurate than standard deflectometry. Sub-aperture deflectometry enables higher spatial resolution and sampling of the UUT surface but requires a more complex system configuration including an auxiliary lens. Dynamic deflectometry technology provides excellent temporal resolution for measuring a moving UUT at the cost of lower spatial resolution. There is, as always, no single metrology solution to all problems. However, there might be an optimal solution for a given problem.

There are promising deflectometry parameters and design spaces to be explored, which may improve the measurement performance of advanced deflectometry solutions, such as utilizing a higher resolution/contrast display (e.g. OLED), implementing a time-modulating electro-optic infrared source, and/or installing multiple cameras for simultaneous image acquisition and systematic error calibration.

4. Optical microscopy and scatterometry

4.1. Optical microscopy

4.1.1. Scanning white-light interferometry (SWLI). Laser interferometry has unique advantages of high measurement accuracy and a long measuring range, while suffering from phase ambiguity when surface discontinuity exceeds one quarter of the wavelength of light. This issue can be addressed by using multiple synthetic wavelengths, which can increase the range of phase ambiguity, although this approach unavoidably sacrifices measurement accuracy. On the other hand, SWLI, which employs a short coherence-length white-light source, is a measurement technique that does not suffer from the phase ambiguity problem. Vertical scanning is required for profile sectioning by searching for the peak position, where the measurement arm has a zero OPD with respect to the reference arm. White-light interferometry (WLI), proposed in the early nineteenth century, is not a newly developed technique for precision measurement. Back in 1893, Michelson used white light to estimate the size of a series of step-shaped etalons. This was done as part of the procedure leading to the first comparison of light wavelengths with an international prototype meter [138]. Subsequently, the original Mirau interferometer with a common optical path design was developed and filed as a patented apparatus for measuring OPD using interference to characterize a surface finish [139]. As shown in appendix A, various Mirau-related systems and methods have been further developed and patented to meet diverse demands for better interferometric optical design, vibration-resistant optical design and algorithms, thickness measuring methods, and dynamic measuring methods and strategies. WLI microscopes [140–145] have been widely used for measuring film thickness and monitoring surfaces with discontinuities of
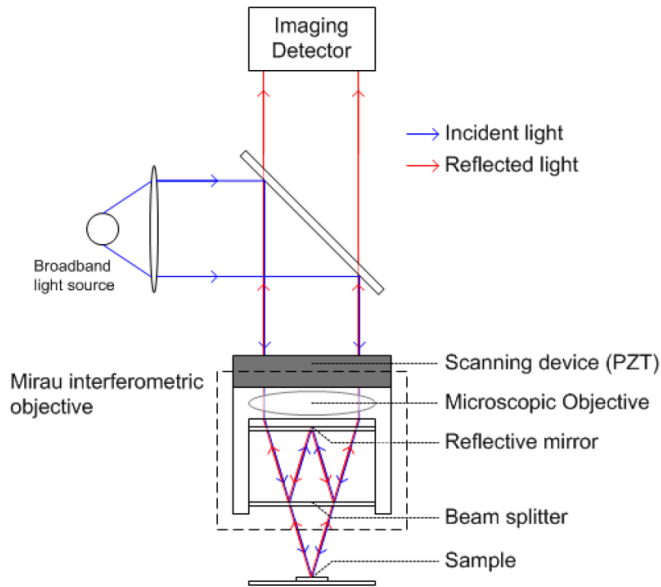
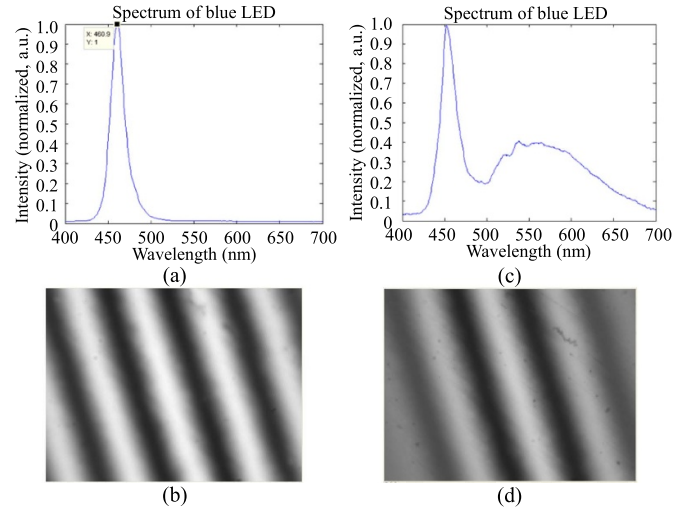**Figure 30.** Classic white-light Mirau interferometric system [148].

Figure 31. Examples of light spectra and the corresponding interferograms: (a) spectrum of a blue LED and (b) interferogram formed by a blue LED; (c) spectrum of a white-light LED; and (d) interferogram formed by WLI (tested sample: flat mirror, magnification of Mirau objective: 20×, NA: 0.4).

more than several wavelengths. In contrast to laser phase-shifting interferometry (PSI) employing a light source with a long coherence length, WLI uses a broadband light source with a short coherence length of approximately 1 μm [146]. Therefore, the interference pattern acquired by WLI is a superposition of the interference patterns of many wavelength components. While PSI uses a monochromatic light source (e.g. laser light) or a quasi-monochromatic light source (e.g. a single-color LED), WLI employs a light source with a broad visible spectrum ranging from 400 nm to 700 nm [144]. A broadband light source has a shorter coherence length than a monochromatic light source and produces an interferogram with OPD-modulated contrast.

The fundamentals of SWLI are introduced in section 4.1.2, followed by the technological advances in *in-situ* SWLI with a literature review of various types of microscopic white-light interferometric profilometry and related references discussing vibration-resistant SWLI (section 4.1.3). Future development trends and challenges are also summarized in section 4.1.4.

4.1.2. Fundamentals of SWLI. Figure 30 shows a schematic of a conventional white-light Mirau interferometric system. As can be seen in the figure, it consists of a broadband light source, a Mirau interferometric objective, a piezoelectric translator (PZT) scanning device for vertical scanning, and a photonic imaging unit for capturing the white-light interferogram. The Mirau interferometric objective splits the light into two different paths, one for the reference mirror and the other for the surface to be measured [138, 147–149]. Then, the light from the two split paths reflected by the surfaces is recombined to form interferograms that can be modeled using the following equation:

$$I_\mathrm{t} = \sum_\lambda \left(I_\mathrm{r}\left(\lambda\right) + I_\mathrm{o}\left(\lambda\right)\right)\left(1 + \gamma \cos\phi\right) \tag{6}$$

where I_r is the intensity of the reference light, I_o is the intensity of the object light, and $\gamma = \sqrt{I_\mathrm{r}I_\mathrm{o}}/\sqrt{I_\mathrm{r}I_\mathrm{o}}\left(I_\mathrm{r} + I_\mathrm{o}\right) - \left(I_\mathrm{r} + I_\mathrm{o}\right)$ and ϕ are the modulation and phase components of the interference fringe, respectively.

Figure 31 shows interferograms formed by a quasi-monochromatic light source and a broadband light source. Figure 31(a) shows the spectrum of a blue LED with a full width at half maximum (FWHM) of 10 nm, and figure 31(b) is the corresponding interferogram. Figure 31(c) shows the spectrum of a 'cool' white-light LED, and figure 31(d) is the corresponding interferogram. A difference in the coherencies of these two cases can be observed, as shown in figures 31(b) and (d).

Fringe modulation in WLI is generated by the superposition of waves from a broadband light source producing different wavelengths. The peak of fringe modulation is the position where all constituent wavelengths have the same phase; namely, the position corresponds to the surface depth where the OPD between the object light and the reference light becomes zero. Hence, as opposed to laser interferometry that utilizes phase information to determine surface depth, WLI uses the maximum position of interferometric fringe modulation for surface reconstruction. In SWLI, vertical-scanning interferometry (VSI) captures interferograms at different heights. For this purpose, vertical scanning is performed at a distance of less than a quarter of the central wavelength of the light source. In contrast with PSI measurement, where the phase is resolved, SWLI calculates the peak of interferogram contrast modulation. VSI involves sampling the interferogram at different heights with a constant interval, reconstructing the interferogram signal, and calculating the peak of the contrast modulation envelope. In WLI measurement, interferogram contrast and the width of the contrast modulation are the two main factors that determine measurement accuracy.

The accuracy of microstructure measurement using SWLI is affected by several types of inherent errors such as batwing effects, ghost steps, field- and tilt-dependent dispersion and variances of surface optical properties. Leach summarized the sources of errors in CSI [150]. The batwing effect is a well-known example that can be observed around a step discontinuity, especially for the case of measuring a step height less than the coherence length of a light source [151, 152]. The occurrence of the batwing effect shows a significant correlation with the measurement parameters of SWLI; in general, the shorter the wavelength, the narrower the batwing size. The batwing effect diminishes when the measurement depth exceeds 1 μm. Wyant first proposed a method combining phase-shifting and coherence-peak-sensing techniques to break the interval-slope limitation of $\lambda/4$ and to avoid the batwing problem [153]. de Groot further developed a strategy by analyzing the difference between the coherence scanning interferogram and the phase profile [154]. Meanwhile, another common error, the so-called ghost step, is regarded as a misclassification of the fringe order attributed to dispersion. This usually occurs at high spatial frequencies where multiple scattering exists. This kind of error was reported in the measurement of flat objects using SWLI [152, 155]. An algorithm was therefore proposed that combines the phase information and the envelope-calculation method [156] to eliminate the ghost steps. Olszak [157] further presented a method measuring OPD changes from the collected interference fringes. The method was found to be effective in correcting the influences of scanning errors and slowly-varying vibrations. Similarly, a dispersive effect associated with ghost steps can make CSI sensitive to surface gradients. Tilt-dependent dispersion, presented by Lehmann [151] in 2006, is often the cause of 2π errors in CSI measurements, even when the tilt is small compared with the numerical aperture (NA) of a Mirau objective. This kind of error depends on the position of an object in the field of view and affects the occurrence of batwing. Leach [152, 155] also indicated that systematic errors exist when the surface gradient is considerably smaller than the acceptance angle of the objective and the mean wavelength of the white light source. In contrast to regular batwing errors, the presence of these phase jumps is systematically position-dependent and generally increases in severity toward the edge of the field of view. This effect also depends strongly on the polarity of the discontinuity, and the dispersive batwing effect causes errors in step height measurement. To overcome these major errors, a dual-wavelength CSI microscope using two LEDs [158] was developed to obtain an accurate surface depth at the position where ghost steps appeared or surface discontinuities such as step heights occurred. Apart from these common errors, the optical properties of the surface to be measured are another important uncertainty source in SWLI. This type of error commonly occurs when the measured surface is made of materials exhibiting different phase changes on reflection or multi-reflection issues [159]. Continuous efforts have been made to minimize these potential errors in SWLI so that the measurement performance can be enhanced to satisfy even higher manufacturing demands.

4.1.3. Technical advancements for in-situ SWLI. Three key factors can be identified for the successful application of SWLI in manufacturing, especially for in-situ AOI; improvement of lateral resolution, adaptability to various surface light variances, and environmental-vibration-resistant capability. Because of their significant effects on the measurement accuracy and precision of SWLI, these factors have been analyzed and studied by many researchers, and significant technological advancements have been made to improve the performance of in-situ SWLI.

4.1.3.1. Improvement of measurement resolution. With microstructures further reduced in size to meet the increasing packaging density of electronic or mechatronic products, the measurement resolution of SWLI becomes extremely crucial. Kino and Chim [160, 161] first tried to resolve aberration problems in the Mirau interferometer caused by the uneven thickness of the beam splitter. The beam splitter in the Mirau designs was replaced by an 800 Å-thick silicon nitride film with a uniformity of 10 Å [162]. The advantage of the correlation microscope lies in enabling phase measurement [163] to achieve a higher measurement accuracy of up to 5 nm using an objective with NA = 0.8. To achieve higher resolution in both the lateral and vertical directions, ultraviolet light was employed to enhance the optical diffraction limit. An optical element inside the interferometer was redesigned to work in the ultraviolet (UV) and deep-UV ranges [164–166]. The key element in the design is the use of nitrogen-rich SiN membranes that are mechanically tough and UV transparent past the 248 nm mercury line, making them best suited for a UV Mirau interferometer. The interferometry attachment that was developed was fixed to a microscope objective with an NA = 0.9, with which the accuracy of SWLI can reach 104 nm. To further enhance the lateral measurement resolution, a Mirau-type interferometer with a confocal slit in the illumination path was developed by combining confocal microscopy and WLI [167]. When measuring a standard target with a pitch of 1.2 μm and a height of 190 nm using the proposed slit integration, the measurement error attributed to the batwing effect can be avoided and the step height can be measured and reconstructed more accurately. Another technique proposed by Lyulko *et al* [168] for increasing the lateral resolution of the Mirau interferometer involved developing an immersion Mirau interferometer to increase the NA. Moreover, simultaneous immersion Mirau interferometry (SIMI), which facilitates the simultaneous acquisition of all interferograms and eliminates the effects of vibration, was developed to achieve 3D one-shot imaging with improved lateral resolution [169]. Polarization Mirau interferometry makes it possible to image live cells in a medium without coverslips. To further enhance the lateral resolution to less than 100 nm (the definition of nanoscopy), many attempts to achieve optical SR have been made in the last two decades [26, 170–182].

In addition to the existing methods illustrated in figure 32, some unconventional sub-diffraction-limit imaging methods have been developed to improve the resolution from the
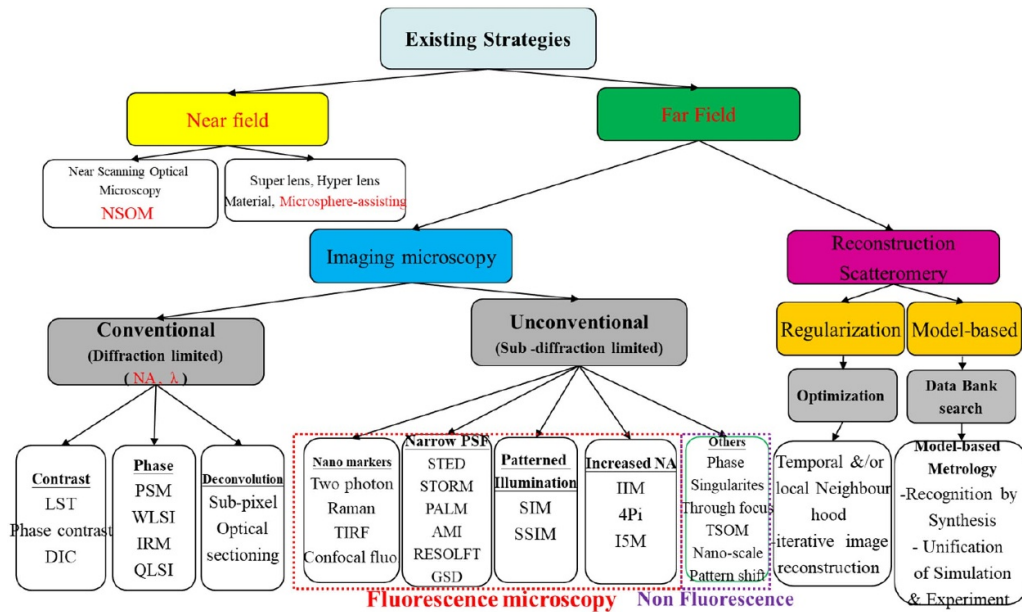
Figure 32. Existing technologies for resolution enhancement: far and near fields.

microscale to the nanoscale. Fluorescence-based methods, such as stimulated emission depletion (STED), stochastic optical reconstruction (STORM), photoactivated localization (PALM), acoustic micro imaging (AMI), reversible saturable optical fluorescence transitions (RESOLFT) and ground state depletion (GSD), have greatly enhanced the resolution to a scale of fewtenths of a nanometre [26, 172–174, 183–185]. Model-based reconstruction methods have also been developed and their feasibility has been demonstrated [183, 184]. However, the development of far-field non-fluorescence imaging microscopy has faced a problem with restricted diffraction limits and still requires technological breakthroughs. Near-field imaging methods, including near scanning optical microscopy (SNOM), superlenses, hyperlenses, metamaterials, and microsphere-assisted microscopy have shown effectiveness in achieving nanoscale resolution [177–179, 185–189]. A time-efficient 3D SR microscopy method involving near-field-assisted WLI was proposed using the near-field imaging concept to achieve lateral near-field imaging through a microspherical superlens [186, 190]. Another microspherical superlens was proved to be effective in transforming near-field evanescent waves into far-field transmitting waves with an imaging lateral resolution of 50 nm and a vertical resolution of 10 nm [191]. Microsphere-assisted WLI microscopy makes it possible to reach a lateral resolution of a few hundreds of nm [188]. In addition to the microsphere-assisted principle, nanoparticle-based metamaterial imaging is also an important emerging method for achieving SR [189]. A propagating incident wave can be scattered by a layer of densely packed dielectric nanoparticles with a diameter of 15 nm as a medium, in which a large nanoscale evanescent-wave illuminating array 15 nm in size can be generated. When a dielectric microsphere with a diameter range larger than the light wavelength or 1–50 µm is positioned close to an object under test (with an air or liquid gap of 100–200 nm), the photons of the near

field, induced by the super-resonance effect (SRE), can be picked up and transformed into propagating waves in the far field, so that an FWHM spot of up to 0.22λ can be generated. Although some breakthroughs have been achieved in near-field imaging, these developments nonetheless require that the objective must be located within an air- or liquid-filled gap of 100–200 nm from the tested surface. Such a working distance is too short and may not be feasible for many applications, especially for *in-situ* manufacturing scenarios. The advantages of these methods are the achievement of full-field, label-free, contactless and non-destructive imaging for AOI. Apart from SWLI, this imaging principle has extensive applications, such as confocal microscopy, endoscopy and differential interferometric contrast (DIC). However, the technical breakthrough for adaptation to *in-situ* AOI will involve resolving the short working distance of the objective, since far-field imaging is definitely essential.

4.1.3.2. Surface light variances. The accuracy of surface-profile reconstruction is determined by the contrast of the interferogram and the coherence length of the light source. A difference in intensity between the reference arm and the object arm is one of the major limitations of SWLI. This limitation makes it difficult to measure objects with low surface reflectivities such as biological samples or highly scattering surfaces, in which the light reflected from the object is much weaker than that reflected from the reference mirror [159]. In the literature, the concept of polarization-based Mirau interferometry was first introduced by Massig [187] in 1992, for detecting changes in the distance of a small reflective measurement surface. Stankewitz then developed a variable epi-illumination interference probe, in which the interferometer was equipped with a variable beam splitter with different reflection and transmission ratios [192].
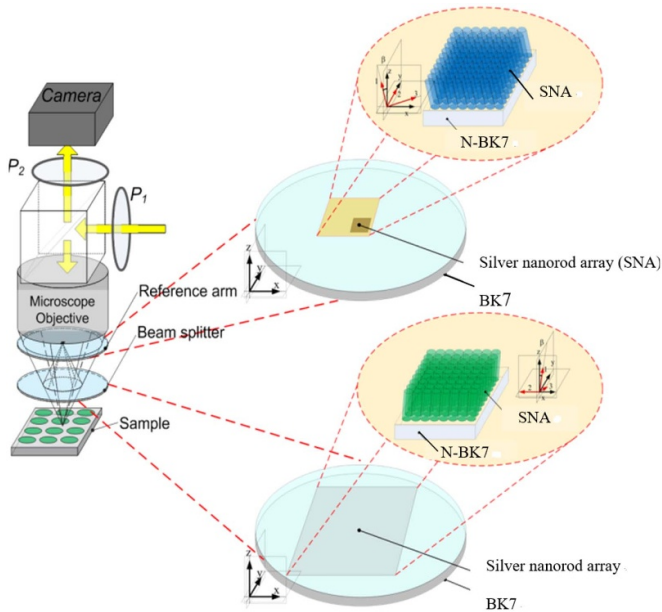
Figure 33. Implementation of a silver NRA in the orthogonal polarization Mirau interferometer developed in [159].

Figure 34. Fabrication process of silver NRA and an SEM image of the silver-coated NRA produced for the reference arm (thickness: 250 nm) [146].

Figure 35. Anisotropic thin film designed as a reflective wave plate [159].

Similarly, Lyulko modified the conventional Mirau interferometer into an orthogonal-polarization Mirau interferometer (OPMI) [168]. The beam splitter in the conventional Mirau interferometer was replaced by a $\lambda/8$ waveplate oriented at 45° relative to the orientation of the incident light. To achieve orthogonally-polarized beams, polarization Mirau interferometry using two quarter-wave plates was proposed by Hariharan and Schmit [193, 194] to generate reference and object light with different polarization states. Using an achromatic phase shifter, which is also a geometric phase shifter, the system enables measurement using white-light PSI. An example of an achromatic phase-shifter configuration is a rotating half-wave plate mounted in the middle of two quarter-wave plates with their axes set at 45° to the angles of polarization of the two beams [195].

More recently, another interesting approach proposed by Chen [159] for balancing the two-arm light difference is a new type of Mirau interferometer which separates light rays in the reference and object arm using orthogonal polarization. Figure 33 presents a schematic of the proposed design of the Mirau interferometric objective [146, 159]. The design involves polarization separation using an optical thin-film coating, with so-called silver nanorod arrays (NRA) and a reflective wave plate. Incident white light is controlled to become linearly polarized at 45° so that the polarization components of the light have equal intensities. Following this, the light passes through a beam splitter and is separated into two components, one reflected toward the reference mirror and the other transmitted toward the tested object. The beam splitter is designed to pass S-polarization and to reflect P-polarization. The reference mirror is designed to reflect P-polarization while suppressing the reflectance of light with S-polarization. This design results in different polarization states of the object beam and the reference beam.
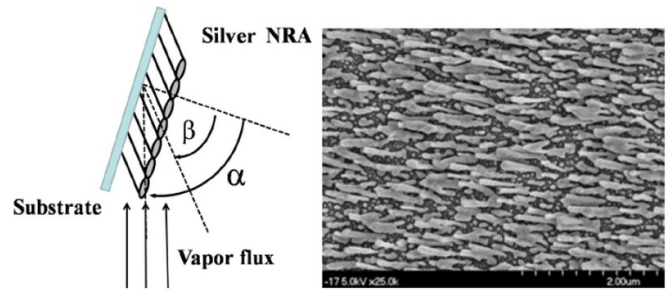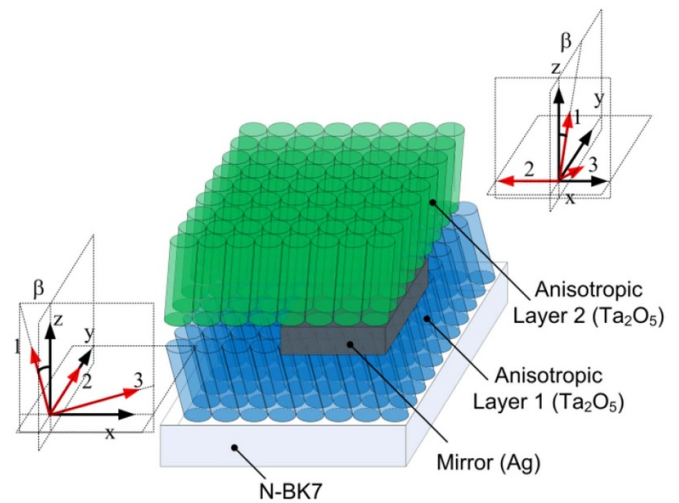
In this design, the silver NRA that was developed is part of the reference arm and is used as a beam splitter of the Mirau interferometer. The thicknesses of the silver NRA coating on the beam splitter and the reference arm are 150 nm and 250 nm, respectively. The silver NRAs are coated at different thicknesses to improve the extinction ratio of the polarization separation. The beam splitter can separate light polarization, and the reference arm is employed to increase the polarization separation of the light. Figure 34 shows a scanning electron microscope (SEM) image of the silver NRA coating used in the reference arm of the interferometer [146, 159]. Figure 35 shows the anisotropic thin film developed as the reflective wave plate [146, 159]. Using electron beam evaporation, a silver mirror is deposited between two anisotropic Ta_2O_5 thin films grown on an NBK-7 substrate with an oblique angle deposition. The three principal refractive indices (n_1, n_2, n_3) and the tilt angle of the columns, β, of the Ta_2O_5 thin film were derived by fitting the angular spectrum to be (n_1, n_2, n_3) = (1.792, 1.653, 1.764) and $\beta = 31°$. The thin film with a thickness of 1542 nm serves as a reflective half waveplate configured as NBK-7 glass/film/silver. Figure 36 compares the 3D reconstructed results of printed circuit board (PCB) bumps obtained by conventional WLI and the OPMI. As can be seen, the OPMI can obtain a higher S/N ratio result in its 3D reconstruction.

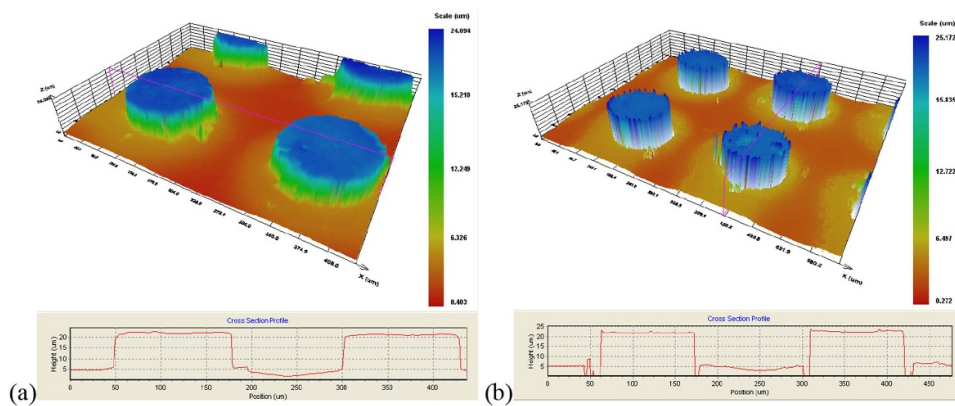**Figure 36.** 3D map and cross-sectional profile of a printed circuit board (PCB) bump measured using (a) an OPMI and (b) conventional WLI [159].

Apart from the issue of light imbalance mentioned above, measuring an optically rough surface using WLI does not guarantee the resolution of the lateral structure of the tested surface because the height difference of neighbouring pixels may exceed the phase ambiguity limit of $\lambda/4$ [196, 197]. Moreover, because the measurement errors of WLI are limited by a random shift of individual interference patterns, an effective strategy was developed to reduce the measurement uncertainty of WLI by sequentially switching the direction of illumination [198]. In summary, the measurement uncertainty of SWLI becomes extremely crucial as *in-situ* AOI faces even stricter measurement tolerance requirements. The allowable measurement uncertainty of SWLI is often only a few nanometres at $\pm 3\sigma$ with a confidence level of 99.7%. An effective reduction of the measurement uncertainty can be achieved by controlling and manipulating the surface light variances which may occur in SWLI.

4.1.3.3. Vibration-resistant capability. In-situ SWLI faces many measurement error sources such as environmental ground or mechanical vibrations, acoustic disturbances, and nonlinearity of the PZT used for axial scanning [143]. Although the general strategy is to perform SWLI on a vibration-isolation table to minimize vibration, there exist unavoidable and undesirable vibrations in an uncontrollable shop floor situation with air disturbance coming from an air conditioner and machine acoustic noises as well as human voices. To resolve this critical issue, some in-situ techniques and strategies have been developed, such as active vibration isolation using a fringe locking mechanism, shortening measurement time, and performing simultaneous PSI, [199–215]. Early research was devoted to active feedback in laser interferometry, either by using adaptable wavelength modulation [201, 212–215] or active control of the reference arm [202–207]. Some strategies using active feedback control of low coherent phase-shifting were also applied to biomedical testing [216–218], with some effectiveness shown in measurement error correction. Meanwhile, phase-shifted errors caused by undesirable vibration in PSI were reduced

using multi-sensors, a frequency shifter, or an acousto-optic modulator (AOM) for accurate detection of vibration-induced shifted error for phase compensation [219–221]. However, the frequency-shifting modulation developed is only applicable to point measurement and not for full-field imaging.

To address vibration in SWLI, phase-shifted errors were corrected using a reference interferometer [216, 217], in which the nonlinearity of the PZT was corrected to reduce measurement uncertainty. Similarly, using wavelength scanning interferometry, another method was developed to compensate for environmental noise in vibration detection and compensation [218]. The main limitation faced by these methods is an insufficient bandwidth for vibration detection and compensation. To resolve this, Chen [143, 219–221] proposed a dual-sensing optical configuration (shown in figure 37) to precisely detect the vibration displacement of the Mirau objective and developed an active fringe-locking strategy to immobilize low-coherence interferograms with a high bandwidth capable of suppressing various environmental vibrations with a frequency up to a few hundreds of Hz. The method developed for vibration-induced phase correction was proved effective by an improvement of more than six times and a response bandwidth up to several 100 Hz can be realized by developing a real-time embedded controller. As well as active feedback compensation in SWLI for vibration minimization, passive vibration compensation in SWLI was also proposed [222, 223]. The advantage of these methods is that no additional active compensation-system hardware is required. The basic principle is to detect the precise position of the interferometer with respect to the measuring object to compensate for phase errors caused by environmental vibrations or scanner nonlinearities. Another strategy is to use the shape information of tested objects for vibration compensation [223]. However, in most cases, the shape information cannot be precisely predetermined. More recently, SWLI with *in-situ* vibration compensation was reported for shop-floor depth measurements in a deep reactive ion etcher [224]. Vibration-compensated SWLI has thus been demonstrated to be essential for *in-situ* AOI and other applications in various fields.
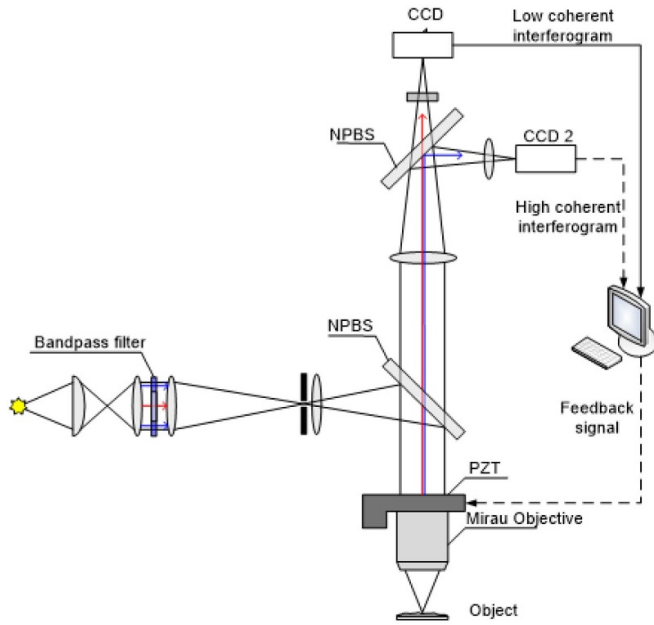
Figure 37. Illustration of dual-sensing optical configuration for SWLI fringe locking.
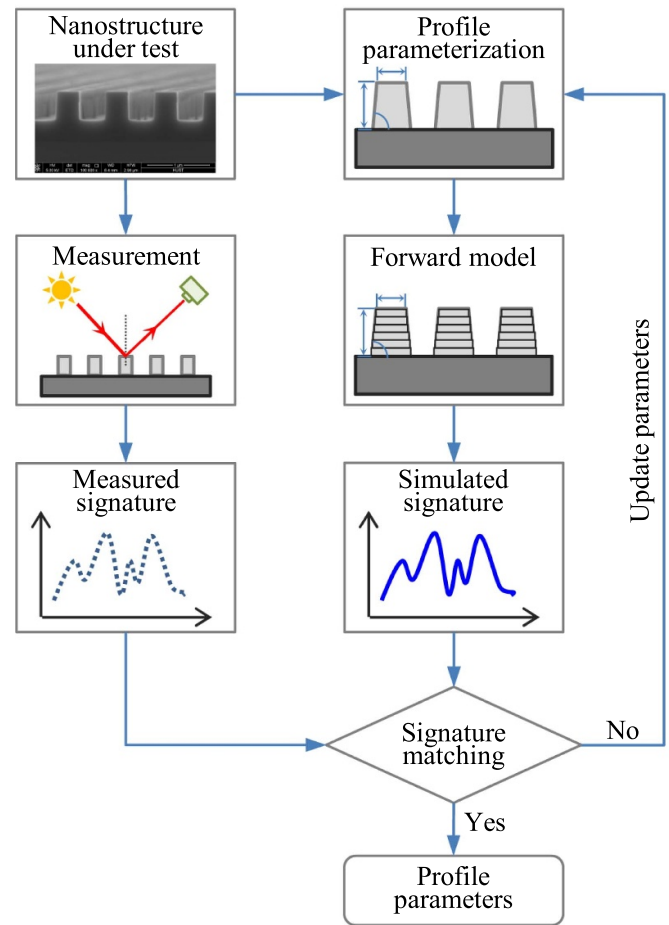
4.1.4. Future development trends and challenges. A literature review on the technical advancements in SWLI, a discussion on the three important measurement properties affecting in-situ SWLI, and analyses of the important developments for effective solutions have been addressed. From the perspective of technological breakthroughs, the most critical measurement parameter affecting SWLI is the improvement of lateral resolution because the current optical resolution is still restricted to the micrometre or sub-micrometre scale. This is mainly caused by optical light diffraction limits which restrain the PSF of white light to approximately 1 mm. Most current SR methods (STED, PALM, STORM) are essentially limited to fluorescence microscopy and specific markers, and therefore, not commonly applied for general dimensional metrology in *in-situ* AOI. With strong advantages in terms of measuring speed, in-line capability, freedom from contamination, and comprehensive theoretical support from Maxwell's equations, model-based simulation methods can play an important role in SWLI metrology for nanoelectronics and other nanotechnologies. SR optical microscopy using metamaterials in SWLI has been proven to enable excellent high-resolution qualitative imaging in many applications and foster novel in-depth studies in fundamental research. Nevertheless, current optical SR metrology still requires significant effort to ensure high traceability and reliable uncertainty estimation, which merit further intensive investigation.

In addition, the effective reduction of measurement uncertainty can be achieved by controlling and manipulating surface light variances which may occur in SWLI. The epi-illumination interference design and the polarization-based Mirau interferometric principle have been proven effective in balancing the difference in light intensity between the reference and object arms. Given the significant impact of SWLI measurement uncertainty on *in-situ* AOI, a measuring

Figure 38. Overview of the principle of optical scatterometry.

tolerance of a few nanometres at a high confidence level is definitely required for advanced manufacturing processes, such as semiconductor fabrication. Moreover, vibration-compensated SWLI has thus been proven essential for *in-situ* AOI and other applications in various fields.

4.2. Optical scatterometry

Optical scatterometry is a technique that measures and analyzes light diffracted by periodic nanostructures. As illustrated in figure 38, the implementation of optical scatterometry involves two main steps [7, 27, 225]. In the first step, the optical signature of a nanostructure under test is measured by a proper scatterometric setup. Here, the term 'signature' represents the optical response of a sample, which is a macroscopic reflection of the microscopic structural profile and the material properties of the sample. The second step involves first parameterizing the profile of the nanostructure under test according to prior knowledge, then establishing a forward scattering model to relate the profile parameters to the signature, and finally extracting profile parameters from the measured signature by solving an inverse scattering problem. In the solution of the inverse problem, the profile parameters that are the inputs of the forward model are constantly adjusted until the simulated signature reaches the best match for the measured one.

In comparison with image-based metrology techniques, which normally allow for the direct determination of dimensional information from the best-focus images acquired, measurement in optical scatterometry is not a 'what you see is what you get' (WYSIWYG) (process, but involves the solution of a complicated inverse-scattering problem. Nevertheless, optical scatterometry is not restricted by the Abbe diffraction limit that is encountered in image-based metrology techniques. Due to its high-throughput, non-destructive, and ease of in-line integration merits, optical scatterometry is widely used in the measurement of CDs and overlays in semiconductor manufacturing [226–231].

In this section, we will give a brief review of optical scatterometry, with an emphasis on the two main steps involved in its implementation.

4.2.1. Scatterometric setups.

Considering a periodic structure such as a grating, its optical response is governed by the well-known grating equation:

$$\sin\theta_i + \sin\theta_m = m\frac{\lambda}{\Lambda}, \qquad (7)$$

where θ_i is the incidence angle, θ_m is the scattering (diffraction) angle associated with the m-th diffraction order ($m = 0$, ± 1, ± 2, …), λ is the wavelength of the incident light, and Λ is the period (pitch) of the structure. There are many different types of scatterometric setups that can be used to collect the diffraction information of the structure under test. As shown in figure 39, these scatterometric setups, according to the incidence angle θ_i, the scattering angle θ_m, and the wavelength of incident light λ, can be basically categorized into the angular scatterometer and the spectroscopic scatterometer [7, 27, 225].

4.2.1.1. Angular scatterometers.

The 2-θ scatterometer is a typical angular scatterometer which was proposed by McNeil and Naqvi *et al* for the measurement of short-pitch structures [232, 233]. In the 2-θ scatterometer, as shown in figure 39(a), a monochromatic light source, such as a He-Ne laser source ($\lambda = 632.8$ nm), is incident upon a structure under test with an incidence angle of θi, and the reflectance or transmittance are acquired by scanning the incidence and the corresponding zeroth-order diffraction angles. There are two main reasons for only collecting the zeroth-order diffracted beam ($m = 0$ in equation (7). First, the zeroth-order diffracted beam usually has a larger intensity than higher-order diffracted beams, which thus provides a higher signal-to-noise ratio in the measurement. Second, the zeroth-order diffracted beam always exists, irrespective of the ratio of λ/Λ and θi according to equation (7). A variant of the 2-θ scatterometer is the so-called optical Fourier transform scatterometer [234, 235], which employs a high NA objective to measure the reflectance for all incident angles simultaneously without any mechanical movement.

In another type of angular scatterometer, shown in figure 39(b), the detector is scanned or an area array detector (e.g. a CCD camera) is used to record the intensities associated with different scattering angles θ_m. To distinguish it from the 2-θ scatterometer, we call this type of angular scatterometer a scattering-angle-resolved scatterometer (The 2-θ scatterometer can be regarded as an incidence-angle-resolved scatterometer). To ensure that there is enough scattering information available for accurate profile reconstruction of short-pitch structures, light sources with short illumination wavelengths, such as an extreme ultraviolet (EUV) light source [236–239] or an x-ray light source [240–243], can be employed in scattering-angle-resolved scatterometers.

4.2.1.2. Spectroscopic scatterometers.

Compared with angular scatterometers, as shown in figure 37(c), spectroscopic scatterometers usually adopt broadband light sources. Similar to the 2-θ scatterometer, most of the spectroscopic scatterometers collect the reflected (or transmitted) zeroth-order diffracted beam. Also, according to equation (7), the structure will separate white light from the broadband light source into a spectrum with different propagating directions at higher diffraction orders. However, all wavelengths from the white light propagate in the same direction at the zeroth-order diffraction, which thus facilitates signal detection. A spectrograph is usually required in the spectroscopic scatterometer to acquire spectral information from the zeroth-order diffracted beam.

The ellipsometric scatterometer is a typical type of spectroscopic scatterometer, as shown in figure 39(d), which applies spectroscopic ellipsometry (SE) to the measurement of periodic nanostructures. Ellipsometry is an optical measurement technique that characterizes thin films (by, for example, film thickness and optical constants) based on the change in polarized light before and after the light is reflected (or transmitted) by a sample [244, 245]. Around the year 2000 [246, 247], ellipsometry was introduced to the measurement of CDs of grating structures. As shown in figure 39(d), a polarization state generator (PSG) and a polarization state analyzer (PSA) are usually mounted in the light input and output paths of an ellipsometric scatterometer, respectively. The PSG and PSA are both comprised of polarization components, such as polarizers and retarders, which are respectively used to modulate and demodulate the polarization states of reflected (or transmitted) light beams.

The conventional spectroscopic ellipsometer typically measures two ellipsometric angles, Ψ (the amplitude ratio) and Δ (the phase difference), and is most suitable for characterizing isotropic samples. For anisotropic samples and/or if the measurement process contains depolarization, it is necessary to use Mueller matrix ellipsometry (MME), which provides up to 16 elements of a 4×4 Mueller matrix. Due to the rich information contained in the Mueller matrix, Mueller matrix ellipsometric scatterometry (also known as MME-based scatterometry or Mueller matrix scatterometry) has demonstrated great potential for the accurate measurement of CDs and overlays in semiconductor manufacturing [248–254].

Table 5 presents an overview of scatterometry techniques. Although we categorize the scatterometry techniques into angular scatterometry and spectroscopic scatterometry,
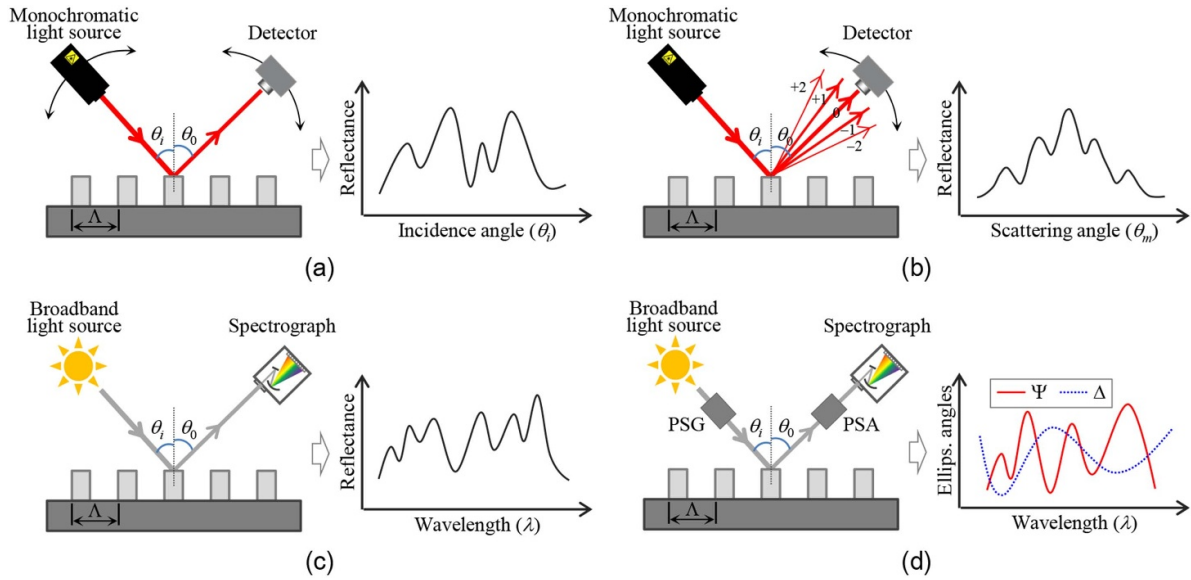
Figure 39. Schematic of different scatterometric setups. (a) and (b) Angular scatterometers; (c) and (d) Spectroscopic scatterometers.

it should be noted that actual scatterometry is commonly a combination of different scatterometry techniques. For example, a tunable light source and a polarizer are often used in a practical 2-θ scatterometer to improve measurement sensitivity. For scattering-angle-resolved scatterometry and spectroscopic scatterometry, the incidence angle is not always fixed but can be operationally adjusted for better measurement sensitivity and parameter decorrelation.

4.2.2. Model-based data analysis. The model-based data analysis procedure involves parameterizing the structural profile of a sample under test, establishing a forward scattering model, and solving an inverse-scattering problem to extract profile parameters from the measured signature. Although both the structural profile and the material properties of a sample influence its optical signature, the material properties (optical constants) are usually pre-determined to address the parameter correlation issue in model-based data analysis. We will not review the determination of the optical constants of materials here, but recommend that the reader consults related references about SE [244, 245]. Next, we will briefly review the three aspects involved in model-based data analysis, namely structural profile parameterization, forward modeling, and inverse-problem solving.

4.2.2.1. Structural profile parameterization. The aim of structural profile parameterization is to find a group of parameters that can characterize the profile of a structure under test. We exemplify structural profile parameterization using a one-dimensional (1D) periodic structure. As shown in figure 40, the dotted rectangle shows a periodic unit of a 1D periodic structure. In general, the structural profile parameterization for this structure is to find parametric equations $w = f(z)$ and $\delta = g(z)$ ($z \in [0,h]$), which describe the width at z and the corresponding offset of the middle point of the width with
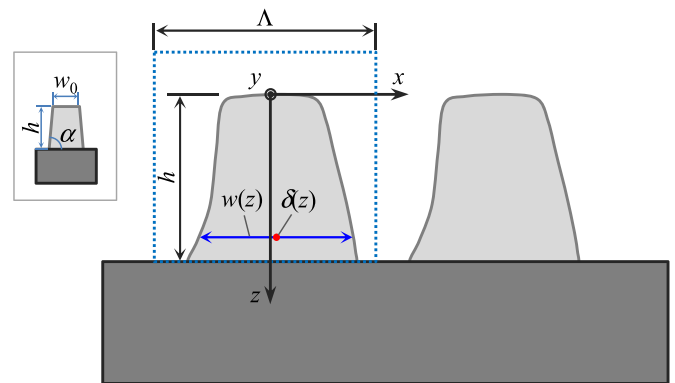
Figure 40. Parameterization of the structural profile of a 1D periodic structure. The dotted rectangle shows a periodic unit of the structure.

respect to the origin of the coordinate, respectively. Specifically, for a trapezoidal profile as shown on the top left corner of figure 40, we have $w = f(z) = 2z \cot \alpha + w_0$ and $\delta = g(z) = 0$ ($z \in [0,h]$). So, the trapezoidal profile can be characterized by three parameters: a top CD w_0, a sidewall angle α, and a height h. However, for a more complex profile, more complex parametric equations need to be adopted. For example, Huang and Terry Jr. used quadratic polynomials to characterize the line shapes of photoresist gratings [255]. Chen *et al* also used quadratic polynomials to characterize the asymmetric profiles of nanoimprinted patterns [256].

Besides polynomial parametric equations, Bézier curves and B-splines can also be used for structural profile parameterization. Wurm *et al* used a Bézier-curve-based geometry model to characterize the profiles of Si gratings [257]. As opposed to polynomial parametric equations, the Bézier-curve-based or B-spline-based models characterize structural profiles by adjusting the coordinates of control points [258].

Table 5. Overview of scatterometry techniques.

Technique	Pros	Cons
Angular scatterometry	• Since a single wavelength is used, no assumption about dielectric functions of the sample materials is required for data analysis • Structural pitch can be measured simultaneously for scattering-angle-resolved scatterometry • Relatively easy to extend to short-wavelength ranges, such as EUV and x-ray	• Contain moving components for 2-θ scatterometry as well as some scattering-angle-resolved scatterometry techniques using goniometers, which limit the measurement speed • Significant experimental setup required, especially for scattering-angle-resolved scatterometry
Spectroscopic scatterometry	• Measurement can be very fast, especially for spectroscopic-reflectometry based scatterometry • Very high vertical resolution (sub-nm) for ellipsometric scatterometry • More measurement information can be acquired, especially for MME-based scatterometry, which is beneficial for parameter decorrelation in data analysis	• Need to pre-determine optical constants of sample materials in a broad spectral range • Need achromatic optical components and detectors with broad spectral responsivity • Need delicate calibrations for accurate measurement, especially in ellipsometric scatterometry

4.2.2.2. Forward modelling. Many methods have been developed for modeling light–nanostructure interactions: the finite-element method [259, 260], the boundary-element method [261, 262], the finite-difference time-domain method [263], and the rigorous coupled-wave analysis (RCWA, also known as the Fourier modal method) [264, 265], to name just a few. All these computational methods start from the basis of Maxwell's equations, and the main difference between them lies in the specific numerical techniques used to solve the governing equations and boundary conditions. Among these methods, RCWA is the most commonly used one in optical scatterometry, due to its good convergence and relatively easy implementation in programming languages.

We take the 1D grating as an example to briefly illustrate the principle of RCWA. For more details, we recommend the readers to consult [264] as well as other related literature. As shown in figure 41(a), for a binary rectangular-groove grating, both the permittivity of the grating region and the electromagnetic fields are first expanded into Fourier series. The tangential field components are then matched at the upper and lower boundaries of the binary grating, and thereby the boundary-value problem is reduced to an algebraic eigenvalue problem. Consequently, the reflection coefficient associated with each diffraction order can be calculated by solving the eigenvalue problem. According to the reflection coefficients, we can further calculate the reflectance (transmittance), ellipsometric angles, and Mueller matrices, etc [7].

To apply the calculation to a surface-relief grating with a more complex profile, as shown in figure 41(b), it is necessary to first slice the structural profile along the z-direction into multiple-layer small rectangles; each slice is then addressed using the same approach as that described for the binary grating above, and the continuity conditions of the tangential field
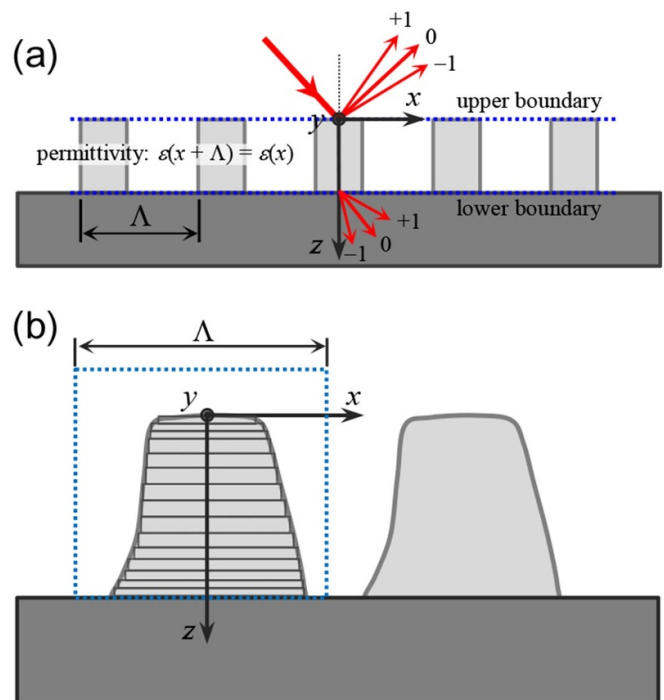

Figure 41. (a) Representation of the light incident upon a 1D binary rectangular-groove grating; (b) slicing the profile of a 1D surface-relief grating into small rectangles.

components are then applied to the upper and lower boundaries of each slice to connect all the related linear equations. The reflection coefficients are finally obtained by solving these linear equations.

Kogelnik presented an embryonic form of RCWA in 1969 for the calculation of the diffraction efficiencies of thick hologram gratings [266]. Moharam and Gaylord first formulated RCWA for planar gratings [267–269] and then extended it to surface-relief gratings [270, 271] and 2D gratings [272]. The RCWA method then received extensive attention and research. In the development of the RCWA method, two issues perplexed researchers for a long time. One was the slow convergence rate for TM polarization of metallic gratings [271], and the other was the poor stability of the calculation of deep surface-relief or multi-layer gratings [270].

Lalanne [273] and Granet [274] *et al* found in 1996 that the convergence rate for metallic gratings in TM polarization can be dramatically improved by reformulating the eigenvalue problem of the RCWA method. However, the underlying cause remained unclear to them. Li subsequently found that the poor convergence for metallic gratings in TM polarization was caused by an incorrect treatment of permittivity in the truncated Fourier space, and further presented the Fourier factorization rules for obtaining faster convergence [275]. Li's factorization rules can easily be applied to 1D gratings, but applying them to 2D gratings is more complicated, since the decomposition of the electric field into parallel and perpendicular components is less obvious for 2D gratings.

To improve the convergence rate for the 2D case, in 1997 Lalanne presented a new formulation of the RCWA method by introducing a free parameter α to weigh the relative strengths of the Fourier transformed matrices of the permittivity and the inverse of the permittivity [276]. However, it is noticeable that the free parameter α can be easily determined for 2D rectangular gratings, but it is hard to determine for 2D gratings with complex contours. At the same time, Li proposed the discretization of the original grating contour by zigzag contours that satisfy Li's factorization rules [277]. Schuster *et al* introduced a normal vector method [278] that fulfills Li's rules by combining the classical RCWA with Popov and Nevière's formulation of the differential method [279]. However, the normal vector method requires a normal vector field that relies on structural geometry and does not apply to arbitrary structures. Götz *et al* extended the normal vector method with automated vector field generation for arbitrary structures [280].

The poor stability in the calculation of deep surface-relief or multi-layer gratings was due to the accumulation of numerical errors generated in the solution of the eigenvalue problem associated with each slice or each layer. Moharam *et al* introduced an enhanced transmittance matrix (T-matrix) approach that was shown to produce numerically stable results for deep multilevel surface-relief dielectric gratings [265]. Li systematically presented two recursive and numerically stable algorithms, the *S*-matrix algorithm and the *R*-matrix algorithm, for modeling multi-layered diffraction gratings [281]. It was also demonstrated that the *S*-matrix algorithm is preferable to the *R*-matrix algorithm in terms of numerical efficiency. Tan proposed an enhanced *S*-matrix algorithm [282] and an enhanced *R*-matrix algorithm [283] to further improve the numerical efficiency of the original *S*-matrix and *R*-matrix algorithms, respectively.

4.2.2.3. Inverse problem solution. Assume that the structural parameters being measured are represented as an M-dimensional vector $\boldsymbol{x} = [x_1,x_2,\ldots,x_M]^{\mathrm{T}}$, where the superscript 'T' denotes a matrix (or vector) transpose and x_i ($i = 1,2,\ldots,N$) correspond to the parameters used to describe the parameterized structural profile as illustrated in section 4.2.2.1. The measured signature is given by an N-dimensional vector as $\boldsymbol{y} = [y_1,y_2,\ldots,y_N]^{\mathrm{T}}$, where y_k ($k = 1,2,\ldots,N$) can be, in terms of reflectance (or transmittance), ellipsometric angles, Mueller matrix elements, etc., collected by the above scatterometric setups at different wavelengths and/or different incident (or scattering) angles. The corresponding theoretical signature calculated by RCWA for any structural parameter vector $\boldsymbol{x}$ is given by $\boldsymbol{F}(\boldsymbol{x}) = [f_1(\boldsymbol{x}),f_2(\boldsymbol{x}),\ldots,f_N(\boldsymbol{x})]^{\mathrm{T}}$. The χ^2 function in statistics is usually used to estimate the matching (fitting error) between the measured and simulated signatures, which is defined by

$$\chi^2 = \sum_{k=1}^{N} w_k[y_k - f_k(\boldsymbol{x})]^2 = [\boldsymbol{y} - \boldsymbol{F}(\boldsymbol{x})]^T \mathbf{W}[\boldsymbol{y} - \boldsymbol{F}(\boldsymbol{x})], \quad (8)$$

where w_k are the weighting factors, which are usually chosen to be the inverse of the variances of the measured signature $\sigma^2(y_k)$ i.e. $w_k = 1/\sigma^2(y_k)$, and $\boldsymbol{W}$ is an $N \times N$ diagonal weighting matrix with the diagonal elements w_k. With the above notations, the inverse problem in optical scatterometry can be mathematically formulated as a least-squares regression problem such that

$$\hat{\boldsymbol{x}} = \underset{\boldsymbol{x} \in \Omega}{\arg\min} \left\{ [\boldsymbol{y} - \boldsymbol{F}(\boldsymbol{x})]^T \mathbf{W}[\boldsymbol{y} - \boldsymbol{F}(\boldsymbol{x})] \right\}, \quad (9)$$

where $\hat{\boldsymbol{x}}$ is the expected solution of the inverse problem and Ω is the parameter domain.

Many methods can be used for solving equation (9), which can overall be categorized into the nonlinear regression method and the library search method [284]. As schematically illustrated in figure 42, the nonlinear regression method iteratively adjusts the structural parameter vector $\boldsymbol{x}$ using some optimization algorithms [285, 286], such as the Gauss–Newton algorithm and the Levenberg–Marquardt algorithm, until the simulated signature $\boldsymbol{F}(\boldsymbol{x})$ best matches the measured signature $\boldsymbol{y}$. In the library search method, a library of simulated signatures is constructed first, and then the signature library is searched to find a best-match signature for the measured signature. The structural parameter vector that corresponds to the best-match simulated signature in both the nonlinear regression method and the library search method is taken to be the solution of the inverse problem.

Table 6 presents a comparison between the nonlinear regression method and the library search method. The nonlinear regression method can achieve an accurate solution, provided that the structural parameter vector $\boldsymbol{x}$ is assigned an appropriate initial value during the iteration. Since the solution in the nonlinear regression method is achieved by an iterative approach and the RCWA calculation needs to be performed for each iteration, the nonlinear regression method is typically time-consuming, especially for 2D periodic structures. Therefore, the nonlinear regression method is not suited for inline
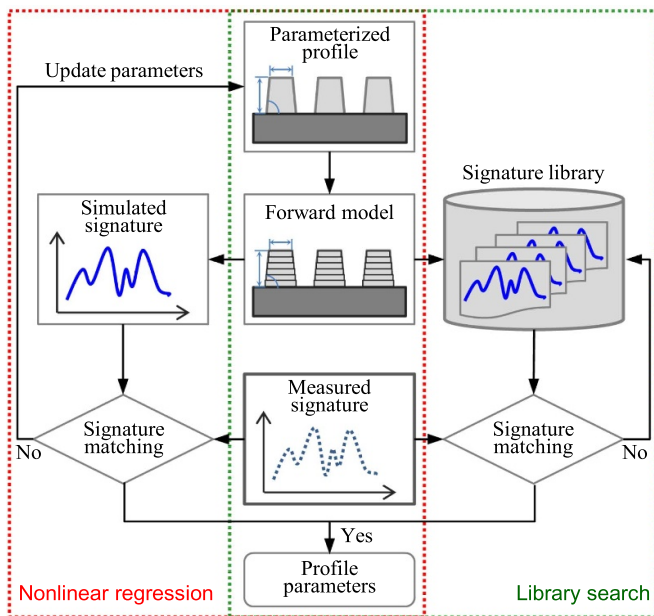
Figure 42. Flowchart of the nonlinear regression method and the library search method.

applications. In comparison, although the offline construction of a signature library is time-consuming, the library search itself can be done quickly and a global solution is guaranteed [284]. Thus, the library search method is well suited for inline applications. However, the solution accuracy of the library search method relies on the structural parameter interval (grid interval) used in the construction of the signature library. A finer grid interval can achieve a higher solution accuracy but will impose an extra burden on time and space resources to generate and store simulated signatures. To increase the solution accuracy for a given signature library, improved library search methods with interpolation of the signature or of the fitting error need to be adopted [287, 288].

4.2.3. Future trends. With the development of advanced photolithography processes and techniques such as multiple-patterning, directed self-assembly, and EUV lithography, very-large-scale integrated circuits (ICs) have broken through to the 7 nm process and are expected to continue towards a 1 nm process [289]. To guarantee the performances of IC devices with ever-decreasing feature sizes, logic devices have transitted from scaling-driven planar devices (e.g. complementary metal-oxide semiconductors) to 3D transistor architectures (e.g. fin field-effect transistors). Meanwhile, memory devices have also transitted from NAND floating gates to 3D multi-layer stacked NAND architectures. State-of-the-art optical scatterometry at the near-atomic scale faces severe challenges of insufficient sensitivity and terrible parameter correlation [290, 291].

In response to these challenges, future trends for optical scatterometry include the extension of illumination wavelengths to short or ultra-short ranges, such as EUV

and x-rays [236–243], and making full use of light polarization [253, 254] to improve measurement sensitivity. Also, since there is no single technique that can fully fulfill the measurement requirements (such as resolution, speed, precision) of a full set of structural parameters of a complex device, the combination or integration of multiple techniques, also known as hybrid or combined metrology, is an important trend that will extend the capability of current techniques [290, 291]. Hybrid metrology is especially useful in parameter decorrelation. In addition to the above trends, advanced data analytics techniques for optical scatterometry, such as machine learning and deep learning [292, 293], are also worthy of future exploration.

5. Optical CT and SR imaging

5.1. Optical coherence tomography (OCT)

Optical coherence tomography (OCT) is a kind of imaging technology that acquires 3D information about the internal structure of the sample to be measured [294]. It is employed in applications where contactless and non-destructive inspection of internal structures is required. One of the advantages of OCT, compared with other technologies such as ultrasonic tomography [295], photoacoustic microscopy [296, 297], and x-ray computed tomography [298, 299], is a micrometric resolution [300] that can be achieved by relatively inexpensive components such as light sources, detectors, and optical elements. Furthermore, the setup for OCT can be designed at a compact size. Nowadays, OCT is often employed in the fields of biology and pharmacy, especially in ophthalmology and cardiology.

Table 7 shows a brief history of OCT development. As can be seen from the table, OCT is a relatively new technology invented in the 1990s. Nowadays, several types of OCT, which are classified depending on their detection methods, are available. In this section, the working principle of each of the types is reviewed.

5.1.1. Time-domain OCT (TD-OCT). The first OCT to be developed was time-domain OCT (TD-OCT) [301, 302]. A basic time-domain OCT configuration is shown in figure 43. A typical setup for time-domain OCT is composed of a low-coherence light source, a beam splitter, a reference mirror, an objective lens, a 2D scanning stage (lateral stage), a 1D scanning stage (axial stage) and a point detector. The reference mirror is mounted on the axial stage so that the OPD between the two reflected light beams can be changed to generate intensity modulation in the interference signal that is detected by the point detector. The interference light intensity reaches its maximum value when the OPD is zero, since a low-coherence light source is employed in the setup. The refractive index distribution in the specimen along the axial direction can be measured by scanning the specimen in the axial direction while monitoring the light intensity with the point detector. To obtain a 3D image of the refractive index distribution of the specimen, it is necessary to scan the lateral stage in the *X* and *Y* directions.

Table 6. Overview of the inverse problem solving methods.

Method	Pros	Cons
Nonlinear regression	• Flexible • Can achieve a highly accurate solution when assigned an appropriate initial value	• Apt to fall into local minima • Time-consuming, especially for 2D periodic structures
Library search	• Well suited for inline applications • Can guarantee a global solution	• Need to construct a signature library prior to measurement • Need interpolation to achieve a more accurate solution

Table 7. A brief history of OCT development.

Year	Type	Reference
1990, 1991	Time-domain OCT	[301, 302]
1994	Spectral-domain OCT	[303]
1998	Full-field OCT	[304]
2003	Swept-source OCT	[305]
2006	Full-field swept-source OCT	[306]

The advantage of time-domain OCT is that the setup can be constructed using relatively inexpensive components.

5.1.2. Frequency-domain OCT (FD-OCT). Following the initial invention of time-domain OCT, spectral-domain OCT (SD-OCT) was developed. This differs from conventional time-domain OCT that uses a point detector; for SD-OCT, broadband interference is acquired using a spectrometer, therefore spectral-domain OCT is categorized as Fourier-domain OCT (FD-OCT) [303]. Spectral-domain OCT can obtain the OPD between two light beams by an inverse Fourier transform of the obtained spectrum. Since axial scanning of a reference mirror is not required, spectral-domain OCT can achieve a higher measurement throughput than conventional time-domain OCT.

Swept-source OCT (SS-OCT) is another kind of frequency-domain OCT with a frequency-tunable light source [305]. The spectrum of an interference signal can be detected by sweeping the wavelength of the light source. Typically, the light source employed in swept-source OCT is a semiconductor laser. Since the resolution is determined by the swept wavelength bandwidth due to the characteristic of the inverse Fourier transform, light sources with a swept bandwidth exceeding 100 nm have been employed in recent years [307–309]. A swept light source composed of a femtosecond laser and a dispersive fiber has demonstrated a higher scanning speed [310].

5.1.3. Full-field OCT. Full-field OCT (FF-OCT) realizes OCT without the *XY*-scanning [304]. A typical configuration of full-field OCT is shown in figure 44. A Linnik configuration is used, with a pair of objective lenses inserted in both the reference and measurement arms, and the point detector in the conventional setup shown in figure 43 is replaced with

Figure 43. A schematic of time-domain OCT.
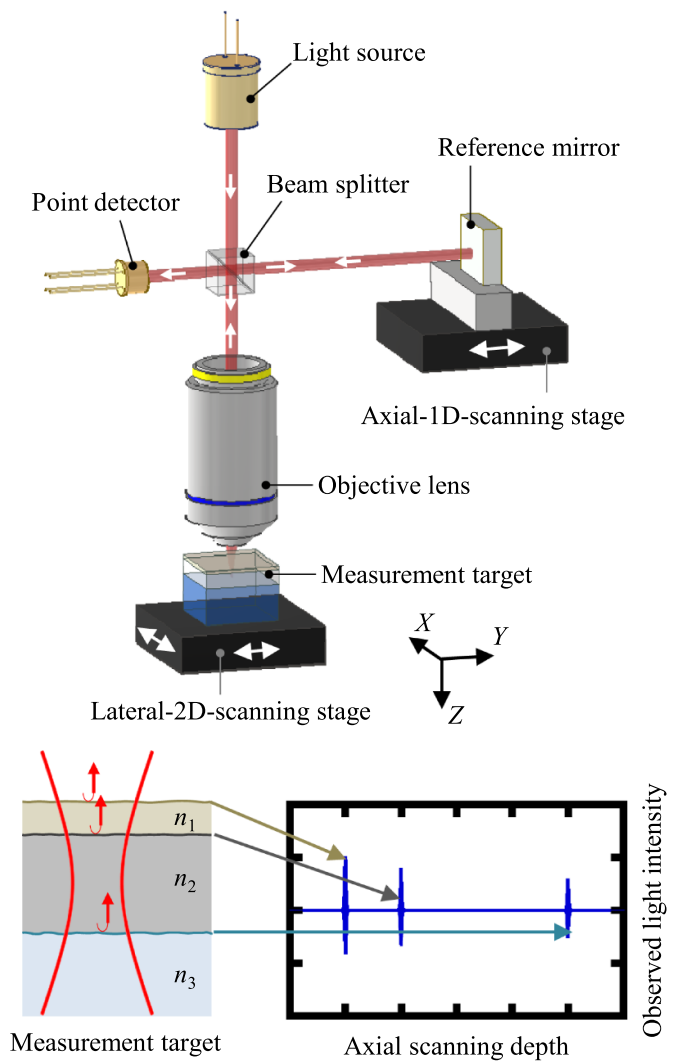
an imaging lens and a 2D detector. Since scanless imaging is possible, high-speed measurement can be realized. This technique can be applied to time-domain OCT and swept-source OCT; however, it cannot be applied to spectral-domain OCT that requires a 1D image as spectral information. OCT without mechanical scanning has been achieved by applying this configuration to swept-source OCT [306].
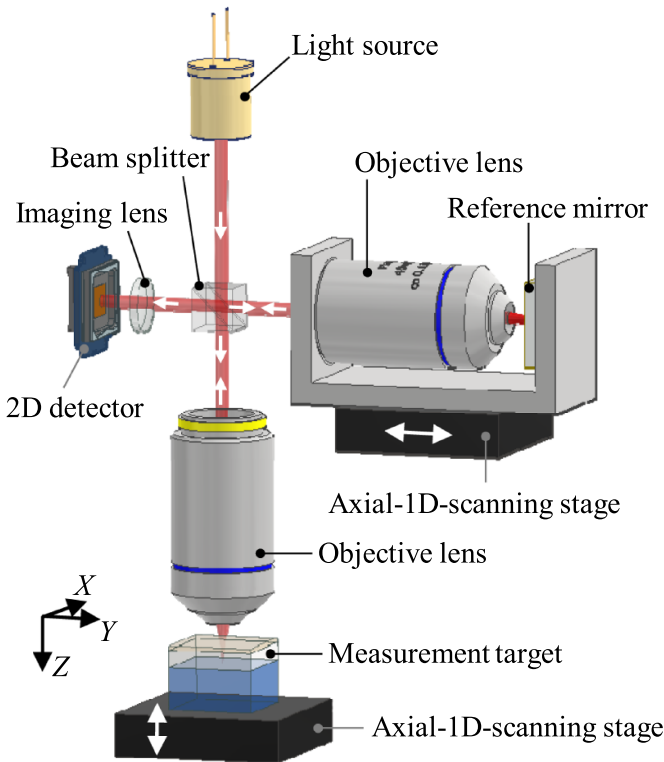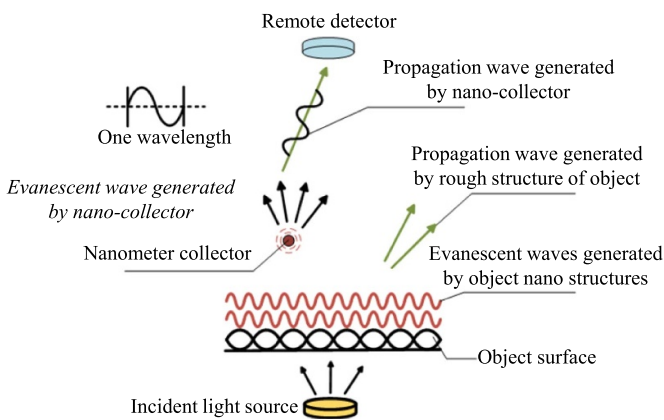
Figure 44. A schematic of full-field-OCT.

Figure 45. Schematic diagram of the near-field optical system [333].

Figure 46. Typical modes of a near-field super-resolution system: (a) transmission collection mode; (b) vertical reflection collection/illumination mode; (c) internal reflection collection mode.
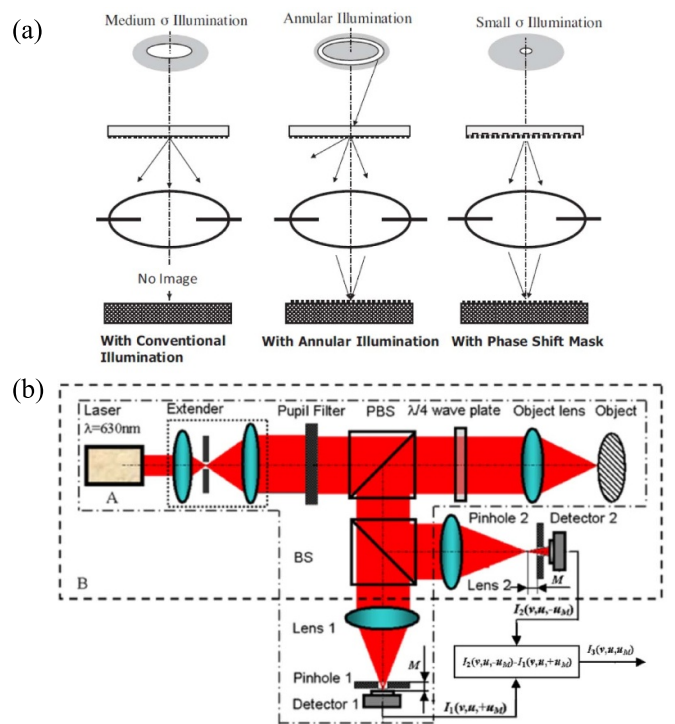
Figure 47. Pupil-filtering for super-resolution imaging: (a) annular illumination [347]; (b) an example of a confocal setup with a pupil filter [349]. (a) copyright (2015), with permission from Elsevier; (b) CC BY 4.0.

5.1.4. Industrial applications of OCT. Although OCT was developed for biological imaging, several proposals and examples of industrial applications have been reported so far. The following is an overview of the relevant papers.

Non-destructive inspection technology is useful for post-process QC in production manufacturing. One of the most common examples is the defect inspection of laminated structures such as color filters and polarizers in the liquid crystal display (LCD) industry [311], where defects in a product can be stochastically generated during the manufacturing process. Kim *et al* proposed an inspection method using spectral-domain OCT, and demonstrated its effectiveness for the fast evaluation of a large LCD [311]. Inspection of defects in

fiber-reinforced plastics (FRP) is another example where non-destructive inspection is required. Carbon-fiber-reinforced plastics (CFRP) are a kind of FRP that is widely employed in industrial products such as aircraft, automobiles and ships due to their low weight and high strength. However, wrinkle defects caused by high shear deformation can reduce the compressive strength of CFRP [312]. Several trials have therefore been made to apply spectral-domain OCT to the defect inspection of FRPs [313, 314].

The compact setup of optical-coherence tomography enables it to be applied for on-machine measurement. Holder *et al* demonstrated the on-machine measurement of fiber orientation in laser-ablated CFRP [315]. OCT can also be applied

Table 8. Overview of OCT techniques.

Time-domain OCT	• Obtains depth information from axial scanning • Intuitive interpretation of changes in the index • Relatively inexpensive • A typical axial resolution is several mm • Measurement speed at each point is low, due to axial scanning (typically kHz) * Lateral scanning is required
Spectral-domain OCT	• Obtains depth information from a Fourier transform of the spectra obtained by a spectrometer • Axial scanning is not required • A typical axial resolution is several mm • Measurement speed at each point is low due to the frame rate of the sensor in the spectrometer (typically kHz or lower) • Measurement apparatus is relatively large * Lateral scanning is required
Swept-source OCT	• Obtains depth information from a Fourier transform of the spectra obtained by a swept source • Extremely high-speed measurement (typically MHz) • Axial scanning is not required • A typical axial resolution is 10 mm • Lateral scanning is required
Full-field OCT	• Obtains depth information and 2D images from 2D detectors (Measurement speed of several tens of Hz) • OCT with no mechanical scanning is available in combination with swept sources • Axial resolution depends on the combined OCT type • Relatively expensive
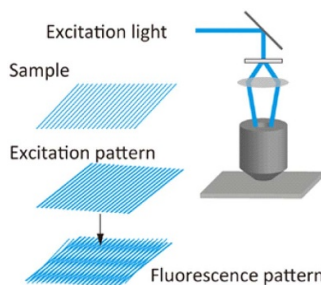
Figure 48. Principle of SIM. Reproduced from [356]. CC BY 4.0.

to the inspection of products fabricated by additive manufacturing, which is a new technology attracting attention in many industrial fields. In recent years, additive manufacturing has been widely applied to various materials such as resin [316] and metals [317]. In additive manufacturing, the stack height at each point can deviate due to nonuniformity in laser irradiation conditions during the process. DePond *et al* demonstrated on-machine precision measurement based onspectral-domain OCT during laser powder-bed-fusion additive manufacturing [317]. Closed-loop feedback forf the laser melting process has also been realized.

Optical coherence tomography can also be applied to the inspection of components made of various materials. In recent years, fine ceramic parts have become increasingly important incutting-edge industrial fields such as micromachining and semiconductor manufacturing, due to their high resistance to heat and chemical substances. Meanwhile, the strength and the product life of these components are strongly affected by the existence of internal defects. Considerable effort has thus been made to develop non-destructive inspection techniques for defect inspection of such ceramic components. For example, Reintjes *et al* investigated the subsurface defects of lead zirconate titanate (PZT) using time-domain OCT [318–320]. However, the strong scattering characteristics of ceramic materials make it difficult to carry out defect inspection based on OCT in the visible and near-infrared wavelength regions. Currently, most of the non-destructive inspection techniques for ceramic components are therefore based on ultrasonic inspection [321]; this inspection requires a measuring probe to come into contact with an object to be measured, while the signals obtained by these methods are noisy and have a relatively low resolution. The application of a mid-infrared laser, whose development has been accelerated in recent years [322–324], is expected to address the aforementioned issues in the defect inspection of ceramic components, and to realize the inspection of deeper internal structures. Su *et al* and Israelsen *et al* have applied the mid-infrared OCT to the defect inspection of components made of alumina and zirconia, materials that have a strong scattering effect in the short-wavelength regions [325, 326]. These results have revealed a clear difference between the mid-infrared OCT and the conventional OCT with a shorter-wavelength light source. A mid-infrared
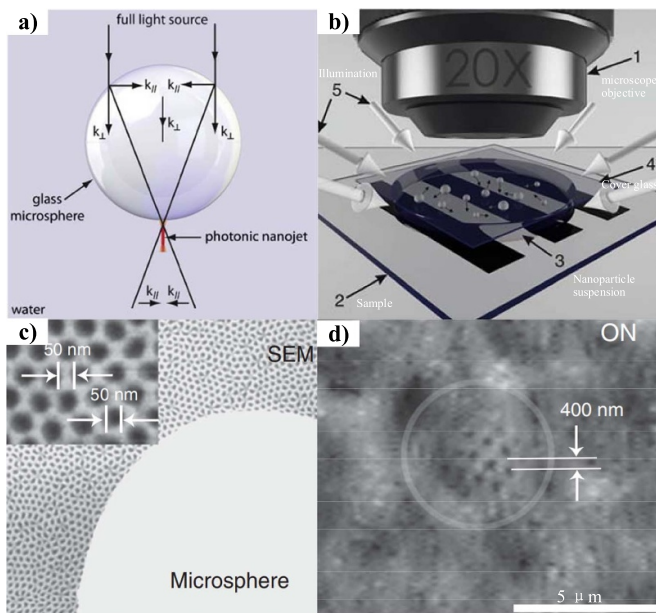
Figure 49. (a) Concept of the PNJ generation. (b) Schematic of the NORM nanoscope. (c) A gold-coated fishnet sample in SEM. (d) Fishnet imaging with a microsphere SR microscope with a magnification factor of eight. Reprinted from [329], copyright (2019), with permission from Elsevier.

laser is expected to be a powerful tool for the non-destructive inspection of products such as power semiconductors and MEMS, which are gaining importance in the industry. In table 8, the characteristics of each of the OCT techniques are summarized.

5.2. Super-resolution (SR) imaging

In a microscope, a lens system generates a magnified image of an object. Under ideal conditions, without the influence of aberrations such as spherical aberration and chromatic aberration, light rays emanating from a point on an object under measurement are focused on a point of a finite size in the image plane of the lens system due to the influence of the light diffraction limit. The light intensity distribution of the image of a point in the image plane is referred to as the PSF. The lateral resolution of a microscope can be determined by using the full width at half-maximum (FWHM) of the PSF. If the light wavelength and NA of a lens system are denoted by λ and NA, respectively, the FWHM of a lens system can be expressed as approximately $0.61\lambda/\text{NA}$. Regarding the light intensity distribution of the image of a point, two neighbouring points at a distance smaller than the FWHM cannot be resolved. As can be seen in the definition of an FWHM, a larger NA contributes to the obtainment of a higher lateral resolution. With the employment of an oil-immersion lens with an NA of 1.40, a resolution of approximately 200 nm can be achieved in the visible light range. Meanwhile, a strong demand exists for an even higher lateral resolution in several applications such as

the inspection of micro- or nanostructures in precision engineering and/or the imaging of cell structures in biotechnology. For the achievement of a resolution beyond the diffraction limit, To date, much effort has been committed to developing techniques for SR imaging to achieve resolution beyond the diffraction limit. As mentioned above, these techniques can be classified into manufacture oriented and biologically oriented [327–329] SR techniques, most of which are aimed at lateral resolution enhancement. Taking the main topic of this article into consideration, manufacture-oriented SR techniques are reviewed in this section.

The axial size of the PSF, which is approximately 500 nm in a refractive index-matched medium, is approximately 2–3 times larger than its lateral width for ordinary high NA objectives. As a typical method, confocal techniques with the so-called sectioning effect have long been used to improve the axial resolution. In recent years, a high axial resolution of approximately 1 nm has been achieved using multiple differential confocal technologies [330–332]. Confocal microscopy can be integrated with the lateral SR techniques that are reviewed below.

5.2.1. Near-field SR diffraction.
Near-field microscopy was designed to capture the light propagating from excited fluorophores at a short distance or to detect evanescent light near fluorophores to achieve a high resolution, since the information from high-frequency components can be lost during the propagation of light diffracted from a small object. A schematic of the principle of near-field optical sensing is shown in figure 45 [333]. When an incident light excites a sample under inspection, high spatial-frequency surface features smaller than the wavelength of incident light generate evanescent waves that can exist within a range of less than one wavelength. The generated evanescent wave cannot propagate to the far field, but can become a radiated wave when a small-sized probe is placed into the evanescent field by means of a scattering, refraction or transmission effect, and can be detected in the far field [334, 335].

Near-field scanning optical microscopy (NSOM) has been developed based on the principle of the non-radiating field-sensing method. A fiber-based optical probe is often employed in NSOM due to its ease of use, as well as a high lateral resolution of several tens of nm. Three typical setups for NSOM are shown in figure 46. As can be seen in the figure, a sample image can be obtained by scanning the tip of a fiber probe over the sample's surface while illuminating the region under inspection [336–339]. With respect to the ordinary transmission mode and the reflection mode, this third mode is known as the photon scanning tunnelling microscope (PSTM) [340]. A fiber probe scans over the sample to collect evanescent waves modulated by the total internal reflection surface. Its spatial resolution is mainly affected by the decay length of the evanescent field, as well as the shape and size of the probe's tip. Due to the nature of the evanescent field, whose intensity decays exponentially, a sub-wavelength resolution

Table 9. Major technologies for manufacturing-oriented super-resolution imaging.

Near-field super-resolution	• Evanescent wave of high-frequency spatial information smaller than the incident wave on the surface is detected. • Near-field evanescent wave is bridged to far field for detection by inducing a small probe into the near-field area. • Tens of nanometre resolution can be achieved. • Near-field region evanescent wave dependence limits its use to near-surface features only
Pupil-filtering confocal super-resolution	• Pupil filter for beam shaping enables a main-lobe diameter smaller than the diffraction limit for a lateral super-resolution. • Confocal approach compensates for the reduced axial resolution by using an optical-sectioning technique with a pinhole. • A lateral resolution better than one-third of the incident wavelength can be achieved. It is difficult to improve it further.
Spatially patterned super-resolution	• Pattern with sub-diffraction-limit features is excited to surface for beating with comparable small-scale information. • Multiple lowered beating frequency images involving the small-scale information are then reconstructed for a super-resolution image. • A resolution better than 100 nm can be achieved; the frequency spectrum of the excitation pattern affects the super-resolution ability. • A saturated structured illumination pattern with more frequencies can further improve the resolution, but the saturation may damage some samples.
Micro-object-based super-resolution	• Photonic nanojets (PNJs) with a width of around $0.5 \pm 0.2\lambda$ are generated by some micro-objects. • PNJs enhance visible light backscattering so that smaller features can be observed in a far field by an ordinary microscope. • A resolution of between $\lambda/8$ and $\lambda/14$ at the far field has been achieved. • Observed results from the microscope need to be further calculated using the calibrated magnitude of the specific micro-object.

in three dimensions can be achieved. A prototype instrument has achieved lateral and axial resolutions of 200 nm and 80 nm, respectively, under conditions with a light wavelength of 633 nm and a probe tip radius of 1 μm. A further study has demonstrated a lateral resolution of 10 nm with an enhancement to the effective sharpness of the tip [341].

A further improvement of the spatial resolution, down to an atomic level, can be realized by the notable probe techniques such as the hole-less tetrahedral tip probe, a local magnetic field interferometric aperture-less scanning probe, and so on [342, 343]. However, due to the rapid decrease in light intensity with the miniaturization of the fiber probe, the lateral resolution was limited to several tens of nm. For the evaluation of fine semiconductor patterns with a half pitch of 20 nm, a sharp metal probe has been proposed to enhance the optical performance, and a residual layer thickness of 10 nm of nanoimprint lithography has been achieved [344].

With the rapid development of key technologies in NSOM, such as probe–sample distance control and the above-mentioned sensing techniques, a commercial NSOM can provide a competent performance with some state-of-the-art prototypes; for example, a commercial scattering-type NSOM can provide a spatial resolution of 10 nm [345]. Meanwhile, although NSOM has demonstrated its ability in SR imaging, a short near-field region on the order of tens of nanometres

limits the applications of near-field microscopy. Far-field high-resolution imaging techniques are thus required in applications where near-field microscopy cannot be applied.

5.2.2. Pupil-filtering confocal SR imaging. Aiming to improve the lateral resolution of optical imaging, in 1952, di Francia introduced a method of employing a pupil filter in an optical imaging system [346]. With the help of an annular illumination [347] with a pupil filter, as shown in figure 47(a), the diameter of a main lobe can be reduced beyond the diffraction limit [348]. Since pupil-filter techniques enable the imaging system to modify the relationship between the amplitude and the phase in both the zeroth- and first-order diffracted beams, the lateral resolution of an imaging system can be improved by optimizing the design parameters of a pupil filter. It should be noted that a small main lobe can reduce the light intensity, resulting in the degradation of image quality. This issue can be addressed by employing a pinhole in the imaging system, as shown in figure 47(b) [348, 349]; the influences of the side-lobes generated by the pupil filter can be reduced with the enhancement due to the optical sectioning effect in a conventional confocal setup [350–352]. A high lateral resolution of better than 0.2 μm was achieved under the conditions of $\lambda = 632.8$ nm and NA $= 0.85$ by an imaging system with a

bipolar absolute-differential confocal setup having a shaped annular illumination [349].

Also, a small focused spot having a long depth of focus was generated with a radially polarized light whose polarization modulation was controlled by a phase plate having three concentric regions [353]. With the enhancement of the tight focusing characteristics of a radially polarized illumination with a high NA objective as well as the pupil filtering technique in a confocal setup, SR imaging with a lateral resolution beyond the diffraction limit has been realized [348].

5.2.3. Spatially patterned SR. To obtain a resolution beyond the diffraction limit, some approaches employing spatially patterned illumination or patterned excitation have been developed. These approaches include so-called structured illumination microscopy (SIM), saturated SIM, as well as stimulated emission depletion (STED). In the following, the structured illumination microscope often employed in manufacturing applications is reviewed [354, 355].

Figure 48 shows a schematic of the structured illumination microscope, where a patterned standing wave structure is projected onto an object as the illumination field [356]. The spatial frequency of the illumination pattern enables the high-spatial-frequency components of the object to be shifted to a lower-frequency region. An image of the object under inspection can be reconstructed at a high resolution by obtaining several images with illumination fields that have different spatial frequencies and different pattern structures. A patterned illumination field can be obtained from the interference between several incident beams. With the use of such periodic patterned illumination with a sinusoidal intensity modulation, a moire image with a much lower spatial frequency than that of the structure of the object under inspection can be captured by the microscope. By obtaining several more images while scanning the periodic pattern illumination and rotating the target object, the sample structure can be reconstructed through numerical calculations. Under a patterned illumination with a high spatial frequency, a lateral resolution of better than 100 nm can be achieved with an infrared laser source [357].

5.2.4. Micro-object-based SR imaging. A new type of SR microscopy, developed in 2004 [358] that uses a photonic nanojet (PNJ), shown in figure 49(a) [329], is attracting attention. When a plane wave is projected onto a micro-object, a PNJ is generated behind the object. The modulation of the generated PNJ can be detected by an ordinary optical microscope, as shown in figure 49(b) [329]. In general, the length of a PNJ is approximately 2λ at FWHM, while its width is about $0.5 \pm 0.2\lambda$ at FWHM, depending on the parameters of the micro-object and its surroundings. Visible-light backscattering can be enhanced by up to orders of magnitude by nanometre-scale dielectric particles within the PNJ. Furthermore, to obtain a physics-based insight into PNJ and its SR performance, more theoretical approaches to

PNJ enhancement have been carried out, based on geometric optics and Mie theory, as well as angular spectrum and analysis [359].

As well as the theoretical studies, experimental investigations have also been carried out to verify the feasibility of micro-object-based SR microscopy. An early study has been conducted to show its feasibility in both transmission and reflection modes with a far-field resolution between $\lambda/8$ and $\lambda/14$ as shown in figures 49(c) and (d) [329, 360, 361]. Using a micro-sphere with a diameter of 3 μm, Ferrand verified the size of a PNJ to be 270 nm at FWHM at a wavelength of 520 nm [362]. Ju employed a self-assembled micro-sphere to generate remarkably short near-field focal lengths [363]. From these results, micro-sphere-based SR microscopy is expected to be a viable alternative microscopy technique for bioimaging, near-field lithography, optical nanosensing, and so on.

In table 9, the characteristics of each of the SR techniques treated in this section are summarized.

6. Conclusions

In this paper, an insight into optical metrology in manufacturing has been provided. Today, highly sensitive optical sensors with a sub-nanometer resolution are employed in manufacturing processes for precision positioning, as well as in post processing for form measurement of a fabricated product for QC. Some state-of-the-art setups for multi-axis measurement with multiple optical sensors and also a planar/surface encoder that has planar scale gratings, have been presented. Advances have also been made in optical form interferometry and deflectometry, and until now, many applications have been developed to evaluate precision optical components with a nanometer resolution in the vertical direction. With advanced techniques such as sub-aperture stitching interferometry, the form measurement of a large object such as the primary mirror of a telescope at a scale of up to several meters has recently been achieved. The technological innovation in optical form interferometry and deflectometry is expected to continue due to the strong demands for the fast and contactless measurement of large components in many industrial fields. Furthermore, there is currently strong demand for measurement of not only the surface form of an object but also micro- and nanostructures and thin-film structures on an object's surface. Optical microscopy and scatterometry are thus gaining importance in today's manufacturing industry where the miniaturization of components is being accelerated. Also, state-of-the-art methods for measuring the internal structure of fabricated products in a non-destructive manner are attracting attention, as well as SR imaging techniques that can realize a high spatial resolution beyond the diffraction limit.

In the manufacturing industry, where further improvements in accuracy and efficiency are constantly required, the import-

ance of multi-axis measurement is expected to increase [1, 2]. As the recent increase in market share shows, sensor technology based on a scale grating that has environmental robustness, as introduced in section 2, is also expected to continue to increase in importance. Although the establishment of a method that can guarantee scale accuracy is an important issue that needs to be addressed, a method based on scatterometry and/or a method based on the highly sensitive optical angle sensor could be a solution [364]. Besides, for the achievement of even higher machining accuracy, continuous effort will be made in the development of on-machine/in-process optical-measurement technologies. Furthermore, with the technological improvement of big data processing technology and computer technology, it is expected that the measurement of fine structures over a wider range may become more familiar when enhanced by the stitching method introduced in section 3.

In recent years, the importance of the traceability of measurement is increasing in many industrial fields. With the development of an optical frequency comb, which is directly traceable to the international standard of time/frequency, many types of technologies have been developed for the measurement of length, angle, and other physical quantities with an optical frequency comb laser. This trend is expected to continue and will be accelerated by the development of a compact mode-locked femtosecond laser source at a reasonable cost in the near future, when the traceability of measurement is expected to be more important.

Appendix A

Year	Patent Number	Title	Inventor/Author
1952	US2612074(A)	Mirau interferometer	Mirau A H
1990	US4948253(A)	Interferometric surface profiler for spherical surfaces	Biegen J F
1991	US5073018(A)	Correlation microscope	Kino G S *et al*
1992	US5166751(A)	Interferometric profilometer sensor	Massig J H
1993	US5194918(A)	Method of providing images of surfaces with a correlation microscope by transforming interference signals	Kino G S Chim S S C
1994	US5633715(A)	Centroid approach for estimating modulation peak in broadbandwidth interferometry	Ai C and Novak E L
1995	US5471303(A)	Combination of white-light scanning and phase-shifting interferometry for surface profile measurements	Ai C and Caber P J
1995	US5446547(A)	Combination of motorized and piezoelectric translation for long-range vertical scanning interferometry	Guenther B W, Caber P J and Hayes J B
1998	US5726754(A)	Variable-speed scanning for interferometric measurements	Andrews M P and Unruh P R
2001	US6987570(B1)	Reference signal for stitching of interferometric profiles	Schmit J and Olszak A
2001	US6185315(B1)	Method of combining multiple sets of overlapping surface-profile interferometric data to produce a continuous composite map	Schmucker M A and Becker B W
2002	US6493093(B2)	Bat-Wing Attenuation in White Light Interferometry	Harasaki A and Schmit J
2002	WO02082008(A1)	A Method and Apparatus of Two Wavelength Interferometry for Measuring Accurate Height of Small Step Composed of Two Different Materials	Kim S W and Park M C
2003	US6545763(B1)	Method for measuring a thickness profile and a refractive index using white-light scanning interferometry and recording medium therefor	Kim S W and Kim G H
2003	US6 538 809(B1)	Variable epi-illumination interference attachment	Stankewitz H W
2003	US6552806(B1)	Automated minimization of optical path difference and reference mirror focus in white-light interference microscope objective	Swinford R W *et al*
2006	US7054071(B2)	Mirau interference objective lens	Davidson M P
2007	WO2007060441(A1)	Apparatus for and a method of determining surface characteristics	Mansfield D I
2008	US7428685(B2)	Cyclic error compensation in interferometry systems	Demarest F C and Hill H A
2009	US7605925(B1)	High-definition vertical-scan interferometry	D Chen
2009	EP2108919(A2)	Interferometer for determining characteristics of an object surface	de Groot P J and de Lega X C
2009	US7619746(B2)	Generating model signals for Interferometry	de Lega X C
2009	US7595891(B2)	Measurement of the top surface of an object with/without transparent thin films in white light interferometry	Tang S
2009	US7538887(B1)	Temporal interferometric signal modelling with constant phase shift in white light interferometry	Tang S
2010	US7948636(B2)	Interferometer and method for measuring characteristics of optically unresolved surface features	de Groot P J *et al*
2010	US7649634(B2)	Methods and systems for white light interferometry and characterization of films	Wan D S
2011	US7956630(B1)	Real-time effective-wavelength error correction for HDVSI	Chen D
2011	US7898672(B1)	Real-time scanner-nonlinearity error correction for HDVSI	Chen D
2011	US7978338(B2)	Compound reference interferometer	de Groot P J *et al*
2011	US7952724(B2)	Interferometer with multiple modes of operation for determining characteristics of an object surface	de Lega X C and de Groot P J
2011	US8072610(B1)	Polarization Mirau interference microscope	Schmit J and Hariharan P
2012	US8126677(B2)	Analyzing surface structure using scanning interferometry	de Groot P J and de Lega X C
2012	US8107085(B2)	Methods and systems for interferometric analysis of surfaces and related applications	de Groot P J
2016	US20160061592A1	Systems and methods for using white light interferometry to measure undercut of a bi-layer structure	Beye R W and Poh S T

(Continued)

(Continued).

Year	Patent Number	Title	Inventor/Author
2016	CN105806789A	Optical fiber white light interferometry difference spectrometer	Yuan *et al*
2016	US10288408B2	A scanning white-light interferometry system for characterization of patterned semiconductor features	Smith N P and Antonelli G A
2019	US10598604B1	Normal incidence phase-shifted deflectometry sensor, system, and method for inspecting a surface of a specimen	Schiltz D and Roisen N
2020	TW202012871A	Image capturing system and image capturing method	Chang W C and Lin C H

ORCID iDs

Liang-Chia Chen ⓘ https://orcid.org/0000-0001-9613-9936
Dae Wook Kim ⓘ https://orcid.org/0000-0002-1122-8727
Xiuguo Chen ⓘ https://orcid.org/0000-0002-7067-5084
Hiraku Matsukuma ⓘ https://orcid.org/0000-0001-8125-9708

References

[1] Gao W, Kim S W, Bosse H, Haitjema H, Chen Y L, Lu X D, Knapp W, Weckenmann A, Estler W T and Kunzmann H 2015 Measurement technologies for precision positioning *CIRP Ann. Manuf. Technol.* **64** 773–96

[2] Gao W, Haitjema H, Fang F Z, Leach R K, Cheung C F, Savio E and Linares J M 2019 On-machine and in-process surface metrology for precision manufacturing *CIRP Ann.* **68** 843–66

[3] Schwenke H, Neuschaefer-Rube U, Pfeifer T, Kunzmann H, Flugge J, Wendt K, Danzebrink H and Abou-zeid A 2002 Optical methods for dimensional metrology in production engineering *CIRP Ann. Manuf. Technol.* **51** 685–99

[4] Estler W T, Edmundson K L, Peggs G N and Parker D H 2002 Large-scale metrology – an update *CIRP Ann.* **51** 587–609

[5] Kunzmann H, Pfeifer T and Flügge J 1993 Scales vs. laser interferometers performance and comparison of two measuring systems *CIRP Ann. Manuf. Technol.* **42** 753–67

[6] Manske E, Jäger G, Hausotte T, Fül R and Füßl R 2012 Recent developments and challenges of nanopositioning and nanomeasuring technology *Meas. Sci. Technol.* **23** 10

[7] Chen X and Liu S 2019 Optical scatterometry for nanostructure metrology *Metrology* **2019** 477–513

[8] Leach R K, Bourell D, Carmignato S, Donmez A, Senin N and Dewulf W 2019 Geometrical metrology for metal additive manufacturing *CIRP Ann.* **68** 677–700

[9] Udem T, Holzwarth R and Hänsch T W 2002 Optical frequency metrology *Nature* **416** 233–7

[10] Kubina P, Adel P, Adler F, Grosche G, Hänsch T W, Holzwarth R, Leitenstorfer A, Lipphardt B and Schnatz H 2005 Long term comparison of two fiber based frequency comb systems *Opt. Express* **13** 904–9

[11] Jin J 2015 Dimensional metrology using the optical comb of a mode-locked laser *Meas. Sci. Technol.* **27** 022001

[12] Häusler G and Ettl S 2011 Limitations of optical 3D sensors *Optical Measurement of Surface Topography* (Berlin, Heidelberg: Springer) pp 23–48

[13] Leach R (ed) 2011 *Optical Measurement of Surface Topography* (Berlin, Heidelberg: Springer)

[14] Zheng Y, Zhang X, Wang S, Li Q, Qin H and Li B 2020 Similarity evaluation of topography measurement results by different optical metrology technologies for additive manufactured parts *Opt. Lasers Eng.* **126** 105920

[15] Savio E, De Chiffre L and Schmitt R 2007 Metrology of freeform shaped parts *CIRP Ann. Manuf. Technol.* **56** 810–35

[16] Pathak V K, Singh A K, Sivadasan M and Singh N K 2018 Framework for automated GD&T inspection using 3D scanner *J. Inst. Eng. Ser.* C **99** 197–205

[17] Fang F Z, Zhang X D, Weckenmann A, Zhang G X and Evans C 2013 Manufacturing and measurement of freeform optics *CIRP Ann. Manuf. Technol.* **62** 823–46

[18] Kim D W, Su T, Su P, Oh C, Graves L and Burge J 2015 Accurate and rapid IR metrology for the manufacture of freeform optics *SPIE Newsroom* (http://www.spie.org/x114738.xml)

[19] De Groot P J 2019 A review of selected topics in interferometric optical metrology *Rep. Prog. Phys.* **82** 32

[20] Trumper I, Choi H and Kim D W 2016 Instantaneous phase shifting deflectometry *Opt. Express* **24** 27993

[21] Geckeler R D 2007 Optimal use of pentaprisms in highly accurate deflectometric scanning *Meas. Sci. Technol.* **18** 115–25

[22] Yang S and Zhang G 2018 A review of interferometry for geometric measurement *Meas. Sci. Technol.* **29** 102001

[23] Hussain D, Ahmad K, Song J and Xie H 2017 Advances in the atomic force microscopy for critical dimension metrology *Meas. Sci. Technol.* **28** 012001

[24] Yacoot A and Koenders L 2011 Recent developments in dimensional nanometrology using AFMs *Meas. Sci. Technol.* **22** 122001

[25] Dai G, Pohlenz F, Xu M, Koenders L, Danzebrink H U and Wilkening G 2006 Accurate and traceable measurement of nano- and micro-structures *Meas. Sci. Technol.* **17** 545–52

[26] Huang B, Wang W, Bates M and Zhuang X 2008 Three-dimensional super-resolution imaging by stochastic optical reconstruction microscopy *Science* **319** 810–3

[27] Raymond C J 2001 Scatterometry for semiconductor metrology *Handbook of Silicon Semiconductor Metrology* pp 477–514 (New York, Basel: Marcel Dekker, Inc)

[28] Pathak V K and Singh A K 2017 Optimization of morphological process parameters in contactless laser scanning system using modified particle swarm algorithm *Meas. J. Int. Meas. Confederation* **109** 27–35

[29] Ruiji T 2001 *Ultra-Precision Coordinate Measuring Machine—Design, Calibration and Error Compensation* (The Netherlands: Technische Universiteit Delft, Eindhoven)

[30] Li X, Gao W, Muto H, Shimizu Y, Ito S and Dian S 2013 A six-degree-of-freedom surface encoder for precision positioning of a planar motion stage *Precis. Eng.* **37** 771–81

[31] Shimizu Y, Matsukuma H and Gao W 2019 Optical sensors for multi-axis angle and displacement measurement using grating reflectors *Sensors* **19** 5289

[32] Steiner R L, Williams E R, Newell D B and Liu R 2005 Towards an electronic kilogram: an improved measurement of the Planck constant and electron mass *Metrologia* **42** 431–41

[33] Dukes J N and Gordon G B 1970 A two-hundred-foot yardstick with graduations every microinch *Hewlett Packard J.* **21** 2–8

[34] Teimel A 1992 Technology and applications of grating interferometers in high-precision measurement *Precis. Eng.* **14** 147–54

[35] Magnescale C 2018 Feedback Scale General Catalog

[36] Pollinger F, Meyer T, Beyer J, Doloca N R, Schellin W, Niemeier W, Jokela J, Häkli P, Abou-Zeid A and Meiners-Hagen K 2012 The upgraded PTB 600 m baseline: a high-accuracy reference for the calibration and the development of long distance measurement devices *Meas. Sci. Technol.* **23** 11

[37] Beers J S and Penzes W B 1992 NIST length scale interferometer measurement assurance *Nistir* pp 1–30 (https://www.nist.gov/system/files/documents/calibrations/4998.pdf)

[38] Tiemann I *et al* 2008 An international length comparison using vacuum comparators and a photoelectric incremental encoder as transfer standard *Precis. Eng.* **32** 1–6

[39] Weichert C, Köchert P, Köning R, Flügge J, Andreas B, Kuetgens U and Yacoot A 2012 A heterodyne interferometer with periodic nonlinearities smaller than ±10pm *Meas. Sci. Technol.* **23** 7

[40] Meiners-Hagen K, Meyer T, Mildner J and Pollinger F 2017 SI-traceable absolute distance measurement over more than 800 meters with sub-nanometer interferometry by two-color inline refractivity compensation *Appl. Phys. Lett.* **111** 5

[41] Hecht E 2017 *Optics* 5th edn (Essex: Pearson)

[42] Pisani M 2009 A homodyne Michelson interferometer with sub-picometer resolution *Meas. Sci. Technol.* **20** 6

[43] Lawall J and Kessler E 2000 Michelson interferometry with 10 pm accuracy *Rev. Sci. Instrum.* **71** 2669–76

[44] Schmidt R H M 2012 Ultra-precision engineering in lithographic exposure equipment for the semiconductor industry *Philos. Trans. R. Soc.* A **370** 3950–72

[45] Lay O P, Dubovitsky S, Peters R D, Burger J, Steier W H, Ahn S-W and Fetterman H R 2004 MSTAR: an absolute metrology system with submicrometer accuracy *New Frontiers Stellar Interferom* **5491** 1068

[46] Mildner J, Meiners-Hagen K and Pollinger F 2016 Dual-frequency comb generation with differing GHz repetition rates by parallel Fabry-Perot cavity filtering of a single broadband frequency comb source *Meas. Sci. Technol.* **27** 8

[47] Yang R, Pollinger F, Meiners-Hagen K, Krystek M, Tan J and Bosse H 2015 Absolute distance measurement by dual-comb interferometry with multi-channel digital lock-in phase detection *Meas. Sci. Technol.* **26** 10

[48] Meiners-Hagen K, Meyer T, Prellinger G, Pöschel W, Dontsov D and Pollinger F 2016 Overcoming the refractivity limit in manufacturing environment *Opt. Express* **24** 24092

[49] Coveney T 2020 A review of state-of-the-art 1D length scale calibration instruments *Meas. Sci. Technol.* **31** 042002

[50] Renishaw plc 2013 RESOLUTE absolute optical encoder with Biss serial communications pp 1–8

[51] Wang H, Wang J, Chen B, Xiao P, Chen X, Cai N and Ling B W K 2015 Absolute optical imaging position encoder *Meas. J. Int. Meas. Confederation* **67** 42–50

[52] Heidenhain 2016 Exposed_linear_encoders *Heidenhain*

[53] Matsuzoe Y 2003 High-performance absolute rotary encoder using multitrack and M-code *Opt. Eng.* **42** 124–31

[54] Ishimura S and Kikuchi K 2015 Eight-state trellis-coded optical modulation with signal constellations of four-dimensional M-ary quadrature-amplitude modulation *Opt. Express* **23** 13

[55] Jäger G, Manske E, Hausotte T, Müller A and Balzer F 2016 Nanopositioning and nanomeasuring machine NPMM-200—a new powerful tool for large-range micro- and nanotechnology *Surf. Topogr. Metrol. Prop.* **4** 034004

[56] Schellekens P, Rosielle N, Vermeulen H, Vermeulen M, Wetzels S and Pril W 1998 Design for precision: current status and trends *CIRP Ann. Manuf. Technol.* **47** 557–86

[57] Bryan J B 1979 The Abbé principle revisited: an updated interpretation *Precis. Eng.* **1** 129–32

[58] Kimura A, Gao W, Kim W, Hosono K, Shimizu Y, Shi L and Zeng L 2012 A sub-nanometric three-axis surface encoder with short-period planar gratings for stage motion measurement *Precis. Eng.* **36** 576–85

[59] Gao W, Dejima S, Shimizu Y and Kiyono S 2003 Precision measurement of two-axis positions and tilt motions using a surface encoder *CIRP Ann. Manuf. Technol.* **52** 435–8

[60] Gao W, Araki T, Kiyono S, Okazaki Y and Yamanaka M 2003 Precision nano-fabrication and evaluation of a large area sinusoidal grid surface for a surface encoder *Precis. Eng.* **27** 289–98

[61] Gao W and Kimura A 2007 A three-axis displacement sensor with nanometric resolution *CIRP Ann. Manuf. Technol.* **56** 529–32

[62] Kimura A, Gao W, Arai Y and Lijiang Z 2010 Design and construction of a two-degree-of-freedom linear encoder for nanometric measurement of stage position and straightness *Precis. Eng.* **34** 145–55

[63] Shimizu Y, Ishizuka R, Mano K, Kanda Y, Matsukuma H and Gao W 2021 An absolute surface encoder with a planar scale grating of variable periods *Precis. Eng.* **67** 36–47

[64] Shimizu Y, Ito T, Li X, Kim W and Gao W 2014 Design and testing of a four-probe optical sensor head for three-axis surface encoder with a mosaic scale grating *Meas. Sci. Technol.* **25** 15

[65] Li X, Gao W, Shimizu Y and Ito S 2014 A two-axis Lloyd's mirror interferometer for fabrication of two-dimensional diffraction gratings *CIRP Ann. Manuf. Technol.* **63** 461–4

[66] Shimizu Y, Aihara R, Mano K, Chen C, Chen Y-L, Chen X and Gao W 2018 Design and testing of a compact non-orthogonal two-axis Lloyd's mirror interferometer for fabrication of large-area two-dimensional scale gratings *Precis. Eng.* **52** 138–51

[67] Shimizu Y, Mano K, Murakami H, Hirota S, Matsukuma H and Gao W 2019 Design optimization of a non-orthogonal two-axis Lloyd's mirror interferometer for fabrication of large-area two-dimensional scale gratings *Precis. Eng.* **60** 280–90

[68] Matsukuma H, Matsunaga M, Zhang K, Shimizu Y and Gao W 2020 Fabrication of a two-dimensional diffraction grating with isolated photoresist pattern structures *Nanomanf. Metrol.* **14** 546–51

[69] Chen X, Ren Z, Shimizu Y, Chen Y and Gao W 2017 Optimal polarization modulation for orthogonal two-axis Lloyd's mirror interference lithography *Opt. Express* **25** 22237

[70] Shimizu Y, Aihara R, Ren Z, Chen Y-L, Ito S and Gao W 2016 Influences of misalignment errors of optical components in an orthogonal two-axis Lloyd's mirror interferometer *Opt. Express* **24** 18778–89

[71] Gao W, Sato S and Arai Y 2010 A linear-rotary stage for precision positioning *Precis. Eng.* **34** 301–6

[72] Keyence 2021 LK-G3000 Series High-speed, High-accuracy CCD Laser Displacement Sensor Catalog

[73] Gao W, Furukawa M, Kiyono S and Yamazaki H 2004 Cutting error measurement of flexspline gears of harmonic speed reducers using laser probes *Precis. Eng.* **28** 358–63

[74] Furukawa M, Gao W, Shimizu H, Kiyono S, Yasutake M and Takahashi K 2003 Slit width measurement of a long precision slot die *J. Japan Soc. Precis. Eng.* **69** 1013–7

[75] Ito S, Matsuura D, Meguro T, Goto S, Shimizu Y, Gao W, Adachi S and Omiya K 2014 On-machine form measurement of high precision ceramics parts by using a laser displacement sensor *J. Adv. Mech. Des. Syst. Manuf.* **8** JAMDSM0048–JAMDSM0048

[76] Wen B, Shimizu Y, Watanabe Y, Matsukuma H and Gao W 2020 On-machine profile measurement of a micro cutting edge by using a contact-type compact probe unit *Precis. Eng.* **65** 230–9

[77] Osawa S, Ito S, Shimizu Y, Jang S, Gao W, Fukuda T, Kato A and Kubota K 2012 Cutting edge height measurement of a rotary cutting tool by a laser displacement sensor *J. Adv. Mech. Des. Syst. Manuf.* **6** 815–28

[78] Jang Y-S and Kim S-W 2018 Distance measurements using mode-locked lasers: a review *Nanomanuf. Metrol.* **1** 131–47

[79] Hyun S, Kim Y-J, Kim Y, Jin J and Kim S-W 2009 Absolute length measurement with the frequency comb of a femtosecond laser *Meas. Sci. Technol.* **20** 095302

[80] Lee J, Han S, Lee K, Bae E, Kim S, Lee S, Kim S-W and Kim Y-J 2013 Absolute distance measurement by dual-comb interferometry with adjustable synthetic wavelength *Meas. Sci. Technol.* **24** 045201

[81] Lee J, Lee K, Lee S, Kim S-W and Kim Y-J 2012 High precision laser ranging by time-of-flight measurement of femtosecond pulses *Meas. Sci. Technol.* **23** 065203

[82] Inaba H *et al* 2006 Long-term measurement of optical frequencies using a simple, robust and low-noise fiber based frequency comb *Opt. Express* **14** 5223–31

[83] Sato R, Chen C, Matsukuma H, Shimizu Y and Gao W 2020 A new signal processing method for a differential chromatic confocal probe with a mode-locked femtosecond laser *Meas. Sci. Technol.* **31** 094004

[84] Chen X, Nakamura T, Shimizu Y, Chen C, Chen Y L, Matsukuma H and Gao W 2018 A chromatic confocal probe with a mode-locked femtosecond laser source *Opt. Laser Technol.* **103** 359–66

[85] Sato R, Shimizu Y, Chen C, Matsukuma H and Gao W 2019 Investigation and improvement of thermal stability of a chromatic confocal probe with a mode-locked femtosecond laser source *Appl. Sci.* **9** 4084

[86] Chen C, Sato R, Shimizu Y, Nakamura T, Matsukuma H and Gao W 2019 A method for expansion of Z-directional measurement range in a mode-locked femtosecond laser chromatic confocal probe *Appl. Sci.* **9** 454

[87] Watanabe T, Kon M, Nabeshima N and Taniguchi K 2014 An angle encoder for super-high resolution and super-high accuracy using SelfA *Meas. Sci. Technol.* **25** 065002

[88] Ikram M and Hussain G 1999 Michelson interferometer for precision angle measurement *Appl. Opt.* **38** 113

[89] Gao W, Arai Y, Shibuya A, Kiyono S and Park C H 2006 Measurement of multi-degree-of-freedom error motions of a precision linear air-bearing stage *Precis. Eng.* **30** 96–103

[90] Nikon Corporation 2019 Autocollimators 6B-LED/6D-LED

[91] MÖLLER-WEDEL OPTICAL 2007 Electroninc autocollimators

[92] Trioptics GmbH 2013 OptiTest (R) a complete range of optical instrument

[93] Gao W 2010 *Precision Nanometrology* (London: Springer London)

[94] Ennos A E and Virdee M S 1982 High accuracy profile measurement of quasi-conical mirror surfaces by laser autocollimation *Precis. Eng.* **4** 5–8

[95] Saito Y, Arai Y and Gao W 2010 Investigation of an optical sensor for small tilt angle detection of a precision linear stage *Meas. Sci. Technol.* **21** 054006

[96] Shimizu Y, Tan S L, Murata D, Maruyama T, Ito S, Chen Y-L and Gao W 2016 Ultra-sensitive angle sensor based on

laser autocollimation for measurement of stage tilt motions *Opt. Express* **24** 2788

[97] Gao W, Ohnuma T, Satoh H, Shimizu H, Kiyono S and Makino H 2004 A precision angle sensor using a multi-cell photodiode array *CIRP Ann. Manuf. Technol.* **53** 425–8

[98] Gao W, Huang P S, Yamada T and Kiyono S 2002 A compact and sensitive two-dimensional angle probe for flatness measurement of large silicon wafers *Precis. Eng.* **26** 396–404

[99] Bitou Y and Kondo Y 2016 Scanning deflectometric profiler for measurement of transparent parallel plates *Appl. Opt.* **55** 9282

[100] Gao W and Kiyono S 1996 High accuracy profile measurement of a machined surface by the combined method *Measurement* **19** 55–64

[101] Gao W, Kiyono S and Sugawara T 1997 High-accuracy roundness measurement by a new error separation method *Precis. Eng.* **21** 123–33

[102] Gao W, Tano M, Sato S and Kiyono S 2006 On-machine measurement of a cylindrical surface with sinusoidal micro-structures by an optical slope sensor *Precis. Eng.* **30** 274–9

[103] Gao W, Saito Y, Muto H, Arai Y and Shimizu Y 2011 A three-axis autocollimator for detection of angular error motions of a precision stage *CIRP Ann. Manuf. Technol.* **60** 515–8

[104] Shimizu Y, Kataoka S, Ishikawa T, Chen Y-L, Chen X, Matsukuma H and Gao W 2018 A liquid-surface-based three-axis inclination sensor for measurement of stage tilt motions *Sensors* **18** 398

[105] Matsukuma H, Ishizuka R, Furuta M, Li X, Shimizu Y and Gao W 2019 Reduction in cross-talk errors in a six-degree-of-freedom surface encoder *Nanomanuf. Metrol.* **2** 111–23

[106] Shimizu Y, Kudo Y, Chen Y-L, Ito S and Gao W 2017 An optical lever by using a mode-locked laser for angle measurement *Precis. Eng.* **47** 72–80

[107] Chen Y-L, Shimitzu Y, Kudo Y, Ito S S, Gao W, Shimizu Y, Kudo Y, Ito S S and Gao W 2016 Mode-locked laser autocollimator with an expanded measurement range *Opt. Express* **24** 425–8

[108] Chen Y-L, Shimizu Y, Tamada J, Kudo Y, Madokoro S, Nakamura K and Gao W 2017 Optical frequency domain angle measurement in a femtosecond laser autocollimator *Opt. Express* **25** 16725–38

[109] Chen Y-L, Shimizu Y, Tamada J, Nakamura K, Matsukuma H, Chen X and Gao W 2018 Laser autocollimation based on an optical frequency comb for absolute angular position measurement *Precis. Eng.* **54** 284–93

[110] Matsukuma H, Madokoro S, Dwi W, Yuki A and Wei S 2019 A new optical angle measurement method based on second harmonic generation with a mode–locked femtosecond laser *Nanomanuf. Metrol.* **2** 187–98

[111] Shimizu Y, Madokoro S, Matsukuma H and Gao W 2018 An optical angle sensor based on chromatic dispersion with a mode-locked laser source *J. Adv. Mech. Des. Syst. Manuf.* **12** 1–10

[112] Shimizu Y, Matsukuma H and Gao W 2020 Optical angle sensor technology based on the optical frequency comb laser *Appl. Sci.* **10** 4047

[113] Nawrocki W 2019 The new SI system of units—the SI of 2018 *Introduction to Quantum Metrology* (Berlin: Springer International Publishing) pp 41–84

[114] Bosse H, Kunzmann H, Pratt J R, Schlamminger S, Robinson I, de Podesta M, Shore P, Balsamo A and Morantz P 2017 Contributions of precision engineering to the revision of the SI *CIRP Ann. Manuf. Technol.* **66** 827–50

[115] Robinson I A and Schlamminger S 2016 The watt or Kibble balance: a technique for implementing the new SI definition of the unit of mass *Metrologia* **53** A46–74

[116] Chao L, Seifert F, Haddad D, Pratt J, Newell D and Schlamminger S 2020 The performance of the KIBB-g1 tabletop Kibble balance at NIST *Metrologia* **57** 035014

[117] Fujii K, Bettin H, Becker P, Massa E, Rienitz O, Pramann A, Nicolaus A, Kuramoto N, Busch I and Borys M 2016 Realization of the kilogram by the XRCD method *Metrologia* **53** A19–45

[118] Parks R E 2008 Specifications: figure and finish are not enough *An Optical Believe It or Not: Key Lessons Learned* vol 7071, ed M A Kahan (SPIE) p 70710B

[119] Martin H M *et al* 2016 Manufacture and final tests of the LSST monolithic primary/tertiary mirror *Proc. SPIE*, ed R Navarro and J H Burge p 99120X

[120] Martin H M, Allen R G, Burge J H, Kim D W, Kingsley J S, Tuell M T, West S C, Zhao C and Zobrist T 2010 Fabrication and testing of the first 8.4-m off-axis segment for the Giant Magellan Telescope *Modern Technologies in Space- and Ground-based Telescopes and Instrumentation* vol 7739 (SPIE) p 77390A

[121] Martin H M *et al* 2014 Production of primary mirror segments for the Giant Magellan Telescope *Advances in Optical and Mechanical Technologies for Telescopes and Instrumentation* vol 9151, eds R Navarro, C R Cunningham and A A Barto (SPIE) p 91510J

[122] Scheiding S, Beier M, Zeitner U-D, Risse S and Gebhardt A 2013 Freeform mirror fabrication and metrology using a high performance test CGH and advanced alignment features *Advanced Fabrication Technologies for Micro/Nano Optics and Photonics VI* vol 8613, eds G von Freymann, W V Schoenfeld and R C Rumpf (SPIE) p 86130J

[123] Pant L M, Singh M P, Pant K K and Ghosh A 2015 In process metrology of aspheric optical surfaces during sub-aperture polishing process *International Conference on Optics and Photonics 2015* vol 9654, ed K Bhattacharya (SPIE) p 96540U

[124] Zhao Z, Zhao H, Gu F, Du H and Li K 2014 Non-null testing for aspheric surfaces using elliptical sub-aperture stitching technique *Opt. Express* **22** 5512

[125] Chen S, Xue S, Dai Y and Li S 2015 Subaperture stitching test of large steep convex spheres *Opt. Express* **23** 29047

[126] Oh C J, Lowman A E, Dubin M, Smith G, Frater E, Zhao C and Burge J H 2016 Modern technologies of fabrication and testing of large convex secondary mirrors *Advances in Optical and Mechanical Technologies for Telescopes and Instrumentation II* vol 9912, ed R Navarro and J H Burge (SPIE) p 99120R

[127] Kulawiec A, Murphy P and DeMarco M 2010 Measurement of high-departure aspheres using subaperture stitching with the variable optical null (VON) *5th International Symposium on Advanced Optical Manufacturing and Testing Technologies: Advanced Optical Manufacturing Technologies* vol 7655, eds L Yang, Y Namba, D D Walker and S Li (SPIE) p 765512

[128] Chen S, Li S and Wang G 2014 Subaperture test of wavefront error of large telescopes: error sources and stitching performance simulations *International Symposium on Optoelectronic Technology and Application 2014: Imaging Spectroscopy; and Telescopes and Large Optics* vol 9298, eds J P Rolland, C Yan, D W Kim, W Ma and L Zheng (SPIE) p 929817

[129] Chen S, Xue S, Dai Y and Li S 2017 Subaperture stitching test of convex aspheres by using the reconfigurable optical null *Opt. Laser Technol.* **91** 175–84

[130] Saif B *et al* 2015 Nanometer level characterization of the James Webb space telescope optomechanical systems using high-speed interferometry *Appl. Opt.* **54** 4285

[131] Kim D W, Aftab M, Choi H, Graves L and Trumper I 2014 Optical metrology systems spanning the full spatial frequency spectrum *Optics InfoBase Conference Papers* (OSA - The Optical Society) p FW5G.4

[132] Su T, Wang S, Parks R E, Su P and Burge J H 2013 Measuring rough optical surfaces using scanning long-wave optical test system. 1. Principle and implementation *Appl. Opt.* **52** 7117–26

[133] Su T, Park W H, Parks R E, Su P and Burge J H 2011 Scanning long-wave optical test system: a new ground optical surface slope test system *Optical Manufacturing and Testing IX* vol 8126 (SPIE) p 81260E

[134] Oh C J, Lowman A E, Smith G A, Su P, Huang R, Su T, Kim D, Zhao C, Zhou P and Burge J H 2016 Fabrication and testing of 4.2 m off-axis aspheric primary mirror of Daniel K. Inouye Solar Telescope *Advances in Optical and Mechanical Technologies for Telescopes and Instrumentation II* vol 9912, ed R Navarro and J H Burge (SPIE) p 99120O

[135] Kim D W, Oh C, Lowman A, Smith G A, Aftab M and Burge J H 2016 Manufacturing of super-polished large aspheric/freeform optics *Advances in Optical and Mechanical Technologies for Telescopes and Instrumentation II* vol 9912, ed R Navarro and J H Burge (SPIE) p 99120F

[136] Huang L, Ng C S and Asundi A K 2011 Dynamic three-dimensional sensing for specular surface with monoscopic fringe reflectometry *Opt. Express* **19** 12809

[137] Wu Y, Yue H, Yi J, Li M and Liu Y 2016 Dynamic specular surface measurement based on color-encoded fringe reflection technique *Opt. Eng.* **55** 024104

[138] Peter de G and Leslie D 1995 Surface profiling by analysis of white-light interferograms in the spatial frequency domain *J. Mod. Opt.* **42** 389–401

[139] Henri M A 1952 US2612074(A)

[140] Flournoy P A, McClure R W and Wyntjes G 1972 White-light interferometric thickness gauge *Appl. Opt.* **11** 1907

[141] James C W 1995 Computerized interferometric measurement of surface microstructure *Proc. SPIE* **2576** 26–37

[142] Novak E and Schmit J 2003 White-light optical profiler with integrated primary standard *Proc. XVII IMEKO World Congr. Metrol* (https://www.imeko.org/publications/wc-2003/PWC-2003-TC2-009.pdf)

[143] Chen L C, Yeh S L, Tapilouw A M and Lee K F 2012 In-situ scanning white light interferometry employing dual-sensing configuration and active fringe-locking strategy *Int. J. Nanomanuf.* **8** 40

[144] Chen L-C and Tapilouw A M 2013 Theoretical simulation and experimental confirmation of duty cycle effect on stroboscopic white light interferometry for M(O)EMS dynamic characterization *J. Micromech. Microeng.* **23** 115008

[145] Chen L-C, Le M-T and Lin Y-S 2014 3-D micro surface profilometry employing novel Mirau-based lateral scanning interferometry *Meas. Sci. Technol.* **25** 094004

[146] Tapilouw A M 2011 *Research on Orthogonal Polarization Mirau Interferometry for Nanometer-scale Surface Profilometry* (Taipei: National Taiwan University)

[147] Denisyuk Y N 1963 On the reproduction of the optical properties of an object by the wave field of its scattered radiation, Pt. I *Opt. Spectrosc.* **15** 279

[148] Leith E N and Swanson G J 1980 Achromatic interferometers for white light optical processing and holography *Appl. Opt.* **19** 638

[149] Wyant J C 2002 White light interferometry *Proc. SPIE*, ed H J Caulfield (SPIE) pp 98–107

[150] Leach R, Brown L, Jiang X, Blunt R and Mike Conroy D M 2008 *Guide for the Measurement of Smooth Surface Topography using Coherence Scanning Interferometry* (http://eprintspublications.npl.co.uk/id/eprint/4099%0A)

[151] Lehmann P 2006. Systematic effects in coherence peak and phase evaluation of signals obtained with a vertical scanning white-light Mirau interferometer ed C Gorecki, A K Asundi and W Osten (SPIE) p 618811

[152] Harasaki A, Schmit J and Wyant J C 2000 Improved vertical-scanning interferometry *Appl. Opt.* **39** 2107

[153] Harasaki A and Wyant J C 2000 Fringe modulation skewing effect in white-light vertical scanning interferometry *Appl. Opt.* **39** 2101

[154] de Groot P, Colonna de Lega X, Kramer J and Turzhitsky M 2002 Determination of fringe order in white-light interference microscopy *Appl. Opt.* **41** 4571

[155] Gao F, Leach R K, Petzing J and Coupland J M 2008 Surface measurement errors using commercial scanning white light interferometers *Meas. Sci. Technol.* **19** 015303

[156] Pförtner A and Schwider J 2001 Dispersion error in white-light Linnik interferometers and its implications for evaluation procedures *Appl. Opt.* **40** 6223

[157] Schmit J and Olszak A 2002 High-precision shape measurement by white-light interferometry with real-time scanner error correction *Appl. Opt.* **41** 5943

[158] Niehues J, Lehmann P and Bobey K 2007 Dual-wavelength vertical scanning low-coherence interferometric microscope *Appl. Opt.* **46** 7141

[159] Tapilouw A M, Chen L-C, Jen Y-J, Lin S-T and Yeh S-L 2013 Orthogonal polarization Mirau interferometer using reflective-type waveplate *Opt. Lett.* **38** 2502

[160] Kino G S and Chim S S C 1990 Mirau correlation microscope *Appl. Opt.* **29** 3775

[161] Chim S C, Beck P A and Kino G S 1990 A novel thin film interferometer *Rev. Sci. Instrum.* **61** 980–3

[162] Chim S S C and Kino G S 1990 Correlation microscope *Opt. Lett.* **15** 579

[163] Chim S S C and Kino G S 1991 Phase measurements using the Mirau correlation microscope *Appl. Opt.* **30** 2197

[164] Fang C C, Gordon S K and William K S 1994 Development of a deep-UV Mirau correlation microscope *Proc. SPIE* **2196** 35–46

[165] Chang F C and Kino G S 1997 Ultraviolet Mirau correlation microscopy *Three-Dimensional Microscopy: Image Acquisition and Processing IV* vol **2984**, eds C J Cogswell, J-A Conchello and T Wilson pp 30–41

[166] Chang F C and Kino G S 1998 325-nm Interference microscope *Appl. Opt.* **37** 3471

[167] Niehues J and Lehmann P 2011 Improvement of lateral resolution and reduction of batwings in vertical scanning white-light interferometry *Proc. SPIE*, eds P H Lehmann, W Osten and K Gastinger (SPIE) p 80820W

[168] Lyulko O V, Randers-Pehrson G and Brenner D J 2010 Immersion Mirau interferometry for label-free live cell imaging in an epi-illumination geometry *Proc. SPIE*, eds D L Farkas, D V Nicolau and R C Leif (SPIE) p 756825

[169] Lyulko O V, Randers-Pehrson G and Brenner D J 2013 Simultaneous immersion Mirau interferometry *Rev. Sci. Instrum.* **84** 053701

[170] Paul Kumar U and Manojit P 2017 Microsphere-aided optical microscopy and its applications for super-resolution imaging *Opt. Commun.* **404** 32–41

[171] Kim M and Rho J 2015 Metamaterials and imaging *Nano Convergence* **2** 22

[172] Bates M, Huang B, Dempsey G T and Zhuang X 2007 Multicolor super-resolution imaging with photo-switchable fluorescent probes *Science* **317** 1749–53

[173] Serrano V M, Monreal J G and Zalesky Z 2008 Superresolution optics: optical imaging resolves beyond the diffraction limit *Laser Focus World* (https://www.laserfocusworld.com/optics/article/16554961/super resolution-optics-optical-imaging-resolves-beyond-the-diffraction-limit)

[174] Li M, Li W, Li H, Zhu Y and Yu Y 2017 Controllable design of super-oscillatory lenses with multiple sub-diffraction-limit foci *Sci. Rep.* **7** 1335

[175] Nagarajan A, Stoevelaar L P, Silvestri F, Siemons M, Achanta V G, Bäumer S M B and Gerini G 2019 Reflection confocal nanoscopy using a super-oscillatory lens *Opt. Express* **27** 20012

[176] Dehez H, Piché M and De Koninck Y 2013 Resolution and contrast enhancement in laser scanning microscopy using dark beam imaging *Opt. Express* **21** 15912

[177] Thibon L, Piché M and De Koninck Y 2018 Resolution enhancement in laser scanning microscopy with deconvolution switching laser modes (D-SLAM) *Opt. Express* **26** 24881

[178] Goorden S A, Bertolotti J and Mosk A P 2014 Superpixel-based spatial amplitude and phase modulation using a digital micromirror device *Opt. Express* **22** 17999

[179] Marcel A L, Jan K, Andreas S, Dirk K, Volker W, Silvio O R and Stefan W H 2010 Comparing video-rate STED nanoscopy and confocal microscopy of living neurons *J. Biophotonics* **3** 417–24

[180] Farahani J, Schibler M and Bentolila L 2010 Stimulated emission depletion (STED) microscopy: from theory to practice *Microsc. Sci. Technol. Appl. Educ.* **2** 1539–47

[181] Xiaowei Z 2009 Nano-imaging with STORM *Nat. Photonics* **3** 365–7

[182] Russell E T, Daniel R L and Watt W W 2002 Precise nanometer localization analysis for individual fluorescent probes *Biophys. J.* **82** 2775–83

[183] Tobisch A, Neher P F, Rowe M C, Maier-Hein K H and Zhang H 2014 Model-based super-resolution of diffusion MRI *Computational Diffusion MRI and Brain Connectivity* (Berlin: Springer International Publishing) pp 25–34

[184] Bano W, Piredda G F, Davies M, Marshall I, Golbabaee M, Meuli R, Kober T, Thiran J and Hilbert T 2020 Model-based super-resolution reconstruction of T2 maps *Magn. Reson. Med.* **83** 906–19

[185] Pohl D W 1991 Scanning near-field optical microscopy (SNOM) *Advances in Optical and Electron Microscopy* vol 12 (Amsterdam: Elsevier) p 243–312

[186] Wang F, Liu L, Yu P, Liu Z, Yu H, Wang Y and Li W J 2016 Three-dimensional super-resolution morphology by near-field assisted white-light interferometry *Sci. Rep.* **6** 24703

[187] Massig J H 1992 Interferometric profilometer sensor US 05166751

[188] Marbach S, Perrin S, Montgomery P, Flury M and Lecler S 2019 Microsphere-assisted imaging of sub-diffraction-limited features *Optical Measurement Systems for Industrial Inspection XI*, eds P Lehmann, W Osten and A A Gonçalves (SPIE) pp 26

[189] Wang Z and Luk'yanchuk B 2019 Super-resolution imaging and microscopy by dielectric particle-lenses *Label-Free Super-Resolution Microscopy* pp 371–406

[190] Hou B, Xie M, He R, Ji M, Trummer S, Fink R H and Zhang L 2017 Microsphere assisted super-resolution optical imaging of plasmonic interaction between gold nanoparticles *Sci. Rep.* **7** 13789

[191] Wang F, Liu L and Li W J 2016 Near-field assisted white-light interferometry for 3D nanoscale imaging *SPIE Newsroom*

[192] Stankewitz H W 2003 Variable epi-illumination interference attachment *US Patent* 6538809

[193] Hariharan P 2007 Improved polarization Mirau interference microscope *Opt. Eng.* **46** 077007

[194] Schmit J and Hariharan P 2011 Polarization Mirau interference microscope *US Patent Specification* US8072610(B1)

[195] Hariharan P 1996 Achromatic and apochromatic halfwave and quarterwave retarders *Opt. Eng.* **35** 3335

[196] Pavliček P and Hýbl O 2008 White-light interferometry on rough surfaces–measurement uncertainty caused by surface roughness *Appl. Opt.* **47** 2941

[197] Pavliček P and Hýbl O 2012 White-light interferometry on rough surfaces—measurement uncertainty caused by noise *Appl. Opt.* **51** 465

[198] Wiesner B, Hybl O and Häusler G 2012 Improved white-light interferometry on rough surfaces by statistically independent speckle patterns *Appl. Opt.* **51** 751

[199] Yoshino T, Nara M, Mnatzakanian S, Lee B S and Strand T C 1987 Laser diode feedback interferometer for stabilization and displacement measurements *Appl. Opt.* **26** 892

[200] Cole G C, Burge J H and Dettmann L R 1997 Vibration stabilization of a phase-shifting interferometer for large optics *Proc. SPIE*, ed H P Stahl (SPIE) pp 438–46

[201] He L 2006 Vibration-compensated interferometry system using phase-modulating interference fringe subdivision technology *Appl. Opt.* **45** 7987

[202] Iwai H, Fang-Yen C, Popescu G, Wax A, Badizadegan K, Dasari R R and Feld M S 2004 Quantitative phase imaging using actively stabilized phase-shifting low-coherence interferometry *Opt. Lett.* **29** 2399

[203] Li X, Yamauchi T, Iwai H, Yamashita Y, Zhang H and Hiruma T 2006 Full-field quantitative phase imaging by white-light interferometry with active phase stabilization and its application to biological samples *Opt. Lett.* **31** 1830

[204] Yamauchi T, Iwai H, Miwa M and Yamashita Y 2007 Measurement of topographic phase image of living cells by white-light phase-shifting microscope with active stabilization of optical path difference *Proc. SPIE*, eds J G Fujimoto, J A Izatt and V V Tuchin (SPIE) p 64291Q

[205] Wizinowich P L 1990 Phase shifting interferometry in the presence of vibration: a new algorithm and system *Appl. Opt.* **29** 3271

[206] Deck L 1996 Vibration-resistant phase-shifting interferometry *Appl. Opt.* **35** 6655

[207] Carlson T B, Denzer S M, Greenlee T R, Groschen R P, Peterson R W and Robinson G M 1997 Vibration-resistant direct-phase-detecting optical interferometers *Appl. Opt.* **36** 7162

[208] Yoshino T and Yamaguchi H 1998 Closed-loop phase-shifting interferometry with a laser diode *Opt. Lett.* **23** 1576

[209] Jiyuan L and Ichirou Y 1999 Fringe locking in a laser diode interferometer by optical feedback during modulation of injection current *Opt. Rev.* **6** 100–3

[210] Bao Y, Su H and Yang Y 2005 Fringe-locking phenomenon in a laser diode interferometer with optical feedback *Proc. SPIE*, eds Y Wang, Z Weng, S Ye and J M Sasian (SPIE) p 797

[211] Freschi A A and Frejlich J 1995 Adjustable phase control in stabilized interferometry *Opt. Lett.* **20** 635

[212] Yamaguchi I 1996 Active phase-shifting interferometers for shape and deformation measurements *Opt. Eng.* **35** 2930

[213] Ji-Yuan L, Ichirou Y, Jun-ichi K and Toshinori N 1997 Real-time surface shape measurement by an active interferometer *Opt. Rev.* **4** 216–20

[214] Zhao C and Burge J H 2001 Vibration-compensated interferometer for surface metrology *Appl. Opt.* **40** 6215

[215] Krishnamachari V V, Andresen E R, Keiding S R and Potma E O 2006 An active interferometer-stabilization scheme with linear phase control *Opt. Express* **14** 5210

[216] Schmit J, Olszak A G and McDermed S D 2002 White-light interferometry with reference signal *Proc. SPIE*, ed K Creath and J Schmit (SPIE) p 102

[217] Schmit J and Joanna S 2003 High-stability white-light interferometry with reference signal for real-time correction of scanning errors *Opt. Eng.* **42** 54

[218] Jiang X, Wang K, Gao F and Muhamedsalih H 2010 Fast surface measurement using wavelength scanning interferometry with compensation of environmental noise *Appl. Opt.* **49** 2903

[219] Liang-Chia C, Yao-Ting H and Kuang-Chao F 2007 A dynamic 3-D surface profilometer with nanoscale measurement resolution and MHz bandwidth for MEMS characterization *IEEE/ASME Trans. Mechatron.* **12** 299–307

[220] Liang-Chia C, Yao-Ting H, Xuan-Loc N, Jin-Liang C and Chung-Chu C 2009 Dynamic out-of-plane profilometry for nano-scale full-field characterization of MEMS using stroboscopic interferometry with novel signal deconvolution algorithm *Opt. Lasers Eng.* **47** 237–51

[221] Liang Chia C, Abraham Mario T, Sheng Lih Y, Shyh Tsong L, Jin Liang C and Huan Chi H 2010 Development of innovative fringe locking strategies for vibration-resistant white light vertical scanning interferometry (VSI) *Key Eng. Mater.* **437** 89–94

[222] Tereschenko S, Lehmann P, Zellmer L and Brueckner-Foit A 2016 Passive vibration compensation in scanning white-light interferometry *Appl. Opt.* **55** 6172

[223] Il M J, Jo T, Kim T and Pahk H J 2015 Residual vibration reduction of white-light scanning interferometry by input shaping *Opt. Express* **23** 464

[224] Teale C, Barbastathis G and Schmidt M A 2019 Vibration compensated, scanning white light interferometer for in situ depth measurements in a deep reactive ion etcher *J. Microelectromech. Syst.* **28** 441–6

[225] Raymond C 2005 Overview of scatterometry applications in high volume silicon manufacturing *AIP Conf. Proc.* vol 788 (AIP) pp 394–402

[226] Raymond C J 1997 Multiparameter grating metrology using optical scatterometry *J. Vac. Sci. Technol.* B **15** 361

[227] El Kodadi M, Soulan S, Besacier M and Schiavone P 2009 Real time scatterometry for profile control during resist trimming process *J. Vac. Sci. Technol.* B **27** 3232

[228] Patrick H J, Germer T A, Ding Y, Ro H W, Richter L J and Soles C L 2008 Scatterometry for in situ measurement of pattern reflow in nanoimprinted polymers *Appl. Phys. Lett.* **93** 233105

[229] Ko C-H and Ku Y-S 2006 Overlay measurement using angular scatterometer for the capability of integrated metrology *Opt. Express* **14** 6001

[230] Madsen M H and Hansen P-E 2016 Scatterometry—fast and robust measurements of nano-textured surfaces *Surf. Topogr. Metrol. Prop.* **4** 023003

[231] den Boef A J 2016 Optical wafer metrology sensors for process-robust CD and overlay control in semiconductor device manufacturing *Surf. Topogr. Metrol. Prop.* **4** 023001

[232] McNeil J R 1992 Scatterometry applied to microelectronics processing *2000 Digest of the LEOS Summer Topical Meetings. Electronic-Enhanced Optics. Optical Sensing in Semiconductor Manufacturing Electro-Optics in Space. Broadband Optical Networks (Cat. No.00TH8497)* vol 1 (IEEE) pp II37–8

[233] Naqvi S S H, McNeil J R, Krukar R H and Bishop K P 1993 Scatterometry and the simulation of diffraction-based metrology *Microlithogr. World* **2** 5–16

[234] Boher P, Luet M, Leroux T, Petit J, Barriault P, Hazart J and Chaton P 2004 Innovative rapid photogoniometry method for CD metrology *Proc. SPIE.*, ed R M Silver (SPIE) pp 1302

[235] Hazart J, Barriault P, Garcia S, Leroux T, Boher P and Tsujino K 2007 Robust sub-50-nm CD control by a fast-goniometric scatterometry technique *Proc. SPIE.*, ed C N Archie (SPIE) p 65183A

[236] Gross H, Rathsfeld A, Scholze F and Bär M 2009 Profile reconstruction in extreme ultraviolet (EUV) scatterometry: modeling and uncertainty estimates *Meas. Sci. Technol.* **20** 105102

[237] Henn M-A, Heidenreich S, Gross H, Rathsfeld A, Scholze F and Bär M 2012 Improved grating reconstruction by determination of line roughness in extreme ultraviolet scatterometry *Opt. Lett.* **37** 5229

[238] Ku Y-S, Yeh C-L, Chen Y-C, Lo C-W, Wang W-T and Chen M-C 2016 EUV scatterometer with a high-harmonic-generation EUV source *Opt. Express* **24** 28014

[239] Ansuinelli P, Coene W M J and Urbach H P 2019 Automatic feature selection in EUV scatterometry *Appl. Opt.* **58** 5916

[240] Jones R L, Hu T, Lin E K, Wu W-L, Kolb R, Casa D M, Bolton P J and Barclay G G 2003 Small angle x-ray scattering for sub-100 nm pattern characterization *Appl. Phys. Lett.* **83** 4059–61

[241] Daniel F S, Scott L, Jasmeet S C and Joseph R K 2015 Determining the shape and periodicity of nanostructures using small-angle x-ray scattering *J. Appl. Crystallogr.* **48** 1355–63

[242] Mika P, Victor S, Jürgen P, Frank S and Michael K 2017 Grazing-incidence small-angle x-ray scattering (GISAXS) on small periodic targets using large beams *IUCrJ* **4** 431–8

[243] Freychet G, Kumar D, Pandolfi R J, Naulleau P, Cordova I, Ercius P, Song C, Strzalka J and Hexemer A 2019 Estimation of line cross sections using critical-dimension grazing-incidence small-angle x-ray scattering *Phys. Rev. Appl.* **12** 044026

[244] Azzam R M, Bashara N M and Ballard S S 1978 Ellipsometry and Polarized Light *Phys. Today* **31** 72

[245] Fujiwara H 2007 *Spectroscopic Ellipsometry: Principles and Applications* (New York: Wiley)

[246] Niu X, Jakatdar N, Bao J and Spanos C J 2001 Specular spectroscopic scatterometry *IEEE Trans. Semicond. Manuf.* **14** 97–111

[247] Hsu-Ting H, Wei K and Fred Lewis T 2001 Normal-incidence spectroscopic ellipsometry for critical dimension monitoring *Appl. Phys. Lett.* **78** 3983–5

[248] Novikova T, De Martino A, Ben H S and Drévillon B 2006 Application of Mueller polarimetry in conical diffraction for critical dimension measurements in microelectronics *Appl. Opt.* **45** 3688

[249] Novikova T, De Martino A, Bulkin P, Nguyen Q, Drévillon B, Popov V and Chumakov A 2007 Metrology of replicated diffractive optics with Mueller polarimetry in conical diffraction *Opt. Express* **15** 2033

[250] Kim Y-N, Paek J-S, Rabello S, Lee S, Hu J, Liu Z, Hao Y and McGahan W 2009 Device based in-chip critical dimension and overlay metrology *Opt. Express* **17** 21336

[251] Chen X, Liu S, Zhang C, Jiang H, Ma Z, Sun T and Xu Z 2014 Accurate characterization of nanoimprinted resist patterns using Mueller matrix ellipsometry *Opt. Express* **22** 15165

[252] Liu S, Chen X and Zhang C 2015 Development of a broadband Mueller matrix ellipsometer as a powerful tool for nanostructure metrology *Thin Solid Films* **584** 176–85

[253] Diebold A C, Antonelli A and Keller N 2018 Perspective: optical measurement of feature dimensions and shapes by scatterometry *APL Mater.* **6** 058201

[254] Korde M, Kal S, Alix C, Keller N, Antonelli G A, Mosden A and Diebold A C 2020 Nondestructive characterization of nanoscale subsurface features fabricated by selective etching of multilayered nanowire test structures using Mueller matrix spectroscopic ellipsometry based scatterometry *J. Vac. Sci. Technol.* B **38** 024007

[255] Hsu-Ting H and Terry Jr F L 2004 Spectroscopic ellipsometry and reflectometry from gratings (Scatterometry) for critical dimension measurement and in situ, real-time process monitoring *Thin Solid Films* **455–456** 828–36

[256] Chen X, Zhang C, Liu S, Jiang H, Ma Z and Xu Z 2014 Mueller matrix ellipsometric detection of profile asymmetry in nanoimprinted grating structures *J. Appl. Phys.* **116** 194305

[257] Wurm M, Endres J, Probst J, Schoengen M, Diener A and Bodermann B 2017 Metrology of nanoscale grating structures by UV scatterometry *Opt. Express* **25** 2460

[258] Hartmut P, Wolfgang B and Marco P 2002 Bézier techniques *Bézier and B-Spline Techniques* (Berlin: Springer) p 25–41

[259] Bao G, Chen Z and Wu H 2005 Adaptive finite-element method for diffraction gratings *J. Opt. Soc. Am.* A **22** 1106

[260] Jan P and Frank S 2010 Accelerated *a posteriori* error estimation for the reduced basis method with application to 3D electromagnetic scattering problems *SIAM J. Sci. Comput.* **32** 498–520

[261] Nakata Y and Koshiba M 1990 Boundary-element analysis of plane-wave diffraction from groove-type dielectric and metallic gratings *J. Opt. Soc. Am.* A **7** 1494

[262] Shi Y, Chen X, Tan Y, Jiang H and Liu S 2017 Reduced-basis boundary element method for fast electromagnetic field computation *J. Opt. Soc. Am.* A **34** 2231

[263] Taflove A and Hagness S 2000 *Computational Electrodynamics: The Finite-difference Time-domain Method* vol 67 2nd edn p 106 (Boston, MA: ARTECH HOUSE) (https://us.artechhouse.com/Computational-Electrodynamics-Third-Edition-P1929.aspx)

[264] Moharam M G, Gaylord T K, Grann E B and Pommet D A 1995 Formulation for stable and efficient implementation of the rigorous coupled-wave analysis of binary gratings *J. Opt. Soc. Am.* A **12** 1068

[265] Moharam M G, Gaylord T K, Pommet D A and Grann E B 1995 Stable implementation of the rigorous coupled-wave analysis for surface-relief gratings: enhanced transmittance matrix approach *J. Opt. Soc. Am.* A **12** 1077

[266] Herwig K 1969 Coupled wave theory for thick hologram gratings *Bell Syst. Tech. J.* **48** 2909–47

[267] Moharam M G and Gaylord T K 1981 Rigorous coupled-wave analysis of planar-grating diffraction *J. Opt. Soc. Am.* **71** 811

[268] Moharam M G and Gaylord T K 1983 Rigorous coupled-wave analysis of grating diffraction— E-mode polarization and losses *J. Opt. Soc. Am.* **73** 451

[269] Moharam M G and Gaylord T K 1983 Three-dimensional vector coupled-wave analysis of planar-grating diffraction *J. Opt. Soc. Am.* **73** 1105

[270] Moharam M G and Gaylord T K 1982 Diffraction analysis of dielectric surface-relief gratings *J. Opt. Soc. Am.* **72** 1385

[271] Moharam M G and Gaylord T K 1986 Rigorous coupled-wave analysis of metallic surface-relief gratings *J. Opt. Soc. Am.* A **3** 1780

[272] Moharam M G 1988 Coupled-wave analysis of two-dimensional dielectric gratings *Holographic Optics: Design and Applications* vol 0883, ed I Cindrich (SPIE) p 8

[273] Lalanne P and Morris G M 1996 Highly improved convergence of the coupled-wave method for TM polarization *J. Opt. Soc. Am.* A **13** 779

[274] Granet G and Guizal B 1996 Efficient implementation of the coupled-wave method for metallic lamellar gratings in TM polarization *J. Opt. Soc. Am.* A **13** 1019

[275] Li L 1996 Use of Fourier series in the analysis of discontinuous periodic structures *J. Opt. Soc. Am.* A **13** 1870

[276] Lalanne P 1997 Improved formulation of the coupled-wave method for two-dimensional gratings *J. Opt. Soc. Am.* A **14** 1592

[277] Li L 1997 New formulation of the Fourier modal method for crossed surface-relief gratings *J. Opt. Soc. Am.* A **14** 2758

[278] Schuster T, Ruoff J, Kerwien N, Rafler S and Osten W 2007 Normal vector method for convergence improvement using the RCWA for crossed gratings *J. Opt. Soc. Am.* A **24** 2880

[279] Nevière M and Popov E 2018 *Light Propagation in Periodic Media* (Boca Raton, FL: CRC Press)

[280] Götz P, Schuster T, Frenner K, Rafler S and Osten W 2008 Normal vector method for the RCWA with automated vector field generation *Opt. Express* **16** 17295

[281] Li L 1996 Formulation and comparison of two recursive matrix algorithms for modeling layered diffraction gratings *J. Opt. Soc. Am.* A **13** 1024

[282] Tan E L 2002 Note on formulation of the enhanced scattering- (transmittance-) matrix approach *J. Opt. Soc. Am.* A **19** 1157

[283] Tan E L 2006 Enhanced R-matrix algorithms for multilayered diffraction gratings *Appl. Opt.* **45** 4803

[284] Raymond C J, Littau M E, Chuprin A and Ward S 2004 Comparison of solutions to the scatterometry inverse problem *Proc. SPIE.*, ed R M Silver (SPIE) pp 564

[285] Press W H, Teukolsky S A, Vetterling W T and Flannery B P 2007 *Numerical Recipes 3rd Edition the Art of Scientific Computing* (Cambridge: Cambridge University Press)

[286] Madsen K, Nielsen H B and Tingleff O 2004 *Methods for Non-Linear Least Squares Problems* 2nd edn (Denmark: Technical University of Denmark)

[287] Chen X, Liu S, Zhang C and Zhu J 2013 Improved measurement accuracy in optical scatterometry using fitting error interpolation based library search *Meas. J. Int. Meas. Confederation* **46** 2638–46

[288] Chen X, Liu S, Zhang C and Jiang H 2013 Improved measurement accuracy in optical scatterometry using correction-based library search *Appl. Opt.* **52** 6726–34

[289] Anon 2019 International Roadmap for Devices and Systems (IRDS^TM) 2018 Edition-IEEE International Roadmap for Devices and Systems^TM (IEEE Press)

[290] Bunday B D, Bello A, Solecky E and Vaid A 2018 7/5nm logic manufacturing capabilities and requirements of metrology *Metrology, Inspection, and Process Control for Microlithography XXXII* vol 10585, ed O Adan and V A Ukraintsev (SPIE) p 17

[291] Orji N G, Badaroglu M, Barnes B M, Beitia C, Bunday B D, Celano U, Kline R J, Neisser M, Obeng Y and Vladar A E 2018 Metrology for the next generation of semiconductor devices *Nat. Electron.* **1** 532–47

[292] Rana N, Zhang Y, Kagalwala T and Bailey T 2014 Leveraging advanced data analytics, machine learning, and metrology models to enable critical dimension metrology solutions for advanced integrated circuit nodes *J. Micro/Nanolithography, MEMS, MOEMS* **13** 041415

[293] Brown K A, Brittman S, Maccaferri N, Jariwala D and Celano U 2020 Machine learning in nanoscience: big data at small scales *Nano Lett.* **20** 2–10

[294] Drexler W, Liu M, Kumar A, Kamali T, Unterhuber A and Leitgeb R A 2014 Optical coherence tomography today:

[295] Wang L V 2004 Ultrasound-mediated biophotonic imaging: a review of acousto-optical tomography and photo-acoustic tomography *Dis. Markers* **19** 123–38

[296] Endoh H, Ohtaki N and Hoshimiya T 2006 Nondestructive detection of tilted surface defect with wedge shape by photoacoustic microscopy *Japan. J. Appl. Phys.* **45** 4609–11

[297] Hoshimiya T, Endoh H and Hiwatashi Y 1996 Observation of surface defects using photoacoustic microscope and quantitative evaluation of the defect depth *Japan. J. Appl. Phys.* 1 **35** 2916–20

[298] Carmignato S 2018 *Industrial X-Ray Computed Tomography*, eds S Carmignato, W Dewulf and R Leach (Cham: Springer International Publishing)

[299] De Chiffre L, Carmignato S, Kruth J P, Schmitt R and Weckenmann A 2014 Industrial applications of computed tomography *CIRP Ann. Manuf. Technol.* **63** 655–77

[300] Drexler W 2004 Ultrahigh-resolution optical coherence tomography *J. Biomed. Opt.* **9** 47

[301] Tanno N, Ichimura T and Saeki A 1990 *Japanese Patent* 2010042

[302] Huang D *et al* 1991 Optical coherence tomography *Science* **22** 1178–81

[303] Tan-no N, Ichimura T, Funaba T, Anndo N and Odagiri Y 1994 Optical multimode frequency-domain reflectometer *Opt. Lett.* **19** 587

[304] Beaurepaire E, Boccara A, Lebec M, Blanchot L and Saint-Jalmes H 1998 Full-field optical coherence microscopy *Opt. Lett.* **23** 244–6

[305] Yun S H, Tearney G J, De Boer J F, Iftimia N and Bouma B E 2003 High-speed optical frequency-domain imaging *Opt. Express* **11** 2953–63

[306] Sarunic M V, Weinberg S and Izatt J A 2006 Full-field swept-source phase microscopy *Opt. Letters* **31** 1462–4

[307] Huber R 2006 Fourier domain mode locking (FDML): a new laser operating regime and applications for biomedical imaging, profilometry, ranging and sensing *Opt. Ex.* **14** 1981–3

[308] Wieser W, Biedermann B R, Klein T, Eigenwillig C M and Huber R 2010 Multi-Megahertz OCT: high quality 3D imaging at 20 million A-scans and 45 GVoxels per second *Opt. Express* **18** 14685

[309] Exalos 2020 EXALOS: high-performance broadband SLEDs, swept sources and sub-systems

[310] Moon S and Kim D Y 2006 Ultra-high-speed phase-sensitive optical coherence reflectometer with a stretched pulse supercontinuum source *Opt. Express* **14** 11575–84

[311] Kim S H, Kim J H and Kang S W 2011 Nondestructive defect inspection for LCDs using optical coherence tomography *Displays* **32** 325–9

[312] Hayman B, Berggreen C and Pettersson R 2007 The effect of face sheet wrinkle defects on the strength of FRP Sandwich structures *J. Sandwich Struct. Mater.* **9** 377–404

[313] Campagne B, Voillaume H and Passelande P 2014 Optical coherence tomography for inspection of aeronautic composite parts *13th Int. Symp. on Nondestructive Characterization of Materials (NDCM-XIII)*

[314] Liu P, Groves R M and Benedictus R 2014 Optical coherence tomography for the study of polymer and polymer matrix composites *Strain* **50** 436–43

[315] Holder D, Boley S, Buser M, Weber R and Graf T 2018 In-process determination of fiber orientation for layer accurate laser ablation of CFRP *Procedia CIRP* **74** 557–61

[316] Lewis A D, Mcelroy A, Beaman J, Lewis A D, Katta N, Mcelroy A, Milner T, Fish S and Beaman J 2018

Understanding and improving optical coherence tomography imaging depth in selective laser sintering nylon 12 parts and powder *Opt. Eng.* **57** 1

[317] DePond P J, Guss G, Ly S, Calta N P, Deane D, Khairallah S and Matthews M J 2018 In situ measurements of layer roughness during laser powder bed fusion additive manufacturing using low coherence scanning interferometry *Mater. Des.* **154** 347–59

[318] Bashkansky M, Duncan M D, Kahn M, Lewis D and Reintjes J 1997 Subsurface defect detection in ceramics by high-speed high-resolution optical coherent tomography *Opt. Lett.* **22** 61

[319] Duncan M D, Bashkansky M and Reintjes J 1998 Subsurface defect detection in materials using optical coherence tomography *Opt. Express* **2** 540

[320] Bashkansky M 2002 Subsurface detection and characterization of Hertzian cracks in advanced ceramic materials using optical coherence tomography *Proc. SPIE* **4703** 46–52

[321] Angrisani L, Bechou L, Dallet D, Daponte P and Ousten Y 2002 Detection and location of defects in electronic devices by means of scanning ultrasonic microscopy and the wavelet transform *Meas. J. Int. Meas. Confederation* **31** 77–91

[322] Duval S, Bernier M, Fortin V, Genest J, Piché M and Vallée R 2015 Femtosecond fiber lasers reach the mid-infrared *Optica* **2** 623

[323] Petersen C R *et al* 2014 Mid-infrared supercontinuum covering the 1.4-13.3 μm molecular fingerprint region using ultra-high NA chalcogenide step-index fibre *Nat. Photonics* **8** 830–4

[324] Bawden N, Matsukuma H, Henderson-Sapir O, Klantsataya E, Tokita S and Ottaway D J 2018 Actively Q-switched dual-wavelength pumped Er 3+:ZBLAN fiber laser at 347 μm *Opt. Lett.* **43** 2724

[325] Israelsen N M, Petersen C R, Barh A, Jain D, Jensen M, Hannesschläger G, Tidemand-Lichtenberg P, Pedersen C, Podoleanu A and Bang O 2019 Real-time high-resolution mid-infrared optical coherence tomography *Light Sci. Appl.* **8** 11

[326] Su R, Kirillin M, Chang E W, Sergeeva E, Yun S H and Mattsson L 2014 Perspectives of mid-infrared optical coherence tomography for inspection and micrometrology of industrial ceramics *Opt. Express* **22** 15804

[327] Huang B, Bates M and Zhuang X 2009 Super-resolution fluorescence microscopy *Annu. Rev. Biochem.* **78** 993–1016

[328] Schermelleh L, Ferrand A, Huser T, Eggeling C, Sauer M, Biehlmaier O and Drummen G P C 2019 Super-resolution microscopy demystified *Nat. Cell Biol.* **21** 72–84

[329] Huszka G and Gijs M A M 2019 Super-resolution optical imaging: a comparison *Micro. Nano Eng.* **2** 7–28

[330] Berterot M, Brianzit P and Pikeg E R 1987 *Super-resolution in Confocal Scanning Microscopy* vol 3 (Bristol: IOP Publishing)

[331] Pawley J B 2006 *Handbook of Biological Confocal Microscopy* 3rd edn (Berlin: Springer)

[332] Zhao W, Sun Y, Wang Y, Qiu L, Shao R and Cui H 2018 Three-dimensional super-resolution correlation-differential confocal microscopy with nanometer axial focusing accuracy *Opt. Express* **26** 15759

[333] Wu Y 2010 Research on some key problems in scanning near-field optical microscopy

[334] Harootunian A, Betzig E, Isaacson M and Lewis A 1986 Super-resolution fluorescence near-field scanning optical microscopy *Appl. Phys. Lett.* **49** 674–6

[335] Betzig E, Saul Isaacson M and Lewis A 1987 Collection mode near-field scanning optical microscopy *Appl. Phys. Lett.* **51** 2088–90

[336] Gleyzes P, Boccara A C and Bachelot R 1995 Near field optical microscopy using a metallic vibrating tip *Ultramicroscopy* **57** 318–22

[337] Heinzelmann H, Hecht B, Novotny L and Pohl D W 1995 Forbidden light scanning near-field optical microscopy *J. Microsc.* **177** 115–8

[338] Hecht B, Sick B, Wild U P, Deckert V, Zenobi R, Martin O J F and Pohl D W 2000 Scanning near-field optical microscopy with aperture probes: fundamentals and applications *J. Chem. Phys.* **112** 7761–74

[339] Hecht B, Heinzelmann H and Pohl D W 1995 Combined aperture SNOM/PSTM: best of both worlds? *Ultramicroscopy* **57** 228–34

[340] Reddick R C, Warmack R J and Ferrell T L 1989 New form of scanning optical microscopy *Phys. Rev.* B **39** 767–70

[341] Ohtsu M and Ohtsu M 1995 Progress of high-resolution photon scanning tunneling microscopy due to a nanometric fiber probe *J. Light. Technol.* **13** 1200–21

[342] Fischer U C, Koglin J and Fuchs H 1994 The tetrahedral tip as a probe for scanning near-field optical microscopy at 30 nm resolution *J. Microsc.* **176** 231–7

[343] Zenhausern F, Martin Y and Wickramasinghe H K 1995 Scanning interferometric apertureless microscopy: optical imaging at 10 angstrom resolution *Science* **269** 1083–5

[344] Takahashi S, Ikeda Y and Takamasu K 2013 Study on nano thickness inspection for residual layer of nanoimprint lithography using near-field optical enhancement of metal tip *CIRP Ann. Manuf. Technol.* **62** 527–30

[345] Quantum Design 2021 neaSNOM

[346] Di Francia G T 1952 Super-gain antennas and optical resolving power *Nuovo Cimento* **9** 426–38

[347] Okazaki S 2015 High resolution optical lithography or high throughput electron beam lithography: the technical struggle from the micro to the nano-fabrication evolution *Microelectron. Eng.* **133** 23–35

[348] Tang F, Wang Y, Qiu L, Zhao W and Sun Y 2014 Super-resolution radially polarized-light pupil-filtering confocal sensing technology *Appl. Opt.* **53** 7407

[349] Zhao W, Tan J and Qiu L 2004 Bipolar absolute differential confocal approach to higher spatial resolution *Opt. Express* **12** 5013

[350] Li Z, Herrmann K and Pohlenz F 2007 Lateral scanning confocal microscopy for the determination of in-plane displacements of microelectromechanical systems devices *Opt. Lett.* **32** 1743

[351] Aguilar J F, Lera M and Sheppard C J R 2000 Imaging of spheres and surface profiling by confocal microscopy *Appl. Opt.* **39** 4621

[352] Arrasmith C L, Dickensheets D L and Mahadevan-Jansen A 2010 MEMS-based handheld confocal microscope for in-vivo skin imaging *Opt. Express* **18** 3805

[353] Sun C-C and Liu C-K 2003 Ultrasmall focusing spot with a long depth of focus based on polarization and phase modulation *Opt. Lett.* **28** 99

[354] Heintzmann R and Huser T 2017 Super-resolution structured illumination microscopy *Chem. Rev.* **117** 13890–908

[355] Wu Y and Shroff H 2018 Faster, sharper, and deeper: structured illumination microscopy for biological imaging *Nat. Methods* **15** 1011–9

[356] Habuchi S 2014 Super-resolution molecular and functional imaging of nanoscale architectures in life and materials science *Frontiers Bioeng. Biotechnol.* **2** 20

[357] Takahashi S, Kudo R, Usuki S and Takamasu K 2011 Super resolution optical measurements of nanodefects on Si wafer surface using infrared standing evanescent wave *CIRP Ann. Manuf. Technol.* **60** 523–6

[358] Chen Z, Taflove A and Backman V 2004 Photonic nanojet enhancement of backscattering of light by nanoparticles: a potential novel visible-light ultramicroscopy technique *Opt. Express* **12** 1214

[359] Li X, Chen Z, Taflove A and Backman V 2005 Optical analysis of nanoparticles via enhanced backscattering facilitated by 3-D photonic nanojets *Opt. Express* **13** 526

[360] Wang Z, Guo W, Li L, Luk'Yanchuk B, Khan A, Liu Z, Chen Z and Hong M 2011 Optical virtual imaging at 50 nm lateral resolution with a white-light nanoscope *Nat. Commun.* **2** 1–6

[361] Itagi A V and Challener W A 2005 Optics of photonic nanojets *J. Opt. Soc. Am.* A **22** 2847

[362] Ferrand P, Wenger J, Devilez A, Pianta M, Stout B, Bonod N, Popov E and Rigneault H 2008 Direct imaging of photonic nanojets *Opt. Express* **16** 6930

[363] Lee J Y *et al* 2009 Near-field focusing and magnification through self-assembled nanoscale spherical lenses *Nature* **460** 498–501

[364] Quan L, Shimizu Y, Xiong X, Matsukuma H and Gao W 2021 A new method for evaluation of the pitch deviation of a linear scale grating by an optical angle sensor *Precis. Eng.* **67** 1–13